Optical Control and Spectroscopic Studies of Collisional Population Transfer in Molecular Electronic States

---

A Dissertation

Submitted to

the Temple University Graduate Board

---

in Partial Fulfillment

of the Requirements for the Degree of

DOCTOR OF PHILOSOPHY

---

by

Xinhua Pan

May, 2017

Examining Committee Members:

A. Marjatta Lyyra, Advisory Chair, Department of Physics

Andreas Metz, Department of Physics

Peter S. Riseborough, Department of Physics

Francis C. Spano, Department of Chemistry

Eric Borguet, Department of Chemistry

ABSTRACT

The quantum interference effects, such as the Autler-Townes (AT) effect and electromagnetically induced transparency (EIT) applied to molecular systems are the focus of this Dissertation in the context of high resolution molecular spectroscopy. We demonstrate that the AT effect can be used to manipulate the spin character of a spin-orbit coupled pair of molecular energy levels serving as a *gateway* between the singlet and triplet electronic states. We demonstrate that the singlet-triplet mixing characters of the *gateway* levels can be controlled by manipulating the coupling laser E field amplitude.

We observe experimentally the collisional population transfer between electronic states $G^1\Pi_g(v = 12, J = 21, f)$ and $1^3\Sigma_g^-(v = 1, N = 21, f)$ of $^7Li_2$. We obtain the Stern-Vollmer plot according to the vapor pressure dependence of collisional transfer rate. The triplet fluorescence from the mixed *gateway* levels to the triplet $b^3\Pi_u(v' = 1, J' = 20, 21, 22)$ levels as a function of the probe laser detuning as well as the control laser detuning are observed and compared. The control laser power dependence of the triplet fluorescence signal intensity is recorded to demonstrate that the collisional transfer rate can be enhanced by increasing the control laser power level (Rabi frequency). The conservation of the molecular population transfer is confirmed by comparing the singlet and triplet fluorescence with the control laser detuning over the resonance.

A large number of ro-vibrational levels of the $6^1\Sigma_g^+$ and $3^1\Pi_g$ electronic states of $^{85}Rb_2$ are observed experimentally by optical-optical double resonance (OODR) spectroscopy technique. The rotational and vibrational Dunham coefficients are extracted from the experimental ro-vibrational energies, and the preliminary Rydberg-Klein-Rees (RKR) potential energy curves are constructed for both states. The ro-vibrational eigenvalues are calculated from the preliminary RKR potential energy curves by using the LEVEL program and compared with the measured ro-vibrational

energy values in order to test the quality of the preliminary RKR potential energy curves. The ro-vibrational eigenvalues calculated from the *ab-initio* curves are also compared with our preliminary RKR potential energy curves. The quantum numbers of the collisional lines are assigned by comparing with the theoretical term values of the intermediate $A^1\Sigma_u^+ \sim b^3\Pi_u$ states, and additional term values for the $6^1\Sigma_g^+$ and $3^1\Pi_g$ states are determined.

ACKNOWLEDGMENTS

I would like to show my sincere gratitude to numerous people who helped me during my education in Physics. First of all, I wish to extend my deepest thanks to my dissertation advisor Prof. A. Marjatta Lyyra for her indispensable mentoring of my study. Her enthusiasm and professionalism impressed me the first day I joined her group. Besides her solid knowledge, her spirit as a female scientist encourages me to pursue the truth of science. She is always there whenever we need help. Her great personality and hospitality make our group a big warm family. She will be my role model for my future endeavor.

I would also like to thank Prof. Theodore W. Burkhardt, Prof. Peter S. Riseborough, and Porf. Andreas Metz for being my teachers and leading me to the gate of advanced Physics. I thank my dissertation committee memebers: Porf. Andreas Metz, Prof. Peter S. Riseborough, Prof. Francis C. Spano, and Prof. Eric Borguet for the time they spending on reading and advising my dissertation and examining my oral defense.

I would like to thank Dr. Ergin Ahmed for his guidance in the lab. I appreciate very much the opportunity to work with him.

I would like to thank Prof. John Huennekens from Lehigh University and Prof. Chin-Chun Tsai from NCKU for sharing their invaluable scientific knowledge and experimental expertise when they visited our group.

I would like to thank our former female group members Dr. Jianmei Bai, Dr. Bediha Beser, and Dr. Yafei Guan, for introducing me to the research and teaching me how to operate the equipment in the lab. Their friendship and a lot of memorable "girls' time" made me not feel lonely far away in a foreign country. I would also like to thank my fellow group member Aydin Sanli for both the cooperation and peer pressure which pushed me to move forward. I would like to thank Phillip Todd Arndt and David Samuel Beecher for their eagerness in learning the workings of the lab.

I would like to thank Edward Kaczanowicz and Matthew McCormick for their mechanical support to our lab, as well as Richard J. Harris for his assistance on our electrical problems. Without their help we would not have been able to perform our experiments successfully.

I would like to thank the previous group members, Dr. Jianbing Qi, Dr. Jenny Magnes, and Dr. Teodora Kirova, for their pioneering work on both theory and experiment which enlightened and encouraged me on my research.

I am very grateful to my mother Ping Li and my father Yinsheng Pan. Thanks for their unconditional support on both my life and education. I also thank my parents-in-law, Zhenxin Liu and Ruixin Liu, for the care they give to my daughter and my family.

Last but not least, I must thank my husband, Yuqiao Liu, for his consistent love, support and understanding during these years, especially for the darkest time. Special thanks go to my daughter, Claire, who is always so cheerful and reminds me to keep positive and strong.

Dedicated to my family.

TABLE OF CONTENTS

LIST OF TABLES

LIST OF FIGURES

CHAPTER 1

INTRODUCTION

The great interest in alkali dimers such as Li_2, Na_2 and Rb_2 parallel to the development of laser technology can be attributed to numerous scientific geniuses such as the Nobel Prize winners Charles Hard Townes (July 28, 1915 - January 27, 2015) and Arthur Leonard Schawlow (May 5, 1921 - April 28, 1999).

The development of narrow bandwidth single mode tunable laser sources permits very high sensitivity and accurate determination of the energy level. Thus the coherence effects have drawn a lot of attention to various phenomena including coherent population trapping (CPT) [1–3], electromagnetically induced transparency (EIT) [4–6], Autler-Townes (AT) effect [7], lasing without invasion (LWI) [8–10], molecular angular momentum alignment [11], slow light [12, 13], reconstruction of an entangled state [14], and atom localization [15], etc. In this dissertation, we focus on the quantum control of the collisional population transfer between singlet and triplet state manifolds achieved by manipulating the spin character of a pair of singlet-triplet mixed *gateway* levels using the Autler-Townes effect.

Furthermore, recently the Rubidium dimer molecules are of great interest in many fields such as ultra-cold molecule formation, cold atom-molecule collisions, etc. However, since the Rb_2 molecule has a dense ro-vibrational energy level structure and

the spin-orbit interaction is relatively strong, the perturbations between electronic states cannot be ignored. The experimental observation of the electronic states is more challenging especially for the high-lying electronic states. In this dissertation, we also present the spectroscopic observation of the electronic states $6^1\Sigma_g^+$ and $3^1\Pi_g$ of $^{85}Rb_2$, and preliminary analysis of the potential energy curves.

This dissertation consists of five chapters. Chapter 2 gives an outline of the theoretical background of the diatomic molecules. The Born-Oppenheimer approximation is introduced in addition to the labelling of an electronic state of a diatomic molecule. The vibrational and rotational motions of diatomic molecules are discussed, and the total energy of a particular ro-vibrational level in terms of the vibrational and rotational quantum number, v and J, respectively, is expressed by Dunham expansion. The coupling of angular momentum vectors is briefly described according to Hund's case (a), (b), (c), and (d). The selection rules for molecular transitions determined by the transition dipole moment operator are also given in this chapter.

Chapter 3 elaborates the quantum control of the spin-orbit interaction based on the Autler-Townes effect [16]. The experimental and theoretical investigation of EIT and Autler-Townes effect is given for a four-level molecular system by continuous wave (*cw*) laser spectroscopy. The spin-orbit interaction and the *gateway* effect are introduced. The control of the singlet-triplet mixing characters of the *gateway* levels by manipulating the coupling laser E field amplitude is demonstrated.

Chapter 4 describes our recent work about optical control of collisional population transfer between electronic states $G^1\Pi_g$ and $1^3\Sigma_g^-$ of $^7Li_2$ [17]. The experimental set-up and the parameter values of the optical fields are given. The excitation scheme and the reaction steps are illustrated. The Stern-Vollmer plot according to the vapor pressure dependence of collisional transfer rate is obtained from the experiment. The triplet and singlet fluorescence signals with the probe and the control laser detuning

are observed and compared. The simulation of the collisional transfer rate confirms our experimental results.

Chapter 5 presents the spectroscopic study of the electronic states $6^1\Sigma_g^+$ and $3^1\Pi_g$ of $^{85}Rb_2$. The experimental set-up and the excitation scheme of the collisional transfer by using the optical-optical double resonance (OODR) spectroscopic technique are shown. A large number of ro-vibrational levels of the two electronic states are measured and preliminarily analyzed. The Dunham's coefficients are extracted from the experimental ro-vibrational energies, and the preliminary RKR potential energy curves are constructed. The quality of the preliminary potential energy curves is tested by reproducing the ro-vibrational eigenvalues and comparing with the measured values as well as with the *ab-initio* curves. The assignment of the collisional lines is given and all observed levels of the two states are presented.

References

[1] H. R. Gray, R. M. Whitley, and C. R. Stroud, Opt. Lett. **3**, 218 (1978).

[2] F. Renzoni, A. Lindner, and E. Arimondo, Phys. Rev. A **60**, 450 (1999).

[3] F.-L. Li, and S.-Y. Zhu, Opt. Commun. **162**, 155 (1999).

[4] S. E. Harris, J. E. Field, and A. Imamoğlu, Phys. Rev. Lett. **64**, 1107 (1990).

[5] K.-J. Boller, A. Imamoğlu, and S. E. Harris, Phys. Rev. Lett. **66**, 2593 (1991).

[6] J. E. Field, K. H. Hahn, and S. E. Harris, Phys. Rev. Lett. **67**, 3062 (1991).

[7] S. H. Autler, and C. H. Townes, Phys. Rev. **100**, 703 (1955).

[8] A. Imamoğlu, and S. E. Harris, Opt. Lett. **14**, 1344 (1989).

[9] S. E. Harris, Phys. Rev. Lett. **62**, 1033 (1989).

[10] M. O. Scully, S.-Y. Zhu, and A. Gavrielides, Phys. Rev. Lett. **62**, 2813 (1989).

[11] J. Qi, G. Lazarov, X. Wang, L. Li, L. M. Narducci, A. M. Lyyra, and F. C. Spano, Phys. Rev. Lett. **83**, 288 (1999).

[12] M. M. Kash, V. A. Sautenkov, A. S. Zibrov, L. Hollberg, G. R. Welch, M. D. Lukin, Y. Rostovtsev, E. S. Fry, and M. O. Scully, Phys. Rev. Lett. **82**, 5229 (1999).

[13] D. Budker, D. F. Kimball, S. M. Rochester, and V. V. Yashchuk, Phys. Rev. Lett. **83**, 1767 (1999).

[14] M. Ikram, and M. S. Zubairy, Phys. Rev. A **65**, 044305 (2002).

[15] V. Minogin, and Y. Rozhdestvenskii, Opt. Commun. **64**, 172 (1987).

[16] E. H. Ahmed, S. Ingram, T. Kirova, O. Salihoglu, J. Huennekens, J. Qi, Y. Guan, and A. M. Lyyra, Phys. Rev. Lett. **107**, 163601 (2011).

[17] E. H. Ahmed, X. Pan, J. Huennekens, and A. M. Lyyra, Phys. Rev. A **89**, 061401 (2014).

CHAPTER 2

INTRODUCTION TO DIATOMIC MOLECULES

2.1 Introduction

Numerous textbooks and papers [18–22] about the basic quantum mechanical studies can be found to understand the diatomic molecular structure. This chapter provides some background information regarding diatomic molecules, including the Born-Oppenheimer approximation, vibration and rotation of diatomic molecules, the coupling of angular momentum vectors, and the selection rules. These topics support the logistics for the presentation of this dissertation.

2.2 The Born-Oppenheimer Approximation

The time independent Schrödinger equation for a diatomic molecule system is given by [20]

$$\widehat{H}\psi(\boldsymbol{r}_i, \boldsymbol{R}) = E\psi(\boldsymbol{r}_i, \boldsymbol{R}), \tag{2.1}$$

and the total Hamiltonian for a diatomic molecule can be written as

$$\widehat{H} = \widehat{T}_{\rm nuc} + \widehat{T}_{\rm elec} + V(\boldsymbol{r}_i, \boldsymbol{R}). \tag{2.2}$$

Thus the Schrödinger equation 2.1 can be written as

$$\widehat{H}\psi(\boldsymbol{r}_i, \boldsymbol{R}) = \left[\widehat{T}_{\rm nuc} + \widehat{T}_{\rm elec} + V(\boldsymbol{r}_i, \boldsymbol{R})\right] \psi(\boldsymbol{r}_i, \boldsymbol{R}) = E\psi(\boldsymbol{r}_i, \boldsymbol{R}), \tag{2.3}$$

where $\widehat{T}_{\rm nuc}$ and $\widehat{T}_{\rm elec}$ are the nuclear and electronic kinetic energy operators, respectively,

$$\widehat{T}_{\rm nuc} = \frac{-\hbar^2}{2\mu}\nabla^2_{\boldsymbol{R}}, \tag{2.4}$$

$$\widehat{T}_{\rm elec} = \sum_{i=1}^{N}\left(\frac{-\hbar^2}{2m_e}\nabla^2_{\boldsymbol{r}_i}\right), \tag{2.5}$$

and $V(\boldsymbol{r}_i, \boldsymbol{R})$ is the Coulomb interaction potential energy including contributions from each pair of charged particles in the molecule,

$$\begin{aligned} V(\boldsymbol{r}_i, \boldsymbol{R}) = & -\sum_{i=1}^{N}\frac{Z_{\rm A}e^2}{4\pi\epsilon_0|\boldsymbol{r}_i - \boldsymbol{R}_{\rm A}|} - \sum_{i=1}^{N}\frac{Z_{\rm B}e^2}{4\pi\epsilon_0|\boldsymbol{r}_i - \boldsymbol{R}_{\rm B}|} \\ & + \frac{1}{2}\sum_{i\neq j}^{N}\frac{e^2}{4\pi\epsilon_0|\boldsymbol{r}_i - \boldsymbol{r}_j|} + \frac{Z_{\rm A}Z_{\rm B}e^2}{4\pi\epsilon_0 R}, \end{aligned} \tag{2.6}$$

where $\boldsymbol{r}_i$ are the position vectors of the ith electron from the center of mass of the nuclei, $\boldsymbol{R} \equiv \boldsymbol{R}_{\rm B} - \boldsymbol{R}_{\rm A}$, with $\boldsymbol{R}_{\rm A}$ and $\boldsymbol{R}_{\rm B}$ the positions of the nuclei relative to the center of mass, and the internuclear distance $R = |\boldsymbol{R}|$. m_e is the mass of the electron, and μ is the reduced mass of the nuclei A and B,

$$\mu = \frac{M_{\rm A}M_{\rm B}}{M_{\rm A} + M_{\rm B}}.$$

$Z_{\mathrm{A}}e$ and $Z_{\mathrm{B}}e$ are the nuclear charges of the two nuclei.

Since the mass of the electrons m_e is much smaller than the mass of the nuclei, and the nuclei move much slower than the electrons, the electronic and nuclear motion can be considered separately, which is well known as the Born-Oppenheimer approximation [23]. One consequence of this assumption is that the polyatomic molecular electronic states can be treated as potential energy surfaces, and for diatomic molecules the electronic states can be treated as potential energy curves. The nuclear motion is governed by the electronic wavefunctions at fixed nuclear distance, which are obtained by solving the Schrödinger equation for the electrons [18].

The time independent Schrödinger equation of the electrons moving in the field of nuclei at a fixed position $\boldsymbol{R}$ can be written as

$$\left[\widehat{T}_{\mathrm{elec}} + V(\boldsymbol{r}_i, \boldsymbol{R})\right] \phi_n(\boldsymbol{r}_i, \boldsymbol{R}) = E_n(R)\phi_n(\boldsymbol{r}_i, \boldsymbol{R}), \tag{2.7}$$

where ϕ_n and $E_n(R)$ are the eigenfunctions and eigenvalues of the molecular state n depending on the internuclear distance R. The complete, orthonormal set of the electronic wavefunctions ϕ_n satisfies

$$\int \mathrm{d}^3\boldsymbol{r}_i \phi_n^*(\boldsymbol{r}_i, \boldsymbol{R})\phi_m(\boldsymbol{r}_i, \boldsymbol{R}) = \delta_{nm}. \tag{2.8}$$

Thus the molecular wavefunction $\psi(\boldsymbol{r}_i, \boldsymbol{R})$ can be expressed as the expansion

$$\psi(\boldsymbol{r}_i, \boldsymbol{R}) = \sum_n F_n(\boldsymbol{R})\phi_n(\boldsymbol{r}_i, \boldsymbol{R}), \tag{2.9}$$

where $F_n(\boldsymbol{R})$ are the wavefunctions of the nuclear motion while the electronic system is in state n. The coupled equations can then be obtained by substituting Equation 2.9

into Equation 2.3, and multiplying by $\phi_m(\boldsymbol{r}_i, \boldsymbol{R})$ on the left,

$$\sum_n \left[\int \mathrm{d}^3 \boldsymbol{r}_i \phi_m^*(\boldsymbol{r}_i, \boldsymbol{R}) \widehat{T}_{\mathrm{nuc}} \phi_n(\boldsymbol{r}_i, \boldsymbol{R}) F_n(\boldsymbol{R}) \right] + (E_m(R) - E) F_m(\boldsymbol{R}) = 0. \tag{2.10}$$

$F_m(\boldsymbol{R})$ with $m = 1, 2, 3, \cdots$ can then further be determined. The operator $\widehat{T}_{\mathrm{nuc}}$ acting on the product $\phi_n F_n$ yields

$$\widehat{T}_{\mathrm{nuc}}(\phi_n F_n) = -\frac{\hbar^2}{2\mu}[F_n(\nabla^2_{\boldsymbol{R}} \phi_n) + 2(\nabla_{\boldsymbol{R}} F_n \cdot \nabla_{\boldsymbol{R}} \phi_n) + \phi_n(\nabla^2_{\boldsymbol{R}} F_n)]. \tag{2.11}$$

Considering that the variation of ϕ_n, $\nabla_{\boldsymbol{R}} \phi_n$, is much less than the variation of F_n, $\nabla_{\boldsymbol{R}} F_n$, with respect to $\boldsymbol{R}$ [18], the Equation 2.11 can be simplified by the Born-Oppenheimer approximation,

$$\widehat{T}_{\mathrm{nuc}}(\phi_n F_n) \approx -\frac{\hbar^2}{2\mu}[\phi_n(\nabla^2_{\boldsymbol{R}} F_n)]. \tag{2.12}$$

Thus the Equation 2.10 reduces to the nuclear Schrödinger equation

$$\left[\frac{-\hbar^2}{2\mu} \nabla^2_{\boldsymbol{R}} + (E_m(R) - E) \right] F_m(\boldsymbol{R}) = 0. \tag{2.13}$$

with

$$m = 1, 2, 3, \cdots,$$

where $F_m(\boldsymbol{R})$ are the unclear wavefunctions and $E_m(R)$ are the electronic eigenvalues for the potential of the electronic state m, with respect to the internuclear distance R, yielded by the Born-Oppenheimer approximation.

2.3 Vibration and Rotation of Diatomic Molecules

As described in the previous section, $E_m(R)$ represents the electronic energy of the molecule in the corresponding electronic state. A typical electronic state of a diatomic molecule could be labeled as [20]

$$n^{2S+1}\Lambda^{+/-}_{\Omega,g/u} ,$$

where S is the total electronic spin quantum number which is usually 0 or 1 for homonuclear diatomic molecules, the superscript $2S+1$ is called spin multiplicity. The electronic states with $S=0$ have a multiplicity of one are called "singlet" states, and the states with $S=1$ have a multiplicity of three and are called "triplet" states. Λ is the absolute value of the projection of electronic orbital angular momentum $\boldsymbol{L}$ onto the internuclear axis, with $\Lambda = 0, 1, 2, \cdots$ for $\Sigma, \Pi, \Delta, \cdots$ states, respectively, and n denotes the energy ordering of states with the same S and Λ. "$+/-$" is the symmetry to classify Σ states ($\Lambda = 0$), in which the electronic wave function either remains unchanged (labeled as Σ^+) or changes sign (labeled as Σ^-) upon reflection of the electrons through any plane containing the internuclear axis. Ω is the sum of the components of the spin and orbital angular momentum along the internuclear axis,

$$\Omega = |\Lambda + \Sigma|.$$

For homonuclear molecules, "g/u" (*gerade/ungerade* in German) is used to label the symmetric or antisymmetric state whose electronic wavefunction remains unchanged or changes through the inversion of all electrons through the center of mass ($\boldsymbol{r}_i \rightarrow -\boldsymbol{r}_i$). For certain states we use the capital lettering of the electronic states, i.e. the X state refers to the ground electronic state $1^1\Sigma_g^+$ of each alkali diatomic molecule.

In addition, for a homonuclear molecule, the parity "s/a" is used to label a *symmetric/antisymmetric* rotational level. When the two identical nuclei are exchanged, the total eigenfunction either remains unchanged or only changes its sign [20]. If the wavefunction remains the same, the level is labeled by "s", and if the wavefunction changes the sign, the level is labeled by "a".

The parity "e/f" which is also known as the rotationless parity, was introduced by Brown *et al.* in 1975 [24]. The e/f basis functions are defined as those with total parity $(\pm)(-1)^J$ for melecules with an even number of electrons and $(\pm)(-1)^{J-1/2}$ for molecules with an odd number of electrons [25]. For the electronic state with "+" total parity, a particular ro-vibrational level is labeled as "e" if $(+)(-1)^J = 1$, and it's labeled as "f" if $(+)(-1)^J = -1$. And for the electronic state with "−" total parity, a particular ro-vibrational level is labeled as "e" if $(-)(-1)^J = 1$, and it's labeled as "f" if $(-)(-1)^J = -1$ [26]. All rotational levels of the electronic states $^1\Sigma^+$ are labeled as e parity.

To a good approximation, the diatomic molecular motion can be broken into two types of motions. One is vibration of the nuclei along the internuclear axis, and the other is rotation about an axis that passes through the center of mass of the nuclei and is perpendicular to the internuclear axis. The total energy or the term value of the molecule can be written by

$$E = E_e + E_v + E_r, \tag{2.14}$$

where E_e refers to the electronic energy at the bottom of the potential energy well, E_v and E_r are the vibrational and rotational energies, respectively.

First, considering the rotational energies as the energy eigenvalues of a rigid rotor, E_r can be written as [20],

$$E_r = \frac{\hbar^2}{2I} J(J+1) = B_e J(J+1), \tag{2.15}$$

where J is the rotational quantum number ($J = 0, 1, 2, \cdots$), and B_e is the rotational constant

$$B_e = \frac{\hbar^2}{2I},$$

$I = \mu R^2$ is the moment of inertia with the reduced mass

$$\mu = \frac{M_1 M_2}{M_1 + M_2}.$$

Note that the energies of these levels increase quadratically with J, and the energy spacing between a level J and the next higher level $J + 1$ increases linearly (see Figure 2.1),

$$\Delta E_r = E_r(J + 1) - E_r(J) = 2JB_e.$$

However, the bond between the two nuclei of the molecule is not completely rigid, and the Equation 2.15 is inadequate to describe rotational energy levels of diatomic molecules. Since while rotating at higher rates, the molecule stretches with increasing moment of inertia, a term of centrifugal distortion in the rotational energy needs to be added to the rotational energy [20],

$$E_r = B_e J(J + 1) - D_e[J(J + 1)]^2, \tag{2.16}$$

where D_e is the centrifugal distortion constant. This term is negative, because when the moment of inertian I increases, the rotational energy decreases.

The nuclei of a diatomic molecule are free to vibrate along the internuclear axis as well. Considering a harmonic oscillator at first, the potential energy function $V(R) = E_m(R)$ can be expressed by a Taylor expansion about its minimum at the equilibrium separation R_0,

$$V(R) = V(R_0) + \left(\frac{\mathrm{d}V}{\mathrm{d}R}\right)_{R=R_0} (R - R_0) + \frac{1}{2}\left(\frac{\mathrm{d}^2V}{\mathrm{d}R^2}\right)_{R=R_0} (R - R_0)^2 + \cdots . \tag{2.17}$$

Since the first derivative of the potential is zero at its minimum, the second term vanishes. Neglecting higher order terms in the expansion, the potential energy function can be approximated as a harmonic oscillator

$$V(R) \approx V(R_0) + \frac{1}{2}k(R - R_0)^2, \tag{2.18}$$

where k is the second derivative of the potential at the equilibrium separation

$$k = \left(\frac{\mathrm{d}^2 V}{\mathrm{d}R^2}\right)_{R=R_0}.$$

By solving the Schrödinger equation with Equation 2.18, the vibrational energies of a diatomic molecule are approximated as

$$E_v = \omega_e \left(v + \frac{1}{2}\right), \tag{2.19}$$

where v is the vibrational quantum number ($v = 0, 1, 2, 3, \cdots$), and ω_e is the frequency of vibration in wavenumber unit (cm^{-1}),

$$\omega_e = \frac{1}{2\pi c}\sqrt{\frac{k}{\mu}}.$$

However, the harmonic oscillator approximation is only good at low vibrational energies. For the high-lying vibrational levels, the higher order terms must be retained in the Taylor expansion 2.17. By adding anharmonic terms into Equation 2.19, the vibrational energies are written as [20]

$$G_v = \omega_e \left(v + \frac{1}{2}\right) - \omega_e x_e \left(v + \frac{1}{2}\right)^2 + \omega_e y_e \left(v + \frac{1}{2}\right)^3 + \cdots, \tag{2.20}$$

where $\omega_e x_e$ and $\omega_e y_e$ are anharmonicity constants, and $\omega_e >> \omega_e x_e >> \omega_e y_e$. The separation between the vibrational energy levels decreases as v increases (see Figure 2.1).

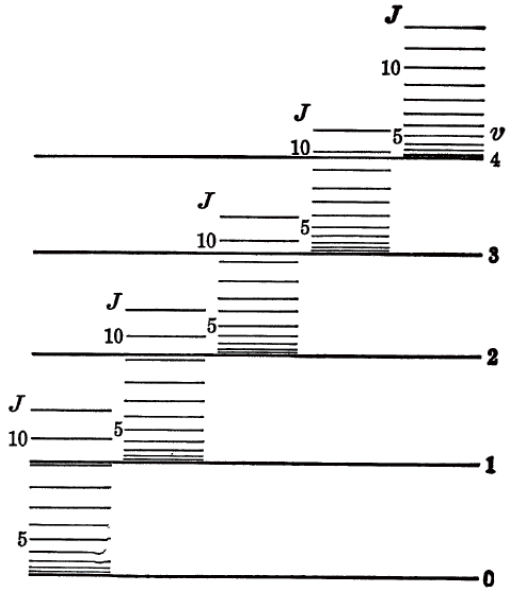

Figure 2.1: Energy levels of the vibrationg rotator according to Reference [20]. The rotational energy separation increases as J increases (short horizontal lines), and the vibrational energy separation decreases as v increases (long horizontal lines).

The approximation stated previously is based on the assumption that the vibrational and rotational motions are independent. However, in reality, at higher energy levels the vibrational motion causes a changing value of moment of inertia, which also affects the rotational motion. Thus the vibrating rotator model must be taken into account. The rotational and centrifugal distortion constants B_e and D_e in Equation 2.16 are replaced by B_v and D_v which include vibrational terms [20],

$$B_v = B_e - \alpha_e \left(v + \frac{1}{2}\right) + \gamma_{e1} \left(v + \frac{1}{2}\right)^2 + \gamma_{e2} \left(v + \frac{1}{2}\right)^3 + \cdots , \tag{2.21a}$$

$$D_v = D_e + \beta_e \left(v + \frac{1}{2}\right) + \beta_{e1} \left(v + \frac{1}{2}\right)^2 + \beta_{e2} \left(v + \frac{1}{2}\right)^3 + \cdots . \tag{2.21b}$$

The spectroscopic constants ω_e, $\omega_e x_e$, B_e, α_e, D_e, β_e, etc. can be determined by analysis of spectroscopic data.

Thus the total energy of a particular rotational and vibrational (ro-vibrational) level including all terms of G_v, B_v, and D_v is given by

$$E(v, J) = T_e + G_v + B_v J(J+1) - D_v[J(J+1)]^2 + \cdots , \tag{2.22}$$

where T_e is the energy of the minimum of the electronic state, which is the same as E_e in Equation 2.14. In addition, higher orders of $J(J+1)$ need to be retained in order to accurately reproduce the observed energy levels. The term values of the vibrating rotator can be expressed in a more compact form using a double power series in terms of the vibrational and rotational quantum number, v and J, respectively, known as the Dunham expansion [27]

$$E(v, J) = \sum_{l,m} Y_{lm} \left(v + \frac{1}{2} \right)^l \left[J(J+1) - \Omega^2 \right]^m . \tag{2.23}$$

where the Y_{lm} terms are called the Dunham's coefficients and can be determined from the measured spectroscopic data, which is discussed in Section 5.3. Ω is the quantum number describing the component of the total electronic spin and orbital angular momentum along the internuclear axis. In Hund's case (a), the component of the total electron spin angular momentum, $\boldsymbol{S}$, along the internuclear axis is Σ, and the component of the total electron orbital angular momentum, $\boldsymbol{L}$, along the internuclear axis is Λ, so $\Omega = \Sigma + \Lambda$. In Hund's case (c), Ω is the component of the total electronic angular momentum, $\boldsymbol{L} + \boldsymbol{S}$, along the internuclear axis. Thus the expectation value of the square of the nuclear rotation has been replaced here by $[J(J+1) - \Omega^2]\hbar^2$. In Hund's case (b), $[J(J+1) - \Omega^2]$ is replaced by $[N(N+1) - \Lambda^2]$, where $\boldsymbol{N}$ is the sum of the nuclear rotation and $\boldsymbol{\Lambda}$. The angular momentum coupling cases are discussed in Section 2.4.

2.4 Angular Momenta and Hund's Cases

The previous discussion was about the electronic motions in the nuclear fields. In a real molecule, rotation and vibration take place simultaneously with the electronic motions. The motions of the nuclei and the motions of the electrons traveling in the nuclear field lead to several different angular momentum vectors. These angular momentum vectors can couple in different ways. The Hund's cases (a), (b), (c), (d), and (e) describe five typical coupling schemes for coupling the angular momentum vectors in diatomic molecules [28]. In a molecule, the description between two of Hund's cases is often necessary.

Figure 2.2 depicts the first four coupling schemes of angular momenta in Hund's cases. The angular momentum operators are described in Table 2.1.

Table 2.1: List of the angular momenta of diatomic molecules frequently used in Hund's coupling cases.

Symbol	Description
$\boldsymbol{L}$	The total electron orbital angular momentum
$\boldsymbol{S}$	The total electron spin angular momentum
Λ	The projection of $\boldsymbol{L}$ onto the internuclear axis
Σ	The projection of $\boldsymbol{S}$ onto the internuclear axis
Ω	The projection of the combination of $\boldsymbol{L}$ and $\boldsymbol{S}$ onto the internuclear axis
$\boldsymbol{R}$	The nuclear rotational angular momentum (not the internuclear axis)
$\boldsymbol{I}$	The total nuclear spin angular momentum
$\boldsymbol{J} = \boldsymbol{R} + \boldsymbol{L} + \boldsymbol{S}$	The total angular momentum excluding nuclear spin
$\boldsymbol{N} = \boldsymbol{J} - \boldsymbol{S} = \boldsymbol{R} + \boldsymbol{L}$	The total angular momentum excluding electron and nuclear spin
$\boldsymbol{F} = \boldsymbol{J} + \boldsymbol{R} + \boldsymbol{L} + \boldsymbol{S}$	The grand total angular momentum

Hund's case (a). In Hund's case (a), each of $\boldsymbol{L}$ and $\boldsymbol{S}$ couples strongly to the internuclear axis. The precession of $\boldsymbol{L}$ and $\boldsymbol{S}$ around the internuclear axis is so fast that only their projections onto the internuclear axis, Λ and Σ, survive. Thus Λ and

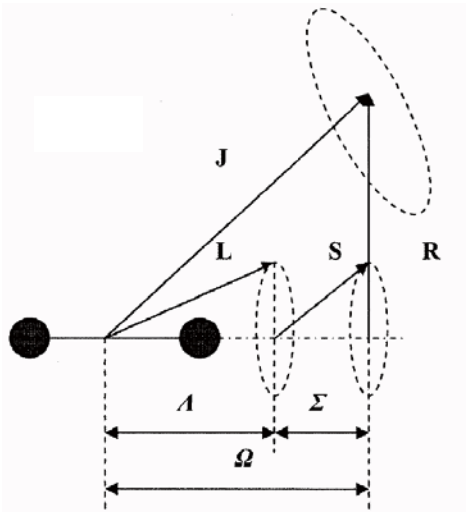

Hund's case (a)

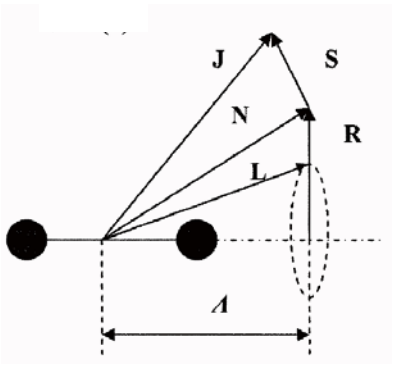

Hund's case (b)

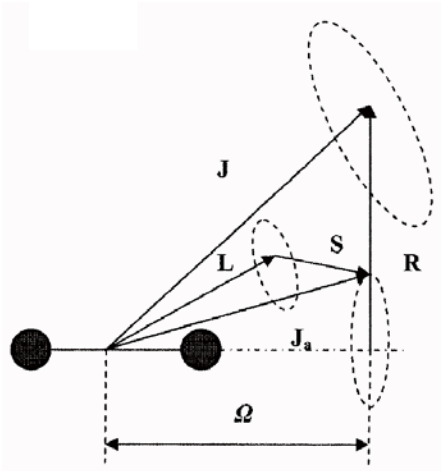

Hund's case (c)

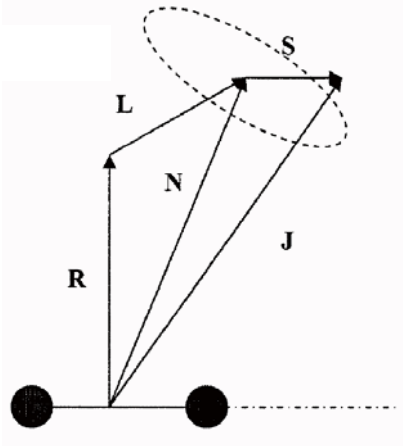

Hund's case (d)

Figure 2.2: Hund's coupling cases (a), (b), (c), and (d). The angular momentum vectors are described in Table 2.1.

Σ are good quantum numbers, rather than L and S. The quantum number Λ takes on the values in terms of the quantum value of L,

$$\Lambda = |M_L| = 0, 1, 2, \cdots, L,$$

and the quantum number Σ takes on the values in terms of the quantum value of S,

$$\Sigma = -S, -S+1, \cdots, S-1, S.$$

The sum of the projections $\Omega = \Lambda + \Sigma$ takes on the values

$$\Omega = |\Lambda - S|, |\Lambda - S| + 1, \cdots, \Lambda + S.$$

In this case $\boldsymbol{\Omega}$ couples to $\boldsymbol{R}$ and form a resultant $\boldsymbol{J}$, as shown in Figure 2.2.

The notation referring to a particular electronic state ${}^{2S+1}\Lambda^{\pm}_{\Omega}$, stated in the beginning of Section 2.3, is based on the angular momentum vectors defined in the Hund's case (a).

Hund's case (b). In Hund's case (b), only $\boldsymbol{L}$ couples strongly to the internuclear axis and forms Λ. $\boldsymbol{S}$ is very weakly coupled or not coupled to the internuclear axis. Therefore Ω is not a good quantum number because Σ is not defined. In this case, $\boldsymbol{\Lambda}$ couples to $\boldsymbol{R}$ and form a resultant $\boldsymbol{N}$, and $\boldsymbol{N}$ couples to $\boldsymbol{S}$ to form $\boldsymbol{J}$, as shown in Figure 2.2. Hund's case (b) generally applies to the case when $\Lambda = 0$, and $\boldsymbol{S}$ is not coupled to the internuclear axis. And also in lighter molecules, even if $\Lambda \neq 0$, $\boldsymbol{S}$ is weakly coupled to the internuclear axis.

The notation of the states described by Hund's case (b) is similar to Hund's case (a) but without the Ω subscript, ${}^{2S+1}\Lambda^{\pm}$.

Hund's case (c). In Hund's case (c), the interaction between $\boldsymbol{L}$ and $\boldsymbol{S}$ (spin-orbit interaction) is stronger than the interaction with the internuclear axis. Therefore neither L nor S are good quantum numbers because Λ and Σ are not defined. In this case, $\boldsymbol{L}$ and $\boldsymbol{S}$ couple first and form a resultant $\boldsymbol{J_a}$, which then couples to the internuclear axis with a component Ω. The electronic angular momentum and the nuclear rotational angular momentum, $\boldsymbol{\Omega}$ and $\boldsymbol{R}$, further form $\boldsymbol{J}$, as shown in Figure 2.2.

The notation ${}^{2S+1}\Lambda_{\Omega}^{\pm}$ is not rigorously correct for the states described by Hund's case (c). We use a numbering index n to label a proper state. For a state $n(\Omega)$, there are $n-1$ states below it with the same value of Ω.

Hund's case (d). In Hund's case (d), the coupling between $\boldsymbol{L}$ and the internuclear axis is very weak while that between $\boldsymbol{L}$ and the rotation is strong. In this case, $\boldsymbol{L}$ and $\boldsymbol{R}$ couple first and form a resultant $\boldsymbol{N}$. $\boldsymbol{N}$ and $\boldsymbol{S}$ then further form $\boldsymbol{J}$, as shown in Figure 2.2.

This dissertation only briefly discusses the Hund's cases (a), (b), (c), and (d). The more detailed description of all five coupling cases can be found in References [20, 22, 26].

2.5 Selection Rules

The transitions between ro-vibrational levels of different electronic states can be realized by external electric or magnetic fields. The probabilities and intensities of the transition are determined by the matrix elements of the transition dipole moment operator $\langle\Psi_i|\mu_e|\Psi_j\rangle$. We apply the symmetry operator σ to the integral and obtain

$$\sigma\langle\Psi_i|\mu_e|\Psi_j\rangle = (-1)^{N_1+N_2+N_3}\langle\Psi_i|\mu_e|\Psi_j\rangle, \tag{2.24}$$

where $N_1 + N_2 + N_3$ characterize the parities of the wavefunctions and the dipole moment under the symmetry operation. When $N_1 + N_2 + N_3$ is an odd integer, the matrix element in Equation 2.24 becomes zero.

For homonuclear diatomic molecules, the electric dipole selection rules are as follows [20],

1. $\Delta\Lambda = 0, \pm 1$. The transitions such as $\Sigma \leftrightarrow \Sigma, \Sigma \leftrightarrow \Pi, \Pi \leftrightarrow \Pi, \Pi \leftrightarrow \Delta, \cdots$ are allowed, while the transitions whose Λ changes by more than one such as $\Sigma \leftrightarrow \Delta, \Pi \leftrightarrow \Phi, \cdots$ are forbidden.

Only $\Sigma^+ \leftrightarrow \Sigma^+,\ \Sigma^- \leftrightarrow \Sigma^-$ transitions are allowed.

2. $\Delta S = 0$. Only the transitions between the electronic states with the same multiplicity are allowed. The transitions between singlet and triplet states are forbidden. However, when spin-orbit interaction is taken into account, this nominal rule breaks down, which is discussed in Chapter 3 and 4.

3. $g \leftrightarrow u$. The transitions of $g \leftrightarrow g$ states and $u \leftrightarrow u$ states are forbidden.

4. $a \leftrightarrow a,\ s \leftrightarrow s$. The transitions between symmetric and antisymmetric rotational levels are forbidden.

5. $e \leftrightarrow f$, for $\Delta J = 0$;

$e \leftrightarrow e,\ f \leftrightarrow f$, for $\Delta J = \pm 1$.

In the fifth selection rule, $\Delta J = J' - J''$ is the difference of the rotational quantum numbers between the upper level J' and the lower level J''. The typical molecular transitions with different ΔJ values are denoted as

$$P(J'') \quad \text{for} \quad \Delta J = -1,$$

$$Q(J'') \quad \text{for} \quad \Delta J = 0,$$

$$R(J'') \quad \text{for} \quad \Delta J = +1.$$

The further selection rules on the rotational quantum number J are

$$\Delta J = \pm 1 \qquad \text{for transition } \Sigma \to \Sigma,$$

$$\Delta J = 0, \pm 1 \qquad \text{for all other transitions, except } J = 0 \not\leftrightarrow J = 0.$$

References

[18] B. H. Bransden, and C. J. Joachain, *Physics of atoms and molecules* (John Wiley & Sons, New York, 1983).

[19] I. N. Levine, *Molecular spectroscopy* (John Wiley & Sons, New York, 1975).

[20] G. Herzberg, *Molecular spectra and molecular structure I, Spectra of diatomic molecules* (Krieger Publishing Company, Malabar, Florida, 1989).

[21] J. I. Steinfeld, *Molecules and radiation: an introduction to modern molecular spectroscopy* (Dover, New York, 1985).

[22] H. Lefebvre-Brion, and R. W. Field, *Perturbations in the spectra of diatomic molecules* (Academic Press, Orlando, 1986).

[23] M. Born, and R. Oppenheimer, Ann. Phys. **84**, 4571 (1927).

[24] J. Brown, J. Hougen, K.-P. Huber, J. Johns, I. Kopp, H. Lefebvre-Brion, A. Merer, D. Ramsay, J. Rostas, and R. Zare, J. Mol. Spectrosc. **55**, 500 (1975).

[25] H. Lefebvre-Brion, and R. W. Field, *The spectra and dynamics of diatomic molecules* (Elsevier, Amsterdam, 2004).

[26] P. F. Bernath, *Spectra of atoms and molecules* (Oxford University Press, Oxford, 1995).

[27] J. L. Dunham, Phys. Rev. **41**, 721 (1932).

[28] F. Hund, Z. Phys. **42**, 93 (1927).

CHAPTER 3

THE THEORY BEHIND THE QUANTUM CONTROL OF THE SPIN-ORBIT INTERACTION

3.1 Introduction

Quantum interference effects, such as Autler-Townes (AT) splitting and electromagnetically induced transparency (EIT), provide powerful probes of fundamental molecular properties, such as determining the absolute transition dipole moment matrix elements of molecular transitions, controlling quantum state singlet-triplet character, and demonstrating frequency domain quantum control on predissociation, etc.

Singlet and triplet energy levels mixed by the spin-orbit interaction can be used as *gateway* levels in spectroscopy to gain access to otherwise "dark" triplet states from a singlet ground state [25, 29–33]. The degree of mixing depends on the strength of the spin-orbit interaction as well as the energy separation between the interacting states. Thus the coupling laser E field amplitude that tunes the singlet-triplet mixing

coefficients is used as a control knob for opening the gateway of the mixed pair of levels "wider".

3.2 The Doppler Broadening Effect

Figure 3.1 shows our experimental model of $^6Li_2$ 3-level cascade excitation. By fre-

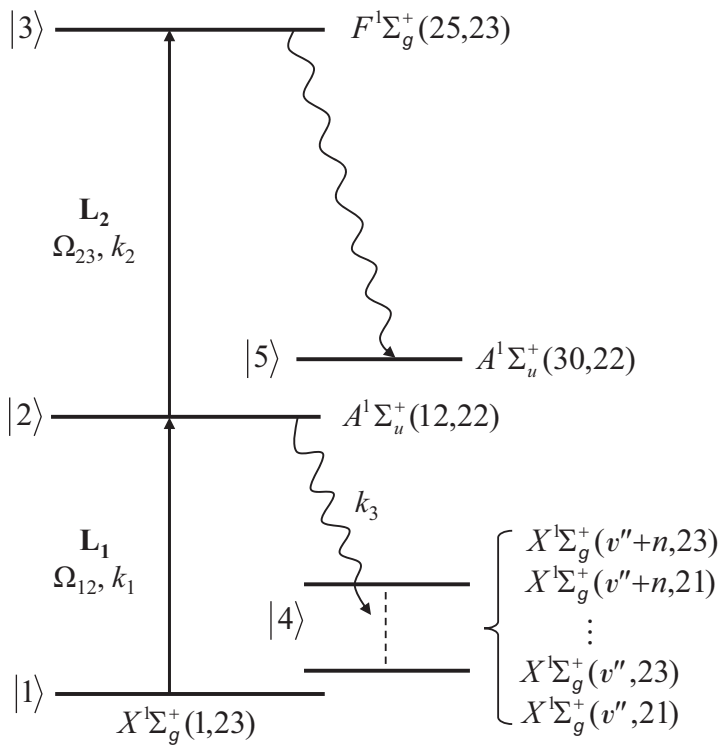

Figure 3.1: The model of $^6Li_2$ 3-level cascade excitation. The pump laser L_1 couples levels $|1\rangle - X^1\Sigma_g^+(v''=1, J''=23)$ and $|2\rangle - A^1\Sigma_u^+(v'=12, J'=22)$, while the coupling laser L_2 couples levels $|2\rangle - A^1\Sigma_u^+(v'=12, J'=22)$ and $|3\rangle - F^1\Sigma_g^+(v=25, J=23)$. Here Ω_{ij} and k_i represent the Rabi frequency and wavenumber of each laser, respectively.

quency domain control, our pump laser L_1 excites the molecules from the ground state $X^1\Sigma_g^+$ to intermediate state $A^1\Sigma_u^+$ here. Then the coupling laser L_2 excites molecules from the $A^1\Sigma_u^+$ state to the $F^1\Sigma_g^+$ state. The fluorescence from the upper state results

in an optical-optical double resonance (OODR) signal. The quantum numbers of the ro-vibrational energy levels in each state are shown in Figure 3.1.

Figure 3.2 shows a portion of the resolved fluorescence following excitation from the $X^1\Sigma_g^+$ state to the $A^1\Sigma_u^+$ state. When the pump laser L_1 is tuned through the

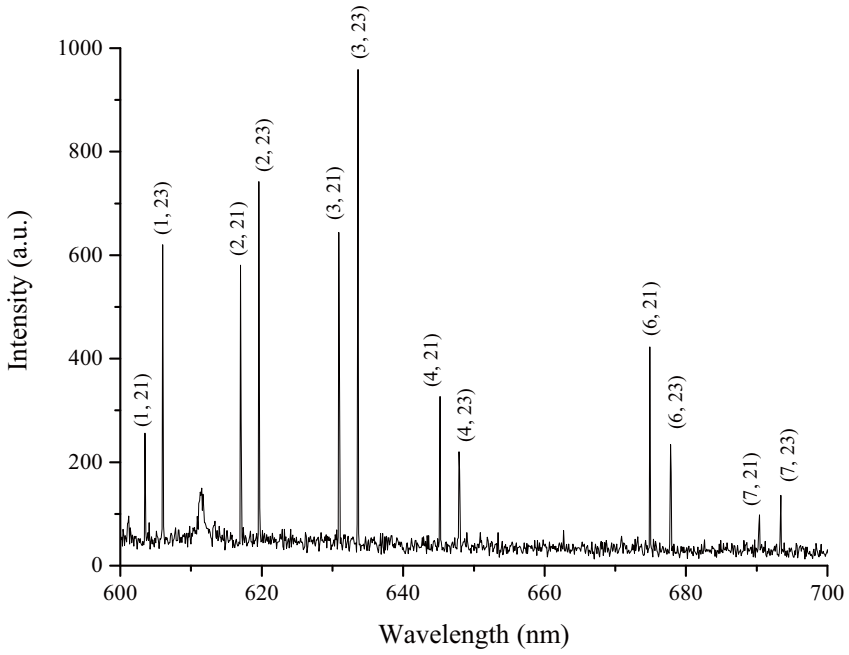

Figure 3.2: A portion of the resolved fluorescence spectrum of $^6Li_2$. Laser L_1 excites the molecules from the thermally populated ground state ro-vibrational level $|1\rangle - X^1\Sigma_g^+(v'' = 1, J'' = 23)$ to the intermediate level $|2\rangle - A^1\Sigma_u^+(v' = 12, J' = 22)$.

pump transition, the recorded lineshape is due to the *Doppler broadening* effect as shown in Figure 3.3. The distribution of radiation with a spread of frequencies is well described by the Gaussian function [34],

$$g(\nu) = \left(\frac{4\ln 2}{\pi\Delta\nu_{\rm D}^2}\right)^{1/2} \exp\left[\frac{-4\ln 2(\nu-\nu_0)^2}{\Delta\nu_{\rm D}^2}\right], \tag{3.1}$$

where $\nu_0 = 494656.6045\,\text{GHz}$ is the center frequency of the lineshape, and $\Delta\nu_{\rm D} = 3.1083\,\text{GHz}$ is the full width at half-maximum (FWHM) of the Doppler-broadened

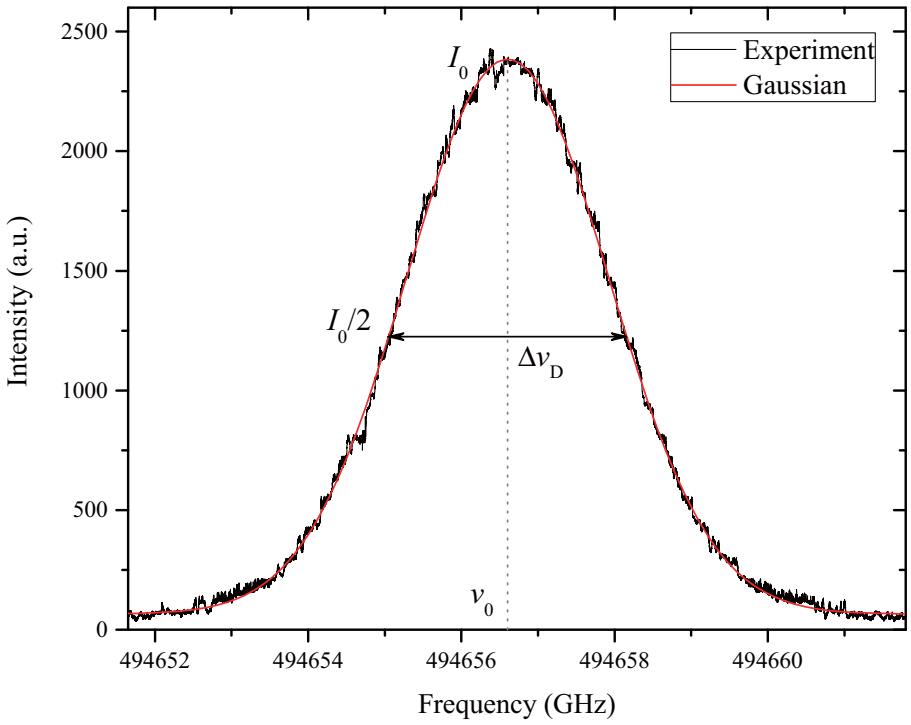

Figure 3.3: Doppler Broadening, when observing fluorescence from the intermediate level $A^1\Sigma_u^+(v' = 12, J' = 22)$ to the thermally populated ground state ro-vibrational level $X^1\Sigma_g^+(v'' = 6, J'' = 21)$ of $^6Li_2$.

line function for molecular mass m_0 at temperature T,

$$\Delta\nu_{\mathrm{D}} = \sqrt{\frac{8k_{\mathrm{B}}T\ln 2}{m_0c^2}}\nu_0. \tag{3.2}$$

The temperature of the system can then be calculated by,

$$T = \left(\frac{\Delta\nu_{\mathrm{D}}}{\nu_0}\right)^2 \frac{m_0c^2}{8k_{\mathrm{B}}\ln 2}. \tag{3.3}$$

The red line in Figure 3.3 is a computational curve fit to our experimental data, which gives 900 K for the value of the temperature of the sample.

3.3 Beam Profile and the Amplitude E of Electric Field of a Laser

The laser beam electric field amplitude has a Gaussian radial distribution as shown in Figure 3.4. The distribution has the form

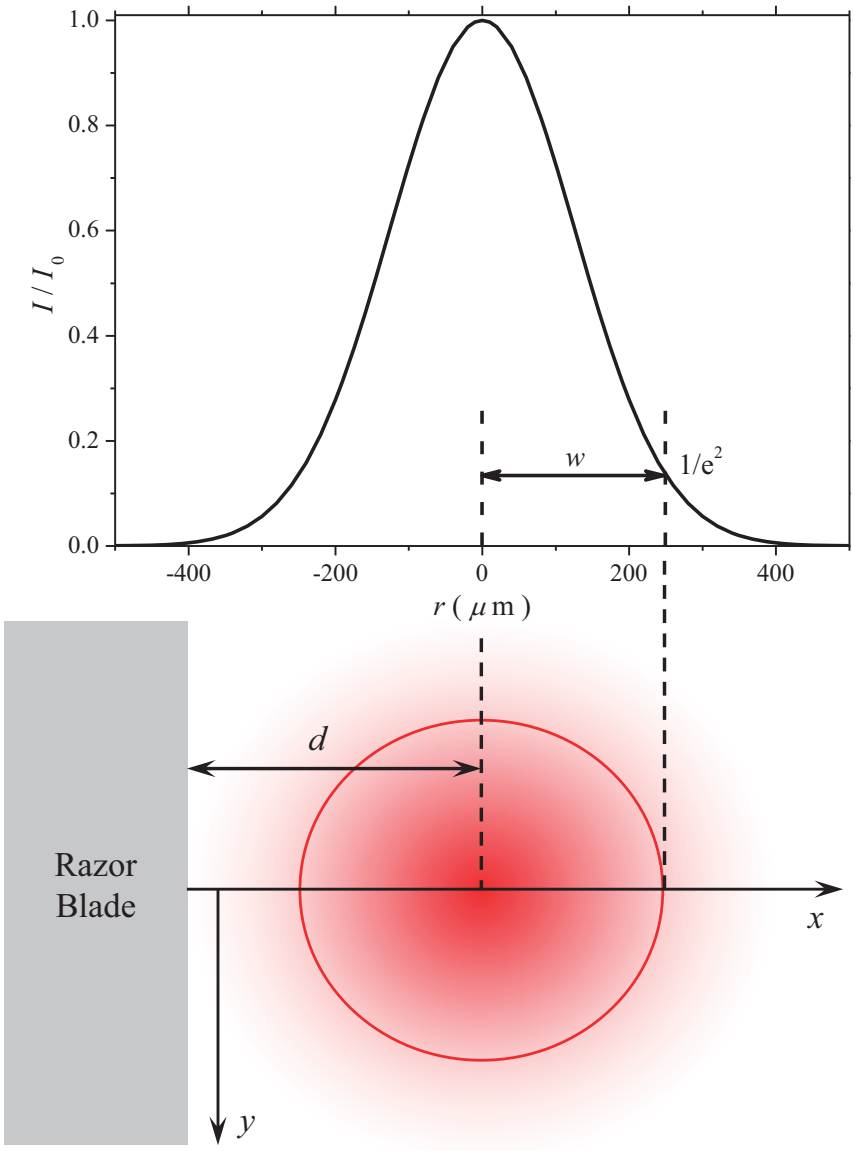

Figure 3.4: Illustration of the Gaussian distribution of the intensity of the laser electric field and the razor blade technique.

$$E(r) = E_0 \exp\left(-\frac{r^2}{w^2}\right), \tag{3.4}$$

where E_0 is the amplitude of the electric field at the center of the laser beam E field radial profile.

The total power of a laser beam can be written as the integral

$$P_{\text{tot}} = \int_0^{+\infty} \int_0^{2\pi} I(r) r \mathrm{d}r \mathrm{d}\varphi, \tag{3.5}$$

in polar coordinates r and φ. And $I(r)$ can be expressed as

$$I(r) = \frac{1}{2} c\varepsilon_0 E(r)^2. \tag{3.6}$$

E_0 can be further determined by experimentally measuring the total power P_{tot} and the beam waist w by using

$$E_0 = \sqrt{\frac{2}{c\varepsilon_0}} \cdot \sqrt{\frac{2P_{\text{tot}}}{\pi w^2}}. \tag{3.7}$$

The beam spot size, or the beam waist, w is defined as the radius at the $1/e^2$ intensity of the maximum value I_0 (Figure 3.4). The beam waist can be measured by using the razor blade technique [35]. Using this method, the power of the laser beam blocked by the razor blade at a distance d is denoted by

$$P(d) = \int_{-\infty}^{d} \int_{-\infty}^{+\infty} I(x, y) \mathrm{d}y \mathrm{d}x. \tag{3.8}$$

By taking into account Equations 3.4 and 3.6 in Cartesian coordinates x and y, Equation 3.8 can be expressed as

$$P(d) = \frac{\pi}{4} w^2 I_0 \left[1 + \operatorname{erf}\left(\frac{\sqrt{2}d}{w}\right)\right], \tag{3.9}$$

where

$$I_0 = \frac{1}{2} c\varepsilon_0 E_0^2.$$

When $d \to \infty$,

$$\lim_{d\to\infty} P(d) = \frac{\pi}{2} w^2 I_0 = P_{\text{tot}}.$$

By taking d_{25} and d_{75} as the positions of the razor blade at 25% and 75% of the maximum laser beam power, respectively, the ratios

$$\frac{P(d_{25})}{P_{\text{tot}}} = \frac{1}{4} = \frac{1}{2}\left[1 + \text{erf}\left(\frac{\sqrt{2}d_{25}}{w}\right)\right], \tag{3.10a}$$

$$\frac{P(d_{75})}{P_{\text{tot}}} = \frac{3}{4} = \frac{1}{2}\left[1 + \text{erf}\left(\frac{\sqrt{2}d_{75}}{w}\right)\right], \tag{3.10b}$$

can be used to obtain the results

$$C = -\frac{\sqrt{2}d_{25}}{w}, \tag{3.11a}$$

$$C = \quad \frac{\sqrt{2}d_{75}}{w}, \tag{3.11b}$$

where C is the solution of error function

$$\text{erf}(C) = \frac{1}{2},$$

with $C \approx 0.47$. The beam waist w can be determined by adding the Equations 3.11 and expressed in terms of C, d_{25} and d_{75},

$$w = \frac{1}{\sqrt{2}C}(d_{75} - d_{25}).$$

By substituting P_{tot} and w into Equation 3.7, the amplitude of the electric field of the laser beam E_0 can be calculated.

3.4 Electromagnetically Induced Transparency and the Autler-Townes Effect

When a strong coupling laser is tuned to resonance with one of the two transitions, the absorption of the weak probe laser displays a dramatic decrease as the probe laser frequency is tuned across the resonance. This phenomenon is called electromagnetically induced transparency (EIT) [5, 6, 36].

The Autler-Townes (AT) splitting effect [7], which is also known as AC Stark effect, can be realized in gas-phase molecules by using the pump and tunable probe lasers to create sub-Doppler double resonance of an upper ro-vibrational level [11].

The excitation scheme is shown in Figure 3.1. The experimental setup is described in Figure 3.5. The pump laser (L_1) is operated with Kiton Red dye and is modulated

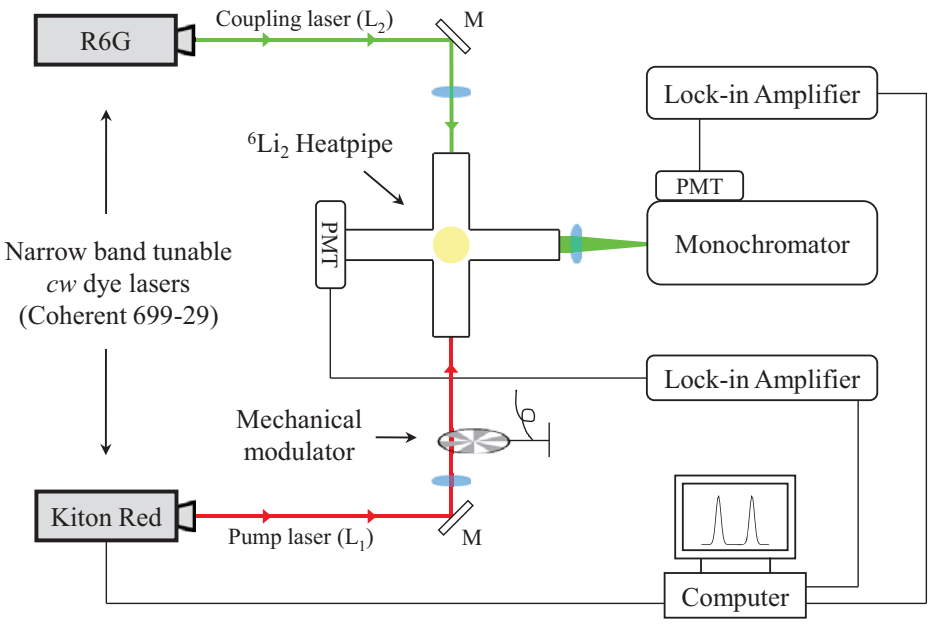

Figure 3.5: Experimental setup for EIT and the Autler-Townes effect of $^6Li_2$ 3-level cascade excitation. The pump laser (L_1) and the coupling laser (L_2) counter-propagate and overlap at the center of the heatpipe. The total fluorescence is detected by the PMT with a filter. And the monochromator detects the resolved fluorescence.

before going through the heatpipe. The coupling laser (L_2) is operated using the R6G dye and counter-propagates relative to the pump laser L_1 in the heatpipe. It is overlapped with the pump laser beam. Both of the lasers are Coherent 699-29 narrow band tunable continous wave (cw) ring dye lasers. The photomutiplier (PMT) with a filter is used to detect the total fluorescence. Meanwhile the monochromator (SPEX 1404) detects the resolved fluorescence. A mechanical modulator is used on the pump laser to improve the signal to noise by phase sensitive detection with lock-in amplifiers.

Figure 3.6 shows the results of the double resonance signal we obtained. Fig-

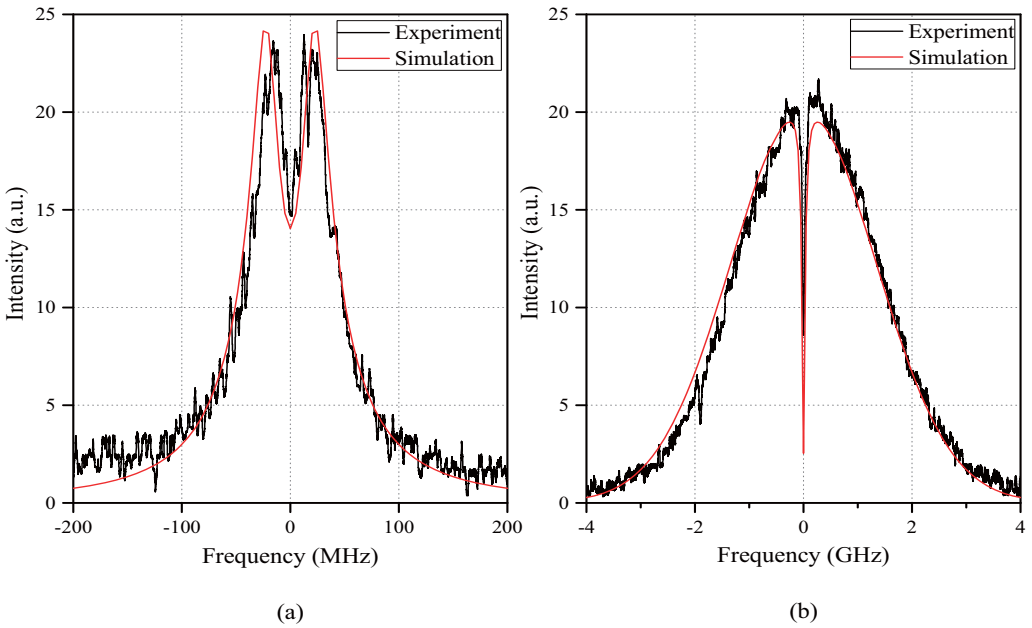

Figure 3.6: (a) AT splitting, observation of fluorescence from the excited level $|3\rangle - F^1\Sigma_g^+(v = 25, J = 23)$ to the intermediate level $A^1\Sigma_u^+(v' = 30, J' = 22)$; (b) EIT, observation of fluorescence from the intermediate level $|2\rangle - A^1\Sigma_u^+(v' = 12, J' = 22)$ to the thermally populated ground state ro-vibrational level $X^1\Sigma_g^+(v'' = 6, J'' = 21)$, in $^6Li_2$.

ure 3.6(a) illustrates the Autler-Townes splitting spectrum, which consists of the total fluorescence from the excited state to the intermediate state as the coupling laser (L_2) frequency is scanned, and Figure 3.6(b) depicts Electromagnetically Induced Transparency (EIT), which is observed by monitoring fluorescence from the

intermediate state to the ground state as the pump laser (L_1) frequency is scanned. The linewidth of the AT splitting spectral line is about 150 MHz, and the width of splitting is related to the Rabi frequency of the coupling laser. The EIT linewidth is about 3 GHz and is dominated by *Doppler broadening*, and the width of the dip is about 100 MHz.

The intensity distribution [37, 38] is described as

$$I_i(\Delta_1, \Delta_2, r) = \sum_M \int_{-\infty}^{\infty} \rho_{ii}^M(r, v_z) N(v_z) \mathrm{d}v_z, \tag{3.12}$$

where Δ_1 and Δ_2 are velocity dependent detunings of the probe and coupling lasers from the molecular transition frequencies ω_{ij},

$$\Delta_1 = \omega_{21} - \omega_1 + k_1 v_z, \tag{3.13a}$$

$$\Delta_2 = \omega_{32} - \omega_2 + k_2 v_z. \tag{3.13b}$$

and ρ_{ii} is the population of level i $(i = 2, 3)$ and magnetic sublevel M,

$$\begin{aligned}
\rho_{22}^M(r, v_z) &= \frac{-\Omega_{1,M}^2}{2F_M(\Delta_2)} \mathrm{Im} \left[\frac{(\Delta_1 + \Delta_2 + i\gamma_{13}) \left[\Delta_2^2 + \gamma_{23}^2 + \frac{\Omega_{2,M}^2 \gamma_{23}}{2W_3} \right]}{(\Delta_1 + \Delta_2 + i\gamma_{13})(\Delta_1 + i\gamma_{12}) - \Omega_{2,M}^2/4} \right. \\
&\left. + \frac{\frac{\Omega_{2,M}^2}{4} \left(1 - \frac{W_{32}}{W_3} \right) (\Delta_2 - i\gamma_{23})}{(\Delta_1 + \Delta_2 + i\gamma_{13})(\Delta_1 + i\gamma_{12}) - \Omega_{2,M}^2/4} \right], \qquad (3.14a) \\
\rho_{33}^M(r, v_z) &= \frac{\Omega_{1,M}^2 \Omega_{2,M}^2}{8W_3 F_M(\Delta_2)} \mathrm{Im} \left[\frac{-2\gamma_{23}(\Delta_1 + \Delta_2 + i\gamma_{13})}{(\Delta_1 + \Delta_2 + i\gamma_{13})(\Delta_1 + i\gamma_{12}) - \Omega_{2,M}^2/4} \right. \\
&\left. + \frac{W_2(\Delta_2 - i\gamma_{23})}{(\Delta_1 + \Delta_2 + i\gamma_{13})(\Delta_1 + i\gamma_{12}) - \Omega_{2,M}^2/4} \right], \qquad (3.14b)
\end{aligned}$$

with

$$F_M(\Delta_2) \equiv W_2(\Delta_2^2 + \gamma_{23}^2 + \frac{\Omega_{2,M}^2 \gamma_{23}}{2W_3} + \frac{\Omega_{2,M}^2}{2} \gamma_{23}(1 - \frac{W_{32}}{W_3}), \tag{3.15}$$

where W_i is the damping rate of the ith level, including both radiative and collisional contributions.

Table 3.1 lists all the parameters needed for the simulation. After theoretical simulation of the experimental data, we obtain the line shapes shown as the red lines in Figure 3.6.

Table 3.1: List of all parameters of the pump and probe lasers used in the simulation of the cascade scheme experiment with the probe transition to $F^1\Sigma_g^+$.

Parameter	Value	
Temperature (°C)	$T = 652$	
Beam Waist (μm)	$w = 127.5$	
Rabi Frequency (MHz)	$\Omega_{12} = 32$	$\Omega_{23} = 187$
Wavenumber (cm^{-1})	$k_1 = 16500.25$	$k_2 = 17601.42$
Decay Rate (s^{-1})	$\gamma_2 = 5.2868 \times 10^7$ $\gamma_{21} = 4.9420 \times 10^5$	$\gamma_3 = 8.9062 \times 10^7$ $\gamma_{32} = 9.2030 \times 10^5$

3.5 The Spin-Orbit Interaction and the Gateway Effect

In order to obtain a more accurate description of the energy level structure of a homonucler molecular system, the relativistic effects due to the following interactions have to be taken into account [22]:

1. Spin-orbit interaction: the interaction between the spin and orbital angular momenta of the electrons,

2. Spin-rotation interaction: the interaction between the electron spin and the rotational angular momenta of the nuclei,

3. Spin-spin interaction: the interaction between the spins of different electrons.

These interactions create the mixing of electronic states of different spin multiplicity, thus causing violation of approximate selection rules. An example is shown in Figure 3.7. Although the dipole selection rule on spin $\Delta S = 0$ prohibits direct

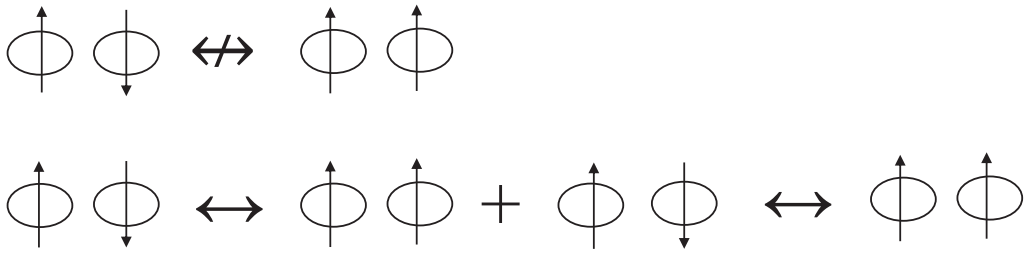

Figure 3.7: The approximate selection rule, $\Delta S = 0$, prohibits direct transitions between singlet and triplet states. However, due to the spin-orbit interaction, singlet triplet levels with the same J could couple together, and make the transition between singlet and triplet states possible.

excitation between states of different spins (singlet $\not\leftrightarrow$ triplet), singlet and triplet energy levels with the same rotational quantum number J can couple together by the spin-orbit interaction creating levels of mixed singlet-triplet character, and make the nominally forbidden transitions possible.

Under certain conditions, the spin-orbit interactions have been demonstrated even for molecules with relatively light nuclei with weakly coupled spin and orbital angular momenta. Therefore the spin-orbit interaction is small (i.e. Lithium, $\sim$0.1 cm^{-1} [39]). For example, in the work of Ahmed *et al.* [16, 40], the spin-orbit interaction couples the nonrelativistic $G^1\Pi_g$ and $1^3\Sigma_g^-$ potentials and creates a mixing mechanism for the ro-vibrational levels of the $G^1\Pi_g$ and $1^3\Sigma_g^-$ states.

Compared with other interactions, such as the spin-rotation and the spin-spin interactions, the spin-orbit interaction for Lithium is much larger. Thus the correction term due to the spin-orbit interaction needs to be added to the Hamiltonian of the

system according to perturbation theory [22],

$$\widehat{H}_{\mathrm{SO}} = \frac{\alpha^2}{2} \sum_N \sum_i \frac{Z_N}{r_{iN}^3} \boldsymbol{l}_{iN} \cdot \boldsymbol{s}_i - \frac{\alpha^2}{2} \sum_{i,j,i\neq j} \left[\frac{1}{r_{ij}^3} (\boldsymbol{r}_{ij} \times \boldsymbol{p}_i)(\boldsymbol{s}_i + 2\boldsymbol{s}_j) \right], \tag{3.16}$$

where α is the fine-structure constant, $\alpha = e^2/\hbar c$, Z_N is the number of protons in nucleus N, $\boldsymbol{r}_{iN}$ is the distance from electron i to nucleus N, $\boldsymbol{p}_i$ is the momentum of electron i in a molecule-fixed frame, $\boldsymbol{s}_i$ is the spin angular momentum of the electron i and $\boldsymbol{l}_{iN} = \boldsymbol{r}_{iN} \times \boldsymbol{p}_i$ is the orbital angular momentum of electron i about nucleus N.

In the Equation 3.16, the first term of $\widehat{H}_{\mathrm{SO}}$ represents the spin-same-orbit interaction of each electron in the field of the bare nuclei. The second term is the spin-other-orbit interaction, which is due to inter-electronic interactions and is opposite to the first term. And since the spin-other-orbit interaction can be incorporated into the first term as a screening effect [41], the spin-orbit Hamiltonian $\widehat{H}_{\mathrm{SO}}$ of Equation 3.16 can be simplified as [42]

$$\widehat{H}_{\mathrm{SO}} = \sum_i \widehat{a}_i \boldsymbol{l}_i \cdot \boldsymbol{s}_i, \tag{3.17}$$

with

$$\widehat{a}_i \boldsymbol{l}_i = \sum_N \frac{\alpha^2}{2} \frac{Z_{\mathrm{eff},N}}{r_{iN}^3} \boldsymbol{l}_{iN}, \tag{3.18}$$

where $Z_{\mathrm{eff},N}$ is the inter-electronic interaction that screens the nuclear charge [43], and therefore signifies the effective charge of the nucleus N.

In the work of Ahmed *et al.* [16, 40], the quantum control of the spin-orbit interaction of the alkali-metal dimer ($^7Li_2$) in a *cw* optical field is observed. The mixed $G^1\Pi_g \sim 1^3\Sigma_g^-$ pair of ro-vibrational levels is an example of the singlet-triplet mixing. These levels can be used as "*gateway*" or "*windows*" levels [29, 44–47] for transferring population between singlet and triplet manifolds which occurs by way of collisional pathways through levels of mixed character.

Figure 3.8 shows a model of the gateway effect [45]. The pump laser excites the

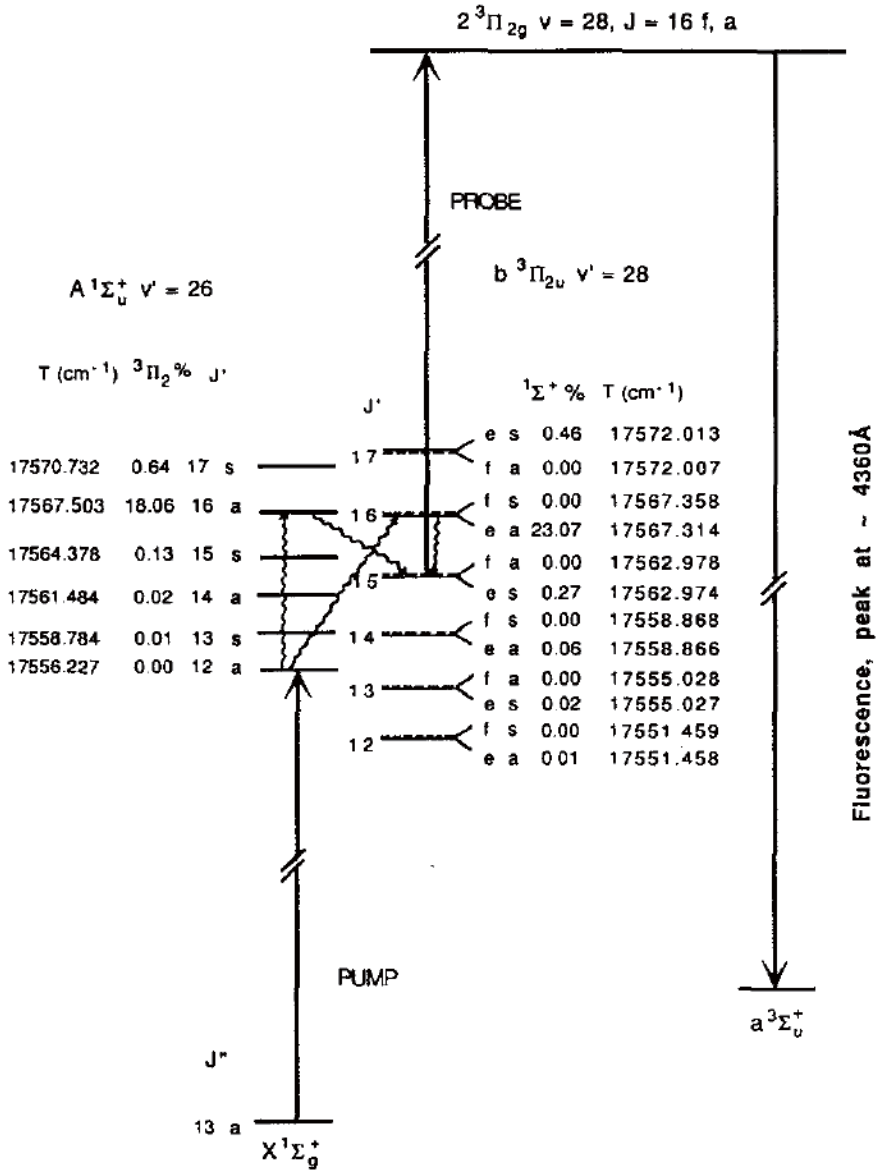

Figure 3.8: The *gateway* effect according to Reference [45]. The pump laser excites the population from the ground $X^1\Sigma_g^+$ state to the intermediate $A^1\Sigma_u^+$ state. During collision, the population flows to the closeby triplet state rotational manifold, following the collisional propensity rule $\Delta J = \pm 2, \pm 4, \cdots$. The nearly degenerate $A^1\Sigma_u^+$ and $b^3\Pi_{2u}$ levels with the same rotational quantum number J can couple together by the spin-orbit interaction. When a pair of ro-vibrational levels of two electronic states is appreciably mixed, a *gateway* is created, leading to a pathway for the transition from the mixing intermediate $A^1\Sigma_u^+ \sim b^3\Pi_{2u}$ state to the $2^3\Pi_{2g}$ state.

population from the ground $X^1\Sigma_g^+$ state to the intermediate $A^1\Sigma_u^+$ state. During collision, the population flows to the closeby manifold of rotational levels, according to the collisional propensity rules for the permanent dipole term, which follow from the selection rules for both perturbations and pure rotational transitions [25, 45]:

$$\Delta J = \pm 2, \pm 4, \cdots,$$

$$\Delta\Omega = 0,$$

$$\Delta S = 0,$$

$$\boldsymbol{s} \not\leftrightarrow \boldsymbol{a},$$

$$e \not\leftrightarrow f,$$

$$g \not\leftrightarrow u.$$

According to the previous discussion, although the dipole selection rule on spin, $\Delta S = 0$, prohibits direct transition between the singlet and triplet states, the nearly degenerate singlet and triplet levels with the same rotational quantum number J can couple together by the spin-orbit interaction. When a pair of ro-vibrational levels of two electronic states is appreciably mixed, this pair of mutually perturbing levels acts as a "*gateway*" through which population flows on its way from one electronic state to the other, leading to a pathway for singlet-triplet transfer, the life time of which is usually too short to be observed.

3.6 The Mixing Character

As discussed in Section 3.4, in the presence of strong electromagnetic fields, the energy levels in atoms or molecules experience shifts in their positions due to the AT effect.

The AT effect is used to modify the mixing coefficients, and thus the amount of singlet or triplet character, of a pair of ro-vibrational states initially perturbed by the spin-orbit interaction (Figure 3.9).

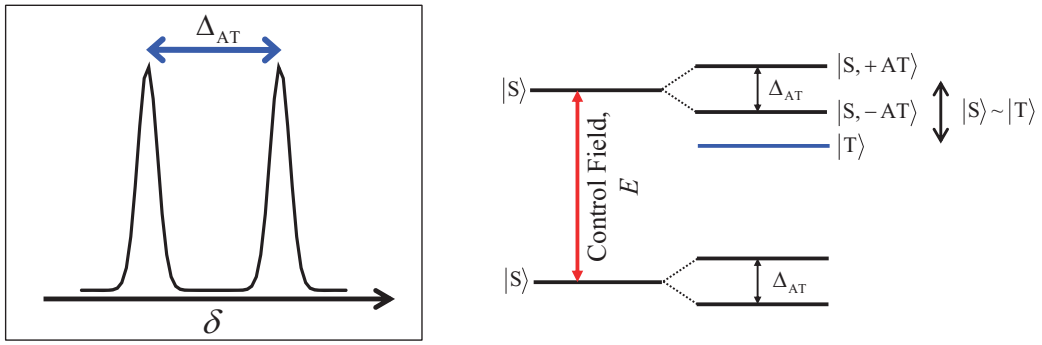

(a) (b)

Figure 3.9: The AT effect is used to manipulate the spin character of a spin-orbit coupled pair of levels (*Gateway Levels*) between the singlet and triplet electronic state manifolds. (a) The AT splitting describes the phenomenon that the transition splits into a pair of states under influence of a strong electromagnetic field. (b) The AT effect is used to control singlet-triplet character of the energy levels. The $|S\rangle \sim |T\rangle$ mixing is created by shifting AT split singlet components.

The shift due to the AT effect Δ_{AT} is propotional to Rabi frequency,

$$\begin{aligned} \Delta_{AT} &= \text{Const} \cdot \Omega, \\ \Omega &= \frac{\mu E}{\hbar}, \end{aligned}$$

with the transition dipole moment matrix element μ, and electric field

$$E_0 = \sqrt{\frac{2}{c\varepsilon_0}} \cdot \sqrt{\frac{2P_{\text{tot}}}{\pi w^2}}.$$

Based on recent theoretical studies for quantum control of the singlet-triplet mixing of two states [48–51], a target state of a desirable mixture of singlet and triplet states, which are close in energy and weakly mixed by a small perturbation, could be

created by applying a strong coupling laser on resonance between one of the mixed levels and a separate third level. And the control of the spin-orbit interaction can be realized by changing the coupling field strength.

Figure 3.10 depicts an example of how to manipulate the spin character of the spin-orbit coupled pair of levels serving as a *gateway* between the singlet and triplet electronic state manifolds [16]. Thermal population in the ground $X^1\Sigma_g^+$ state is excited to the first excited $A^1\Sigma_u^+$ state by the weak pump laser L_1. And then L_2, the weak probe laser, excites the population to the mixed pair of levels $G^1\Pi_g \sim 1^3\Sigma_g^-$, which are the *gateway* levels. The strong coupling laser L_3 couples the transition between the $G^1\Pi_g$ state and the $A^1\Sigma_u^+$ electronic state with different rotational quantum numbers J. Both singlet and triplet channel fluorescence is detected from the mixed $G^1\Pi_g \sim 1^3\Sigma_g^-$ gateway levels simultaneously. The mixing character can be manipulated by tuning the coupling laser E field amplitude.

In Figure 3.10, the singlet $|S_0\rangle$ states and the triplet $|T_0\rangle$ state are two closely spaced eigenstates coupled by the spin-orbit perturbation $\widehat{H}_{SO}$, which creates the mixed states $|S\rangle$ and $|T\rangle$, which have characteristics of both unperturbed states [20, 52, 53]. The Hamiltonian of the two-state system can be written as [44, 54],

$$\begin{pmatrix} E_{S_0} - E & H_{SO} \\ H_{SO} & E_{T_0} - E \end{pmatrix} \begin{pmatrix} \alpha \\ \beta \end{pmatrix} = 0, \tag{3.19}$$

where E_{S_0} and E_{T_0} are the eigenenergies of the pure singlet and the pure triplet state $|S_0\rangle$ and $|T_0\rangle$, respectively. α and β are the mixing coefficients for each wave vector solution. $|H_{SO}|$ is the spin-orbit perturbation matrix element, defined as

$$|H_{SO}| = |\langle S_0|\widehat{H}_{SO}|T_0\rangle|. \tag{3.20}$$

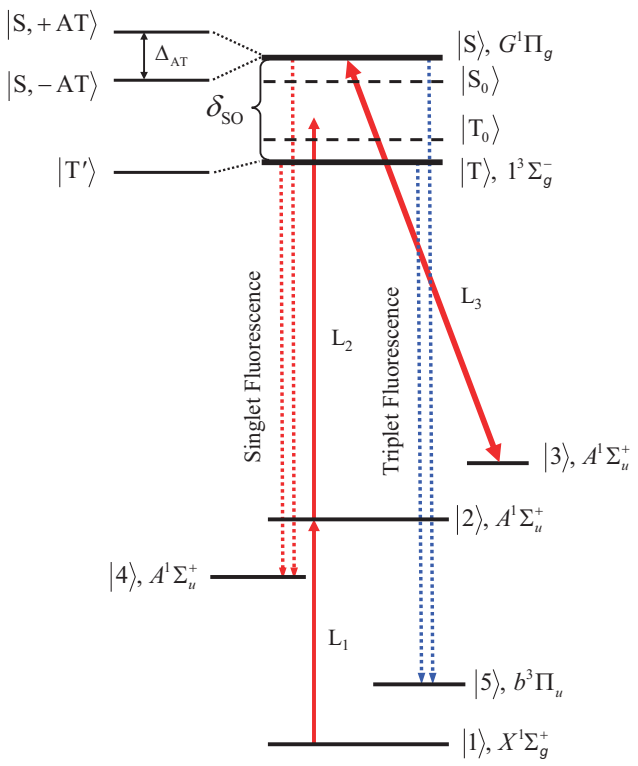

Figure 3.10: All-optical control of the spin-orbit interaction according to Reference [16]. The weak pump laser L_1 excites the population from the ground state $(|1\rangle, X^1\Sigma_g^+)$ to the first excited state $(|2\rangle, A^1\Sigma_u^+)$. Then L_2, the weak probe laser, further excites the population to the *gateway* levels $G^1\Pi_g \sim 1^3\Sigma_g^-$. The coupling field L_3 is set on resonance with the transition of $|S\rangle \leftrightarrow |3\rangle$. The fluorescence of transitions from the mixed levels $G^1\Pi_g \sim 1^3\Sigma_g^-$ to the singlet level $|4\rangle$ and the triplet level $|5\rangle$ is simultaneously observed from both singlet and triplet channels, respectively.

Thus the eigenenergies of the perturbed states are given by

$$E_{S,T} = \frac{1}{2}\left\{(E_{S_0} + E_{T_0}) \pm \left[(E_{S_0} - E_{T_0})^2 + 4|H_{SO}|^2\right]^{\frac{1}{2}}\right\}. \tag{3.21}$$

The wavefunctions of the perturbed states can be written as

$$|S\rangle = \alpha|S_0\rangle - \beta|T_0\rangle, \tag{3.22a}$$

$$|T\rangle = \alpha|T_0\rangle + \beta|S_0\rangle, \tag{3.22b}$$

with the normalization condition

$$\alpha^2 + \beta^2 = 1, \tag{3.23}$$

the mixing coefficients are given by

$$\alpha = \frac{|H_{\mathrm{SO}}|}{\sqrt{\delta^2 + |H_{\mathrm{SO}}|^2}}, \tag{3.24a}$$

$$\beta = \frac{\delta}{\sqrt{\delta^2 + |H_{\mathrm{SO}}|^2}}, \tag{3.24b}$$

where δ is the splitting between the perturbed and unperturbed states,

$$\delta = E_{\mathrm{S}} - E_{\mathrm{S}_0} = E_{\mathrm{T}_0} - E_{\mathrm{T}}.$$

Thus from Equation 3.24, $|H_{\mathrm{SO}}|$ can be determined from the amplitude ratio and the energy shift,

$$|H_{\mathrm{SO}}| = \delta\alpha/\beta. \tag{3.25}$$

The amplitude ratio α/β is related to the ratio of the emission intensities through the singlet and triplet channels from the perturbed level. For states defined by Equations 3.22

$$\left(\frac{I_{\mathrm{triplet}}}{I_{\mathrm{singlet}}}\right)_{\mathrm{S}} = \frac{\epsilon_{\mathrm{t}}}{\epsilon_{\mathrm{s}}}\frac{\tau_{\mathrm{s}}}{\tau_{\mathrm{t}}}\frac{|\beta|^2}{|\alpha|^2}, \tag{3.26a}$$

$$\left(\frac{I_{\mathrm{triplet}}}{I_{\mathrm{singlet}}}\right)_{\mathrm{T}} = \frac{\epsilon_{\mathrm{t}}}{\epsilon_{\mathrm{s}}}\frac{\tau_{\mathrm{s}}}{\tau_{\mathrm{t}}}\frac{|\alpha|^2}{|\beta|^2}, \tag{3.26b}$$

here τ_{s} and τ_{t} are the Einstein coefficients of the unperturbed singlet and triplet components, respectively, and ϵ_{s} and ϵ_{t} are the detection system efficiencies. $(I_{\mathrm{triplet}})_{\mathrm{S}}$ and $(I_{\mathrm{singlet}})_{\mathrm{S}}$ are the fluorescence intensities of the state $|\mathrm{S}\rangle$ through the triplet and singlet

channels, respectively, and $(I_{\text{triplet}})_{\text{T}}$ and $(I_{\text{singlet}})_{\text{T}}$ are the fluorescence intensities of the state $|\text{T}\rangle$ through the triplet and singlet channels, respectively. Thus the mixing coefficients can be found by measuring the intensity of the fluorescence from each of the mixed levels [54],

$$\frac{\alpha}{\beta} = \left(\frac{(I_{\text{triplet}}/I_{\text{singlet}})_{\text{T}}}{(I_{\text{triplet}}/I_{\text{singlet}})_{\text{S}}}\right)^{\frac{1}{4}} = \left(\frac{(I_{\text{triplet}})_{\text{T}}/(I_{\text{triplet}})_{\text{S}}}{(I_{\text{singlet}})_{\text{T}}/I_{\text{singlet}})_{\text{S}}}\right)^{\frac{1}{4}}. \tag{3.27}$$

Then the Hamiltonian of the system $|H_{\text{SO}}|$ can be further determined from Equation 3.25.

As shown in Figure 3.10, taking into account the energy separation between the perturbed levels $|\text{S}\rangle$ and $|\text{T}\rangle$,

$$\delta_{\text{SO}} = E_{\text{S}} - E_{\text{T}},$$

and the energy separation between the unperturbed levels $|\text{S}_0\rangle$ and $|\text{T}_0\rangle$,

$$\delta^0_{\text{SO}} = E_{\text{S}_0} - E_{\text{T}_0},$$

with the relation,

$$\delta^0_{\text{SO}} = (\alpha^2 - \beta^2)\delta_{\text{SO}},$$

according to Equations 3.25, the Hamiltonian of the spin-orbit interaction can be simplified as [44, 54]

$$H_{\text{SO}} = \hbar\alpha\beta\delta_{\text{SO}}.$$

When the coupling field is applied to the system, the Hamiltonian of the interaction of the molecule with the optical fields, H_{int}, has to be included. It has the form $-\boldsymbol{\mu}\cdot\boldsymbol{E}$, where $\boldsymbol{\mu}$ is the transition dipole moment between the levels coupled by a laser with electric field $\boldsymbol{E}$. After applying the rotating wave approximation, considering the levels that are directly coupled by optical field and the spin-orbit interaction, $|1\rangle$,

$|2\rangle$, $|3\rangle$, $|\mathrm{S}_0\rangle$, and $|\mathrm{T}_0\rangle$ in Figure 3.10, the Hamiltonian of interaction of the system with optical fields can be written as [16],

$$\begin{aligned}\frac{H_I}{\hbar} &= \alpha\beta\delta_{\mathrm{SO}}(|S_0\rangle\langle T_0| + |T_0\rangle\langle S_0|) + \frac{\Omega_1}{2}(|2\rangle\langle 1| + |1\rangle\langle 2|) + \frac{\Omega_2}{2}(|S_0\rangle\langle 2| + |2\rangle\langle S_0|) \\ &+\frac{\Omega_3}{2}(|3\rangle\langle S_0| + |S_0\rangle\langle 3|) - (\delta_1+\delta_2)|S_0\rangle\langle S_0| - (\delta_1+\delta_2+\delta^0_{\mathrm{SO}})|T_0\rangle\langle T_0| \\ &-\delta_1|2\rangle\langle 2| - (\delta_1+\delta_2-\delta_3)|3\rangle\langle 3|, \end{aligned} \tag{3.28}$$

where δ_i is the velocity-dependent detuning of the ith laser

$$\delta_i \equiv \Delta_i \pm k_i v_z,$$

with

$$\Delta_i \equiv \omega_i - \omega_{i,\mathrm{res}},$$

the detunings for molecules at rest in the lab frame. ω_i is the frequency of the ith laser, and $\omega_{i,\mathrm{res}}$ is the resonance transition frequency between the corresponding unperturbed levels. The Rabi frequency of laser i is

$$\Omega_i = \frac{\mu_i E_i}{\hbar}.$$

When the control field couples the states $|\mathrm{S}\rangle$ and $|3\rangle$, the nominally singlet peak splits into two components ($|\mathrm{S},-\mathrm{AT}\rangle$ and $|\mathrm{S},+\mathrm{AT}\rangle$ as shown in Figure 3.10) due to the AT effect, with the separation determined by the Rabi frequency of the control laser L_3. The $|\mathrm{S},-\mathrm{AT}\rangle$ component of the pair shifts closer to the nearby $|\mathrm{T}\rangle$ state and acquires more triplet character and the $|\mathrm{T}\rangle$ level shifts slightly to the modified state $|\mathrm{T}'\rangle$ and acquires more singlet character due to the spin-orbit interaction between them. Meanwhile the separation between the $|\mathrm{S},+\mathrm{AT}\rangle$ component and the $|\mathrm{T}\rangle$ state increases. Thus the singlet character of the $|\mathrm{S},+\mathrm{AT}\rangle$ component is en-

hanced due to the decreasing amount of mixing between them. The result is shown in Figure 3.11 [16].

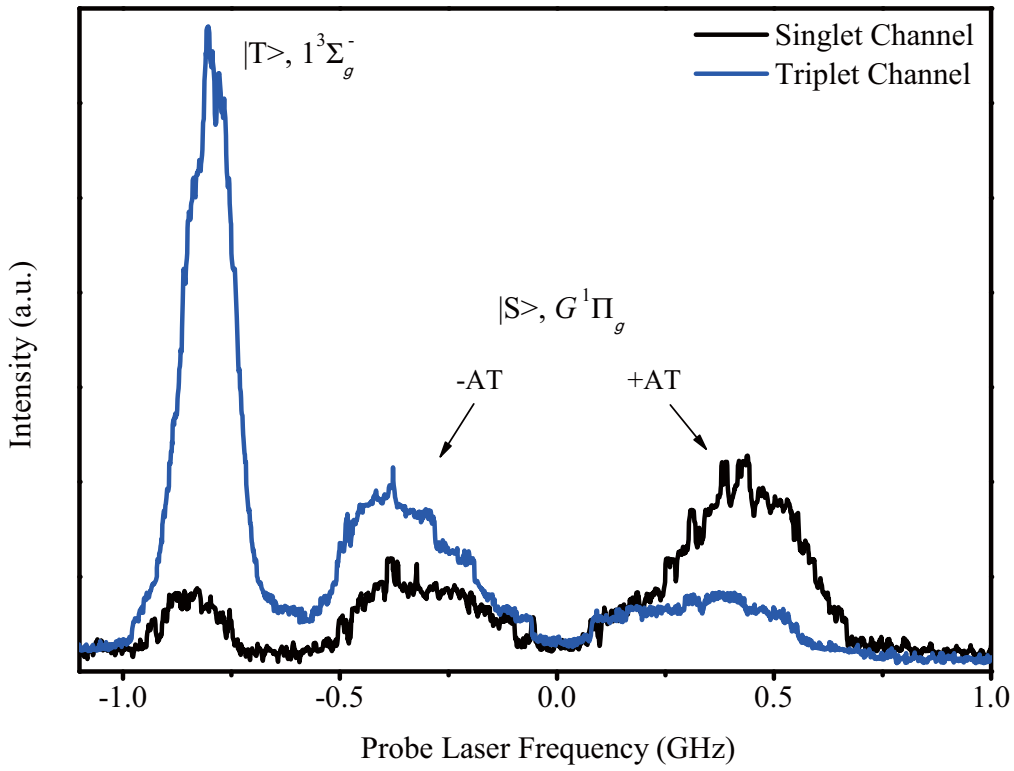

Figure 3.11: Singlet-triplet mixing according to Reference [16]. With the control laser on resonance between the $|\mathrm{S}\rangle$ state and the $|3\rangle$ state (Figure 3.10), the fluorescence from the singlet (black line) and triplet (blue line) channels are observed simultaneously. The $|\mathrm{S}, -\mathrm{AT}\rangle$ component gains more triplet character in mixing and $|\mathrm{S}, +\mathrm{AT}\rangle$ component becomes "cleaner" singlet.

In order to demonstrate that the spin-orbit interaction can be manipulated by tuning the amplitude of the control laser field, the spectra from the singlet fluorescence channel with varying power levels of the control laser is shown in Figure 3.12. By increasing the power level of the control laser, the spin-orbit interaction of $|T'\rangle$ with the $|\mathrm{S}, -\mathrm{AT}\rangle$ component increases, and the singlet-triplet mixing is enhanced. The singlet character of the predominantly triplet level $|T'\rangle$ is enhanced. And the two

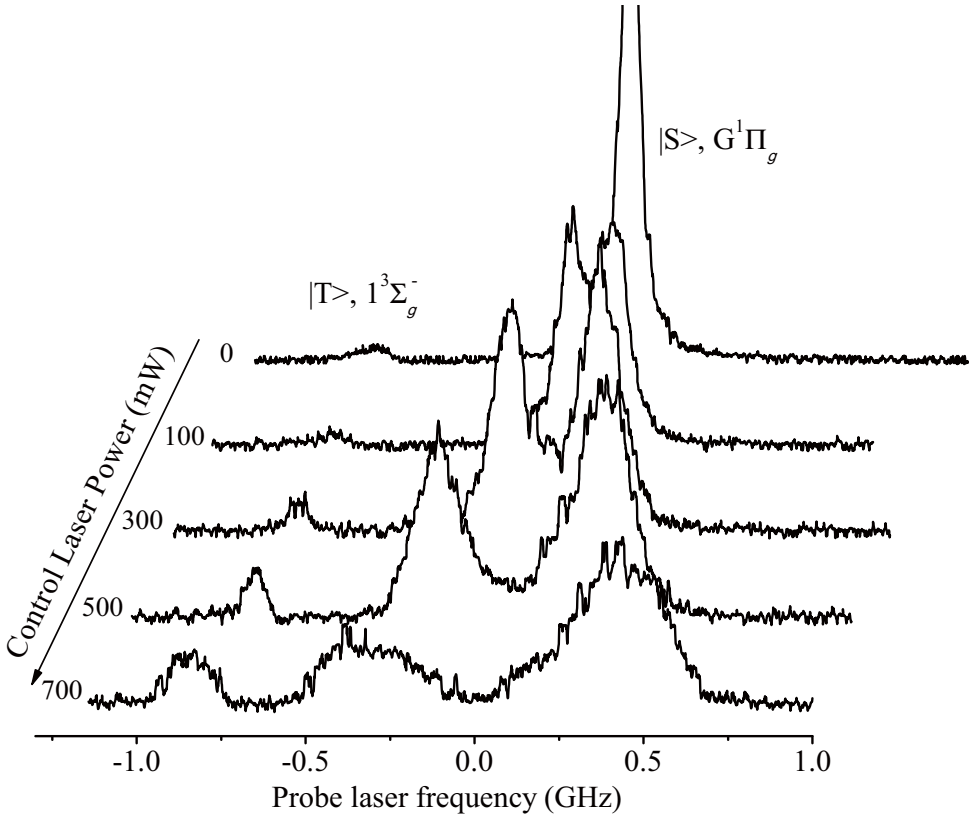

Figure 3.12: The dependence of the singlet-triplet mixing and the magnitude of the AT splitting on the control laser power according to Reference [16]. The spectra of the singlet fluorescence from the perturbed levels to the lower $A^1\Sigma_u^+$ level are recorded with different power levels of the control laser. As the control laser power increases, the leftmost peak, corresponding to the fluorescence from the level $|T'\rangle$ with primarily triplet character, gains more singlet character. Meanwhile the peak(s) on the right, corresponding to the fluorescence from the components $|\mathrm{S}, -\mathrm{AT}\rangle$ and $|\mathrm{S}, +\mathrm{AT}\rangle$ with primarily singlet character, shift apart more due to AT effect.

components $|\mathrm{S}, -\mathrm{AT}\rangle$ and $|\mathrm{S}, +\mathrm{AT}\rangle$ of the AT pair, predominantly of singlet character, become more asymmetric.

3.7 Conclusion

In this chapter, we have investigated several quantum interference effects, such as the Autler-Townes (AT) effect and electromagnetically induced transparency (EIT). The AT effect states that under the influence of a strong electromagnetic field, the transition experiences splitting into a pair of states, and the magnitude of the splitting between the two components is proportional to the strength of the coupling field.

The optical control of the collisional population flow between singlet and triplet state manifolds could be achieved by manipulating the spin character in a pair of singlet-triplet mixed *gateway* levels following the collisional propensity rules. The mixing coefficients of two states, which are perturbed by the spin-orbit interaction, can be determined by measuring the intensity of fluorescence from each of the mixed levels.

Finally, we have shown that the population flow between the singlet manifold and the triplet manifold of the perturbed states could be enhanced with the gateway opening "wider", by increasing the coupling laser power.

References

[5] K.-J. Boller, A. Imamoğlu, and S. E. Harris, Phys. Rev. Lett. **66**, 2593 (1991).

[6] J. E. Field, K. H. Hahn, and S. E. Harris, Phys. Rev. Lett. **67**, 3062 (1991).

[7] S. H. Autler, and C. H. Townes, Phys. Rev. **100**, 703 (1955).

[11] J. Qi, G. Lazarov, X. Wang, L. Li, L. M. Narducci, A. M. Lyyra, and F. C. Spano, Phys. Rev. Lett. **83**, 288 (1999).

[16] E. H. Ahmed, S. Ingram, T. Kirova, O. Salihoglu, J. Huennekens, J. Qi, Y. Guan, and A. M. Lyyra, Phys. Rev. Lett. **107**, 163601 (2011).

[20] G. Herzberg, *Molecular spectra and molecular structure I, Spectra of diatomic molecules* (Krieger Publishing Company, Malabar, Florida, 1989).

[22] H. Lefebvre-Brion, and R. W. Field, *Perturbations in the spectra of diatomic molecules* (Academic Press, Orlando, 1986).

[25] H. Lefebvre-Brion, and R. W. Field, *The spectra and dynamics of diatomic molecules* (Elsevier, Amsterdam, 2004).

[29] L. Li, and R. W. Field, J. Phys. Chem. **87**, 3020 (1983).

[30] L. Li, and R. W. Field, *Molecular dynamics and spectroscopy of stimulated emission pumping*, edited by H. L. Dai, and R.W.Field, (World Scientific, Singapore, 1995) Chap. 7, p. 251.

[31] L. Li, and A. M. Lyyra, Spectrochimi. Acta, Part A **55**, 2147 (1999).

[32] L. Morgus, P. Burns, R. D. Miles, A. D. Wilkins, U. Ogba, A. P. Hickman, and J. Huennekens, J. Chem. Phys. **122**, 144313 (2005).

[33] P. Burns, L. Sibbach-Morgus, A. D. Wilkins, F. Halpern, L. Clarke, R. D. Miles, L. Li, A. P. Hickman, and J. Huennekens, J. Chem. Phys. **119**, 4743 (2003).

[34] S. Frank L. Pedrotti, L. M. Pedrotti, and L. S. Pedrotti, *Introduction to optics*, 3rd ed. (Pearson Education, Inc., New Jersey, 2007) Chap. 26, p. 567.

[35] D. R. Skinner, and R. E. Whitcher, J. Phys. E **5**, 237 (1972).

[36] J. Qi, Ph.D. Thesis, Temple University (2000).

[37] J. Qi, F. C. Spano, T. Kirova, A. Lazoudis, J. Magnes, L. Li, L. M. Narducci, R. W. Field, and A. M. Lyyra, Phys. Rev. Lett. **88**, 173003 (2002).

[38] F. C. Spano, J. Chem. Phys. **114**, 276 (2001).

[39] D. L. Cooper, J. M. Hutson, and T. Uzer, Chem. Phys. Lett. **86**, 472 (1982).

[40] S. Ingram, Ph.D. Thesis, Temple University (2010).

[41] L. Veseth, Theo. Chim. Acta **18**, 368 (1970).

[42] R. N. Zare, *Angular momentum* (Wiley-Interscience, New York, 1986).

[43] M. Blume, A. J. Freeman, and R. E. Watson, Phys. Rev. **134**, A320 (1964).

[44] X. Xie, and R. W. Field, Chem. Phys. **99**, 337 (1985).

[45] L. Li, Q. Zhu, A. M. Lyyra, T. Whang, W. C. Stwalley, R. W. Field, and M. H. Alexander, J. Chem. Phys. **97**, 8835 (1992).

[46] L. Li, S. Antonova, A. Yiannopoulou, K. Urbanski, and A. M. Lyyra, J. Chem. Phys. **105**, 9859 (1996).

[47] A. M. Lyyra, H. Wang, T.-J. Whang, W. C. Stwalley, and L. Li, Phys. Rev. Lett. **66**, 2724 (1991).

[48] T. Kirova, and F. C. Spano, Phys. Rev. A **71**, 063816 (2005).

[49] M. V. Korolkov, and J. Manz, J. Chem. Phys. **120**, 11522 (2004).

[50] J. González-Vázquez, I. R. Sola, J. Santamaria, and V. S. Malinovsky, Chem. Phys. Lett. **431**, 231 (2006).

[51] J. González-Vázquez, I. R. Sola, J. Santamaria, and V. S. Malinovsky, J. Chem. Phys. **125**, 124315 (2006).

[52] J. Huennekens, A. Loza, M. Masters, and K. M. Sando, J. Chem. Phys. **88**, 6013 (1988).

[53] M. Masters, J. Huennekens, W. Luh, L. Li, A. M. Lyyra, K. Sando, V. Zafiropulos, and W. C. Stwalley, J. Chem. Phys. **92**, 5801 (1990).

[54] H. Sun, and J. Huennekens, J. Chem. Phys. **97**, 4714 (1992).

CHAPTER 4

OPTICAL CONTROL OF COLLISIONAL POPULATION TRANSFER BETWEEN MOLECULAR ELECTRONIC STATES OF DIFFERENT SPIN MULTIPLICITY

4.1 Introduction

For diatomic alkali-metal molecules, the adiabatic model (Figure 4.1) can be described as two-dimentional electronic potential energy curves, and the intersections become avoided crossings of the intersecting diabatic potentials due to the perturbation [22]. However, this model breaks down when relativistic effects such as the spin-orbit interaction, which is the coupling between the electron spin and its orbital angular

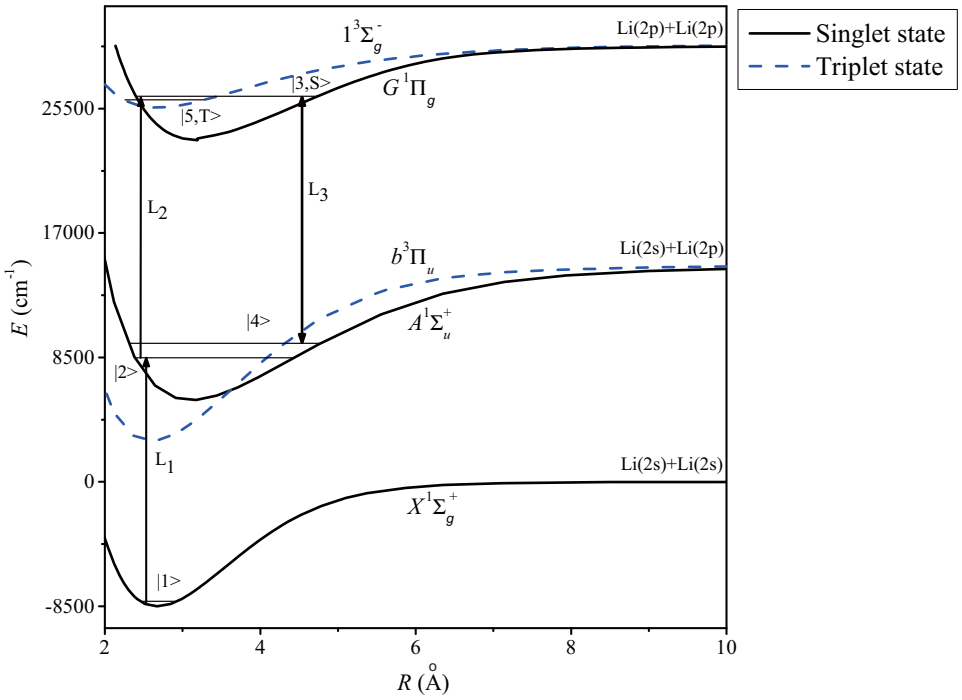

Figure 4.1: The adiabatic model of potential energy curves for the electronic states $X^1\Sigma_g^+$, $A^1\Sigma_u^+$, $b^3\Pi_u$, $G^1\Pi_g$, and $1^3\Sigma_g^-$ of $^7Li_2$ as a function of internuclear distance R [55–59]. The $A^1\Sigma_u^+$ and $b^3\Pi_u$ states have the same dissociation limit 2s+2p, and the $G^1\Pi_g$ and $1^3\Sigma_g^-$ states have the same dissociation limit 2p+2p. The mixing of singlet and triplet states $A^1\Sigma_u^+ \sim b^3\Pi_u$ and $G^1\Pi_g \sim 1^3\Sigma_g^-$ occur between two ro-vibrational levels with the same rotational quantum number J by the spin-orbit interaction.

momentum, are taken into account, as previously discussed in Section 3.5. Although the dipole selection rule on spin, $\Delta S = 0$, prohibits direct excitation between states of different spins (singlet $\not\Leftrightarrow$ triplet), singlet and triplet energy levels with the same rotational quantum number J can couple together by the spin-orbit interaction creating levels of mixed singlet-triplet character. These mixed spin-multiplicity character levels form a "*gateway*" [25, 45, 46, 60] for transferring population between singlet and triplet manifolds by collisional pathways through levels of mixed singlet and triplet character.

In the recent experiment, Ahmed *et al.* [16, 40] have demonstrated that the singlet and triplet character of a pair of levels coupled by the spin-orbit interaction serving as

a *gateway* can be manipulated by using the Autler-Townes (AC Stark) effect [7]. In this work [17], we extend the experiment for optical control of collisional population transfer between singlet and triplet states of the $^7Li_2$ dimer.

4.2 Experimental Apparatus

The experimental set-up is illustrated in Figure 4.2.

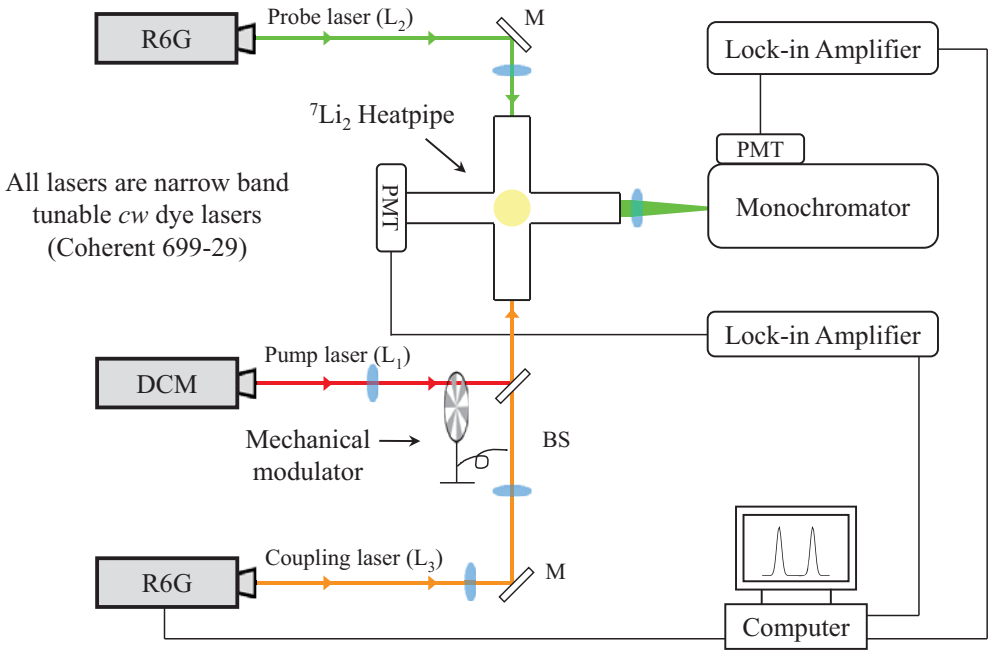

Figure 4.2: The experimental set-up for optical control of collisional population transfer between molecular electronic states of different spin multiplicity. The pump (L_1) and probe (L_2) lasers are counterpropagating, while the coupling laser (L_3) copropagates with L_1. A monochromator is used for the singlet channel and a PMT with an interference bandpass filter (Thorlabs, center wavelength 441.6 nm and bandwidth 10 nm) is used for the triplet channel.

The Lithium metal is loaded into a five-arm, stainless steel heatpipe oven. Two of the side arms are heated by 280 Ohm ceramic heaters (Lindberg), while the top arm is wrapped by a cable heater (ARI, BXX-093B38-4T) for uniformly heating the oven. All three heaters as well as the reservoir at the bottom center of the heatpipe are

wrapped with extra external insulation. The oven temperature is controlled around 850 K by the voltage applied to the heaters, and can be calculated from the *Doppler* profile of one laser transition, discussed in Section 3.2. The heatpipe is vacuum sealed by holding the window on the flange with o-ring at the end of each arm. The arms of the heatpipe are water-cooled to avoid condensation of the metal vapor on the windows and flanges. A layer of stainless steel mesh is placed inside each arm to allow the liquid lithium to circulate smoothly inside the heatpipe. The difference between the hot and cold regions of the heatpipe can be as large as 500 K.

The $^7Li_2$ dimers are produced at the reservoir of the heatpipe under the $\sim$2.3 cm long interaction region where the laser beams are focused and from which the fluorescence corresponding to specific rovibronic transitions is emitted in a direction perpendicular to the laser propagation axis. Most of the vapor produced in the heatpipe is atomic Lithium, with about 5% of the atoms forming molecular Lithium.

Argon gas is used not only as a buffer gas to prevent hot metal vapor from reaching the heatpipe oven windows, but also to introduce collisions with $^7Li_2$ molecules causing population transfer in this experiment. The vapor pressure dependence of the collision rate will be discussed later in Section 4.4. Thus in order to look at the collisions explicitly, the argon gas is loaded into the heatpipe oven at 2 Torr pressure (measured at room temperature).

The pump (L_1), probe (L_2), and coupling (L_3) lasers are all Coherent 699-29 *cw* dye lasers. The pump laser (L_1) is operated with dicyanomethylene (DCM) dye, and both the probe (L_2) and coupling (L_3) lasers are operated with Rhodamine 590 (R6G) dye. The pump (L_1) and probe (L_2) lasers are counterpropagating, while the coupling laser (L_3) copropagates relative to L_1 in the heatpipe. A mechanical modulator is used on the pump laser to improve the signal to noise by phase sensitive detection with lock-in amplifiers. A neutral density filter is used to attenuate each laser beam to the desired power, which is measured by a Coherent Lasermate D power meter, with

an accuracy of ±1% of the reading. The desired spot size, or beam waist w at the interaction region of heatpipe is achieved by using one lens or combining two lenses in the path of each laser beam, and is measured using the razor blade technique [35], as described in Section 3.3. The parameters are listed in Table 4.1.

Table 4.1: List of parameters of all three lasers used in the transition of $G^1\Pi_g \sim 1^3\Sigma_g^- - A^1\Sigma_u^+ - X^1\Sigma_g^+$.

Parameter	Value		
Temperature (K)	$T = 850$		
Pressure (mTorr)	Ar(293 K)=2000		
Power (mW)	$P_1 = 10$	$P_2 = 50$	$P_3 = 0 \sim 760$
Beam waist (μm)	$w_1 = 90$	$w_2 = 110$	$w_3 = 225$
Wavenumber (cm^{-1})	$k_1 = 15726.10$ (15684.54)	$k_2 = 18111.37$ (18103.19)	$k_3 = 17026.87$

Two fluorescence detection channels are used to monitor triplet and singlet fluorescence simultaneously (see Figure 4.3). The total triplet fluorescence is collected by a Hamamatsu R928 photomultiplier tube (PMT) mounted on the top arm of the heatpipe with an interference bandpass filter (Thorlabs, center wavelength 441.6 nm and bandwidth 10 nm) in order to separate the desired fluorescence from the background. Meanwhile the singlet channel fluorescence signal is detected using a SPEX 1404 double grating monochromator with bandwidth of ∼0.1 nm, equipped with a Hamamatsu R928 photomultiplier tube (PMT). Both signals from the photomultiplier tubes are amplified by lock-in amplifiers (SR 850).

4.3 Excitation Scheme

Figure 4.3 illustrates the excitation scheme of this experiment. The excitation process can be separated into two parts. In part "A", $^7Li_2$ molecules are first excited from a thermally populated ro-vibrational level of the ground singlet $X^1\Sigma_g^+$ electronic state

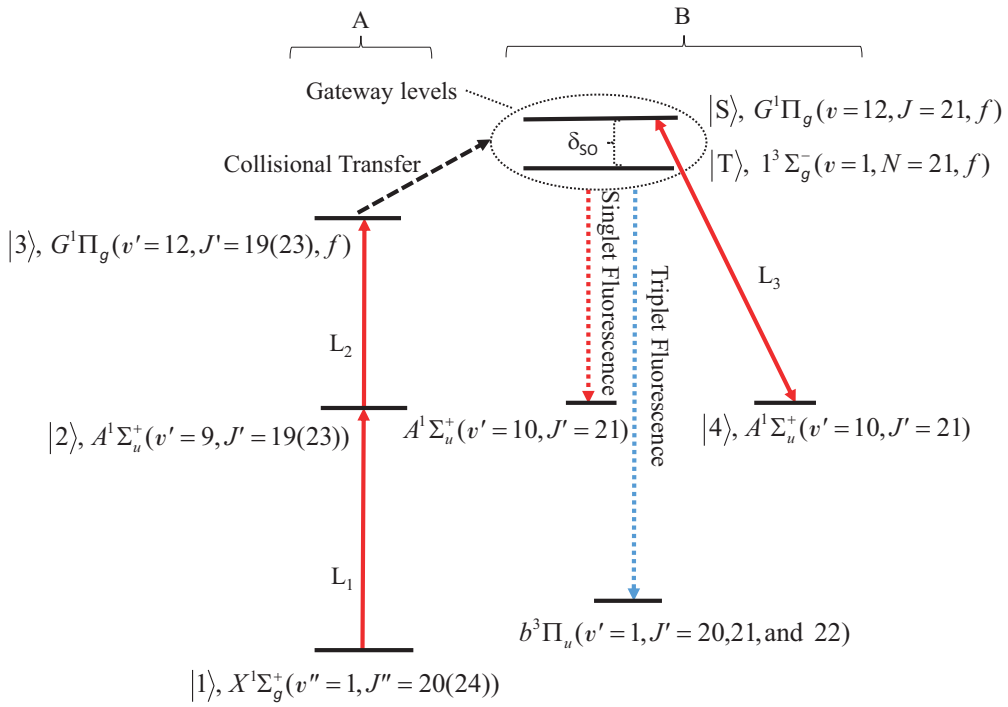

Figure 4.3: The excitation scheme for optical control of collisional population transfer between molecular electronic states of different spin multiplicity according to Reference [17]. In part A, $^7Li_2$ molecules from the ground singlet $X^1\Sigma_g^+$ state (labeled as $|1\rangle$) are excited by the pump laser L_1 to the intermediate singlet $A^1\Sigma_u^+$ state (labeled as $|2\rangle$). The probe laser L_2 then further excites the population to the singlet $G^1\Pi_g$ state (labeled as $|3\rangle$). In part B, collisions with argon gas transfer the population to the *gateway* levels $|S\rangle \sim |T\rangle$ with collisional propensity rules $\Delta J = \pm 2, \pm 4, \cdots$, and f parity only. The coupling laser L_3 couples the transition between the levels $|S\rangle$ and $|4\rangle$. The singlet and triplet fluorescence is detected simultaneously, from the *gateway* levels to $A^1\Sigma_u^+$ and $b^3\Pi_u$ states, respectively.

to a ro-vibrational level of the intermediate singlet $A^1\Sigma_u^+$ state by the pump laser (L_1). Then the probe laser (L_2) further excites the population to a ro-vibrational level of the singlet $G^1\Pi_g$ state. In part "B", the population transfers to the *gateway* levels $G^1\Pi_g(v = 12, J = 21, f) \sim 1^3\Sigma_g^-(v = 1, N = 21, f)$ ($|S\rangle \sim |T\rangle$), during collisions of the excited $^7Li_2$ molecules with argon gas, from rotational levels of the $G^1\Pi_g$ state, according to collisional propensity rules [25, 60],

$$\Delta J = \pm 2, \pm 4, \cdots ,$$

$$\Delta\Omega = 0,$$

$$\Delta S = 0,$$

$$\boldsymbol{s} \not\leftrightarrow \boldsymbol{a},$$

$$e \not\leftrightarrow f,$$

$$g \not\leftrightarrow u.$$

As described in Section 3.6, the spin character of the components of the *gateway* levels $|\mathrm{S}\rangle \sim |\mathrm{T}\rangle$ can be manipulated by using the Autler-Townes (AT) effect of the coupling laser L_3 which couples the transition between the $G^1\Pi_g$ state and the $A^1\Sigma_u^+$ electronic state. Due to the AT effect, one of the interacting levels shifts closer (stronger coupling) to the gateway partner level acquiring more triplet character, and the other shifts further away (weaker coupling) becoming a more pure singlet state. By controlling the power and detuning from resonance of the coupling field, the optical control of the collisional transfer between the pure singlet level $|3\rangle$ and the pure triplet $b^3\Pi_u$ state manifold is achieved. The resonance frequencies of the lasers are given in Table 4.1 in wavenumber ($k = \nu/c$) in units of cm^{-1}.

Considering collisions between the argon gas and the excited $^7\mathrm{Li}_2$ molecules, the reactions in the experiment can be described by three consecutive steps:

$$\mathrm{Li}_2(|1\rangle) + h\nu_1 + h\nu_2 \rightarrow \mathrm{Li}_2^*(|3\rangle), \tag{4.1a}$$

$$\mathrm{Li}_2^*(|3\rangle) + \mathrm{Ar} \rightarrow \mathrm{Li}_2^*(|\mathrm{S}\rangle \sim |\mathrm{T}\rangle) + \mathrm{Ar}, \tag{4.1b}$$

$$\mathrm{Li}_2^*(|\mathrm{S}\rangle \sim |\mathrm{T}\rangle) \rightarrow \mathrm{Li}_2(b^3\Pi_u) + h\nu, \tag{4.1c}$$

In the first step, described as Equation 4.1a, Li_2 molecules in the ro-vibrational $X^1\Sigma_g^+(v'' = 1, J'' = 20)$ or $X^1\Sigma_g^+(v'' = 1, J'' = 24)$ ground state (level $|1\rangle$) are excited by two photons through the intermediate $A^1\Sigma_u^+(v' = 9, J' = 19)$ or $A^1\Sigma_u^+(v' =$

$9, J' = 23$) state (level $|2\rangle$) to populate the pure singlet excited state level $\mathrm{Li}_2^*(|3\rangle)$, which is either $G^1\Pi_g(v = 12, J = 19, f)$ or $G^1\Pi_g(v = 12, J = 23, f)$ state (level $|3\rangle$). In the second step, described as Equation 4.1b, the Li_2^* molecules experience collisions with argon gas, and the population transfers to the gateway levels $G^1\Pi_g(v = 12, J = 21, f) \sim 1^3\Sigma_g^-(v = 1, N = 21, f)(|\mathrm{S}\rangle \sim |\mathrm{T}\rangle)$. In the last step, described as Equation 4.1c, some fraction of the Li_2^* molecules in the gateway levels $|\mathrm{S}\rangle \sim |\mathrm{T}\rangle$ decay via spontaneous emission to the lower pure triplet $b^3\Pi_u$ state. Through this collisional mechanism, the natural spin-orbit mixing in the $|\mathrm{S}\rangle \sim |\mathrm{T}\rangle$ gateway levels allows molecules in the excited pure singlet level $|3\rangle$ to decay to pure triplet levels of the lower $b^3\Pi_u$ electronic state, which is nominally forbidden by the dipole selection rule $\Delta S = 0$.

In order to model theoretically the experimental results and to confirm the nature of the observed fluorescence line shapes, the theoretical framework [48] and the standard density matrix formalism [61, 62] are introduced. The equation of motion of the system is

$$\frac{\mathrm{d}\rho}{\mathrm{d}t} = -\frac{i}{\hbar}[H, \rho] + \Gamma\rho, \tag{4.2}$$

where ρ is the density matrix, and Γ is the relaxation matrix which accounts for physical processes such as spontaneous decay of levels, collisions, etc. The Hamiltonian of interaction of the system with optical fields is similar as Equation 3.28 [16]. By taking the levels that are directly coupled by the optical fields and the spin-orbit interaction (levels $|1\rangle, |2\rangle, |3\rangle, |\mathrm{S}_0\rangle, |\mathrm{T}_0\rangle$, and $|4\rangle$ in Figure 4.3) into account, the Hamiltonian of the system can be written as summation of two components

$$H = H^{\mathrm{A}} + H^{\mathrm{B}},$$

where H^{A} describes the subsystem formed by the states $|1\rangle, |2\rangle$, and $|3\rangle$, and H^{B} describes the subsystem formed by the states $|\mathrm{S}_0\rangle, |\mathrm{T}_0\rangle$, and $|4\rangle$. The two components

of H in the interaction picture incorporate the rotating wave approximation [62] and are expressed in the basis set of the unperturbed levels,

$$\begin{aligned} H_I^{\mathrm{A}} &= -\hbar\Delta_1|2\rangle\langle 2| - \hbar(\Delta_1+\Delta_2)|3\rangle\langle 3| \\ &\quad +\frac{\hbar}{2}\Omega_1(|2\rangle\langle 1| + |1\rangle\langle 2|) + \frac{\hbar}{2}\Omega_2(|3\rangle\langle 2| + |2\rangle\langle 3|), \qquad (4.3a) \\ H_I^{\mathrm{B}} &= -\hbar\Delta_3|4\rangle\langle 4| + \frac{\hbar}{2}\Omega_3(|4\rangle\langle \mathrm{S}_0| + |\mathrm{S}_0\rangle\langle 4|) \\ &\quad +\hbar\alpha\beta\delta_{\mathrm{SO}}(|\mathrm{S}_0\rangle\langle \mathrm{T}_0| + |\mathrm{T}_0\rangle\langle \mathrm{S}_0|), \qquad (4.3b) \end{aligned}$$

where

$$\Delta_i \equiv \omega_i - \omega_{\mathrm{res}}$$

are the detunings for molecules at rest in the lab frame, where ω_i is the frequency of the ith laser and ω_{res} is the resonance transition frequency between the corresponding unperturbed levels. The Rabi frequency Ω_i of the laser i is,

$$\Omega_i = \frac{\mu_i E_i}{\hbar},$$

where μ_i is the dipole matrix element of the corresponding transition. δ_{SO} is the energy separation between the perturbed levels $|\mathrm{S}\rangle$ and $|\mathrm{T}\rangle$. As described in Section 3.6, the mixed spin-orbit coupled states can be written as

$$|\mathrm{S}\rangle = \alpha|\mathrm{S}_0\rangle - \beta|\mathrm{T}_0\rangle,$$

$$|\mathrm{T}\rangle = \alpha|\mathrm{T}_0\rangle + \beta|\mathrm{S}_0\rangle,$$

with the normalization condition

$$\alpha^2 + \beta^2 = 1.$$

The singlet $|S_0\rangle$ states and the triplet $|T_0\rangle$ state are two closely spaced eigenstates coupled by the spin-orbit interaction, with the energy separation δ^0_{SO} proportional to δ_{SO},

$$\delta^0_{SO} = (\alpha^2 - \beta^2)\delta_{SO}.$$

4.4 Pressure Dependence of the Collision Rate

In order to find out how the vapor pressure controls collisional transfer rate, we observe the triplet fluorescence signal at different pressures of the argon gas (measured at room temperature), as shown in Figure 4.4.

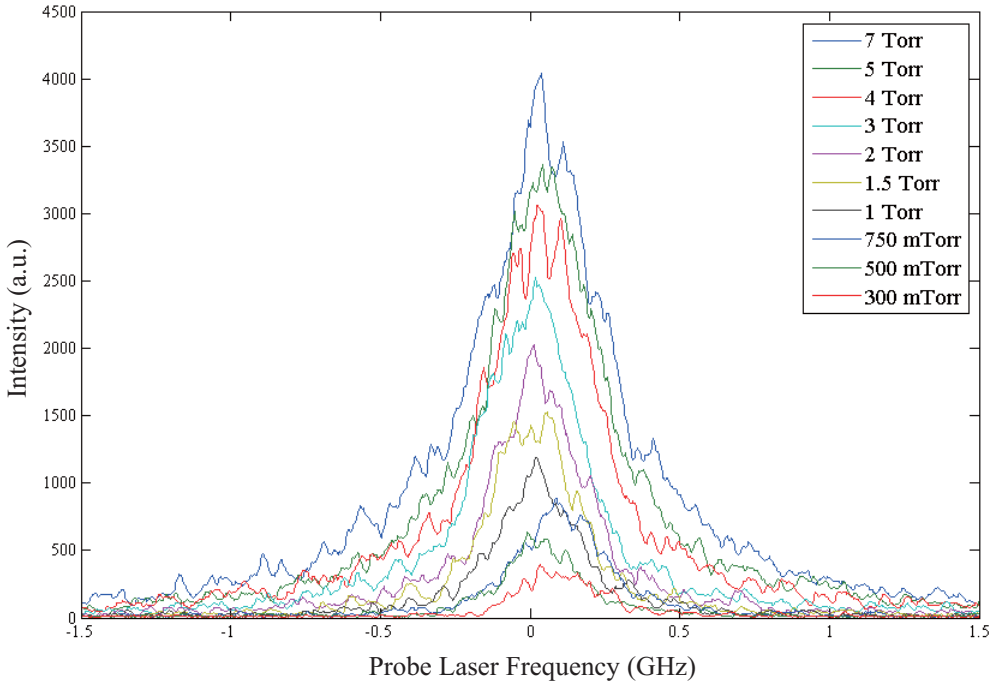

Figure 4.4: Argon gas pressure dependence of the triplet fluorescence from the gateway levels $1^3\Sigma_g^-(v = 1, N = 21, f) \sim G^1\Pi_g(v = 12, J = 21, f)$ to the $b^3\Pi_u(v' = 1, J' = 20, 21, 22)$ levels, as a function of the probe laser detuning from resonance.

The Stern-Vollmer plot [63], given in Figure 4.5, shows the dependence of triplet fluorescence signal intensity on the argon gas vapor pressure. The dotted line corre-

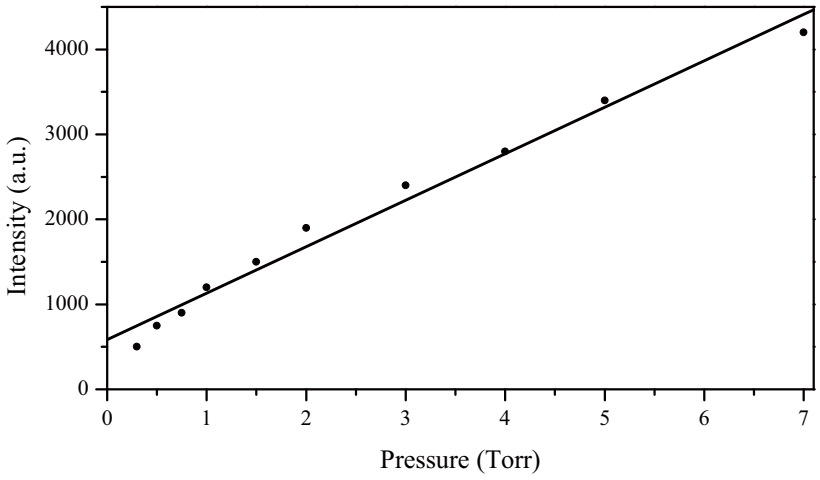

Figure 4.5: Stern-Vollmer plot showing the dependence of the triplet fluorescence signal intensity from the gateway levels $1^3\Sigma_g^-(v = 1, N = 21, f) \sim G^1\Pi_g(v = 12, J = 21, f)$ of the optically excited $^7Li_2$ molecules on the vapor pressure of argon atoms.

sponds to our experimental values of the intensity when the probe laser is on resonance for each vapor pressure, while the solid line is the linear fit of the experimental values. When the pressure drops to zero, the collisional transfer rate should fall to the value corresponding to collisional transfer due to lithium atom collisions.

We load the heatpipe oven with argon gas at 2 Torr pressure for the experiment of optical control of collisional transfer.

4.5 Experimental Result

Figure 4.6 illustrates the collisional transfer rate as a function of the probe laser detuning from resonance (a), as well as a function of the detuning of the control laser (b). In Figure 4.6(a), when only the weak pump and the probe lasers are present, due to the spin-orbit interaction between the $|S\rangle$ and $|T\rangle$ levels, a fraction of the $^7Li_2$ molecules excited to level $|3\rangle$ naturally decay through the *gateway* levels $|S\rangle \sim |T\rangle$ to the pure triplet $b^3\Pi_u$ state (black line). When the control laser (L_3) is on resonance,

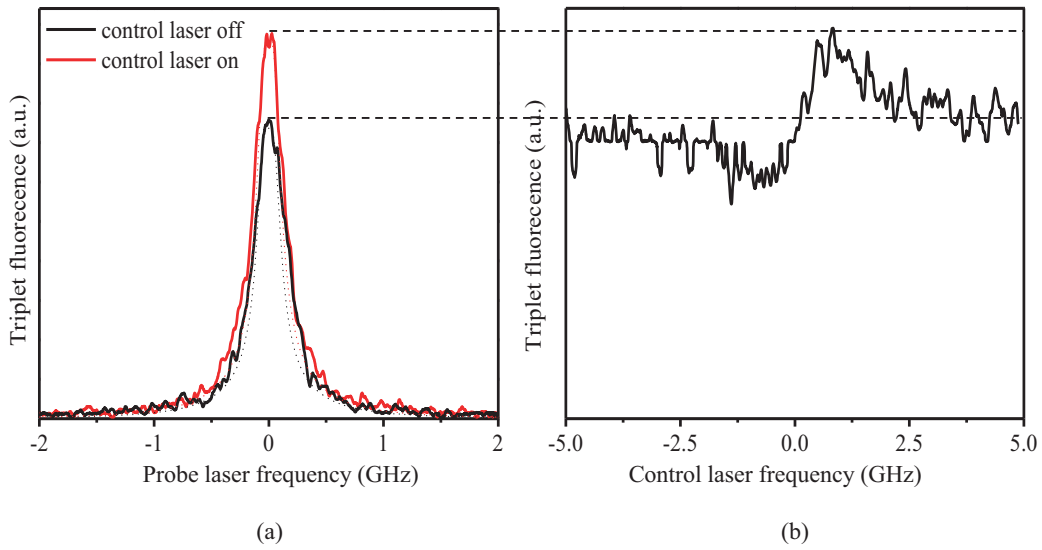

Figure 4.6: Triplet fluorescence detected from the gateway levels $1^3\Sigma_g^-(v = 1, N = 21, f) \sim G^1\Pi_g(v = 12, J = 21, f)$ to the $b^3\Pi_u(v' = 1, J' = 20, 21, 22)$ levels according to Reference [17]. (a) Probe laser (L_2) scan with (red line) and without (black line) the control laser (L_3) fixed on resonance, (b) control laser (L_3) scan while the probe laser (L_2) is fixed on resonance. The power of the control laser (L_3) is 760mW in (a) and (b).

enhancement of the collisional population transfer between the singlet level $|3\rangle$ and the triplet $b^3\Pi_u$ levels is observed (red line). The increase in the transfer rate is a result of the enhanced mixing between the singlet and the triplet states caused by the Autler-Townes effect of the control laser. In Figure 4.6(b), the peak position corresponds to the frequency of the coupling laser on resonance. There is a decrease of the transfer rate at lower frequency which is caused by the nonresonant AC Stark effect. The singlet component of the AT split pair shifts slightly in position and thus the mixing character decreases.

The suppression (lower frequency than resonance) and enhancement (on resonance) rates in the transition from the *gateway* levels $|S\rangle \sim |T\rangle$ to $b^3\Pi_u$ levels are approximately 11% and 20%, respectively, estimated from the relative change in the intensity of the triplet fluorescence observed in Figure 4.6(b). Nevertheless, the overall collisional singlet to triplet transfer rate is a constant, since the total molecular

population in the relevant levels is unaffected by the control laser and the change of the rate is relatively similar.

In order to observe the control laser power dependence of the collisional transfer rate, we recorded the triplet fluorescence intensity with varying power (Rabi frequency) of the control laser, as shown in Figure 4.7. By increasing the control laser power level, the collisional transfer rate increases, caused by the enhancement of the spin-orbit interaction of the *gateway* levels $|S\rangle \sim |T\rangle$.

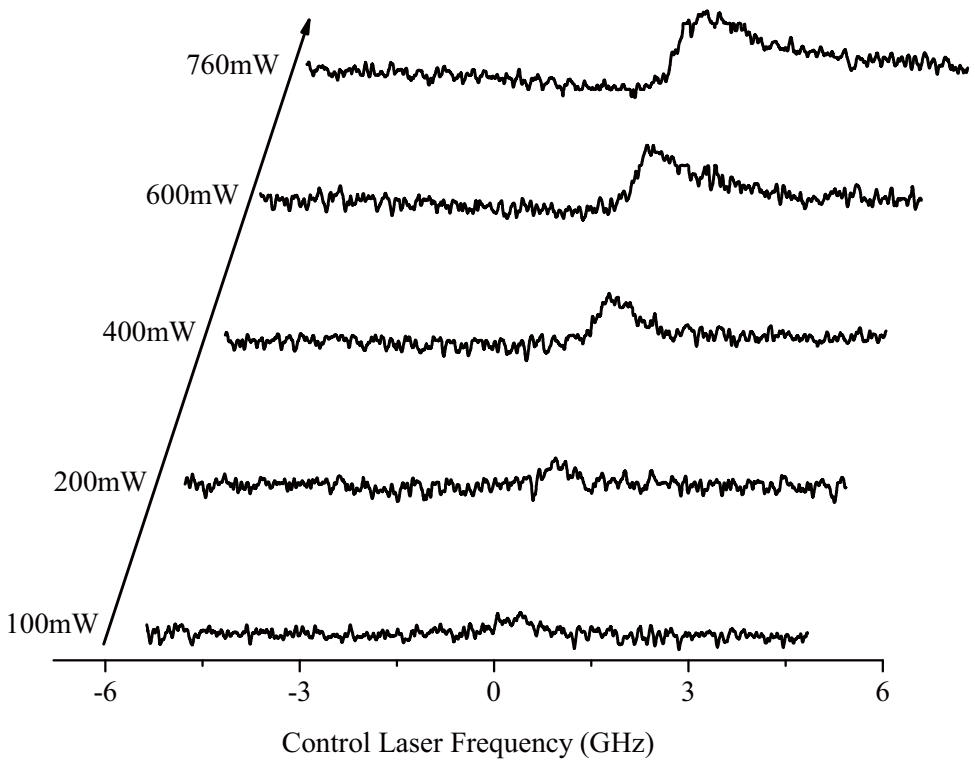

Figure 4.7: The control laser power dependence of the collisional transfer rate according to Reference [17]. The triplet fluorescence detected from the gateway levels $1^3\Sigma_g^-(v=1, N=21, f) \sim G^1\Pi_g(v=12, J=21, f)$ to the $b^3\Pi_u(v'=1, J'=20, 21, 22)$ levels are recorded with different power levels of the control laser. With the pump and probe lasers kept on resonance, the control laser is scanned over the $1^3\Sigma_g^-(v=1, N=21, f) \sim G^1\Pi_g(v=12, J=21, f) \leftrightarrow A^1\Sigma_u^+(v'=14, J'=21)$ resonance (see Figure 4.3).

In Figure 4.8 both the triplet and the singlet fluorescence from the *gateway* levels $1^3\Sigma_g^-(v=1, N=21, f) \sim G^1\Pi_g(v=12, J=21, f)$ is recorded simultaneously, in

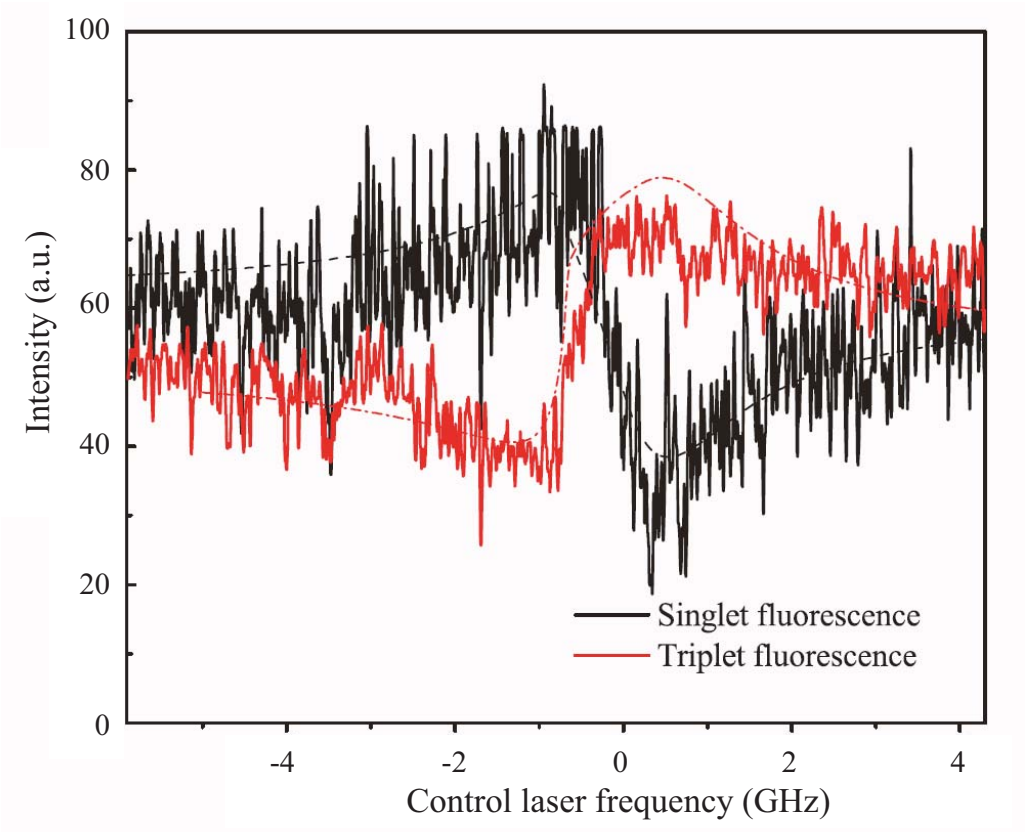

Figure 4.8: The singlet and triplet fluorescence observed simultaneously according to Reference [17]. The fluorescence signals are from the *gateway* levels $1^3\Sigma_g^-(v=1, N=21, f) \sim G^1\Pi_g(v=12, J=21, f)$ to the singlet state $A^1\Sigma_u^+$ (black line) and the triplet $b^3\Pi_u$ levels (red line), respectively, as a function of the coupling laser detuning. The dashed lines are the simulations.

order to test the conservation of the molecular population. When the transfer from the *gateway* levels $1^3\Sigma_g^-(v=1, N=21, f) \sim G^1\Pi_g(v=12, J=21, f)$ to the triplet manifold $b^3\Pi_u$ is enhanced (red line), the decay from the *gateway* levels $1^3\Sigma_g^-(v=1, N=21, f) \sim G^1\Pi_g(v=12, J=21, f)$ to the singlet manifold $A^1\Sigma_u^+$ is suppressed and vice versa (black line). The singlet and triplet fluorescence signals from the *gateway* levels are complementary. The lower signal to noise ratio in Figure 4.8 compared to Figures 4.6(b) and 4.7 is due to the low laser power for the lasers L_1 and L_2 and the SPEX 1404 monochromator (50-μm entrance and exit slits) used as a very narrow bandpass filter for the monitoring of the singlet fluorescence.

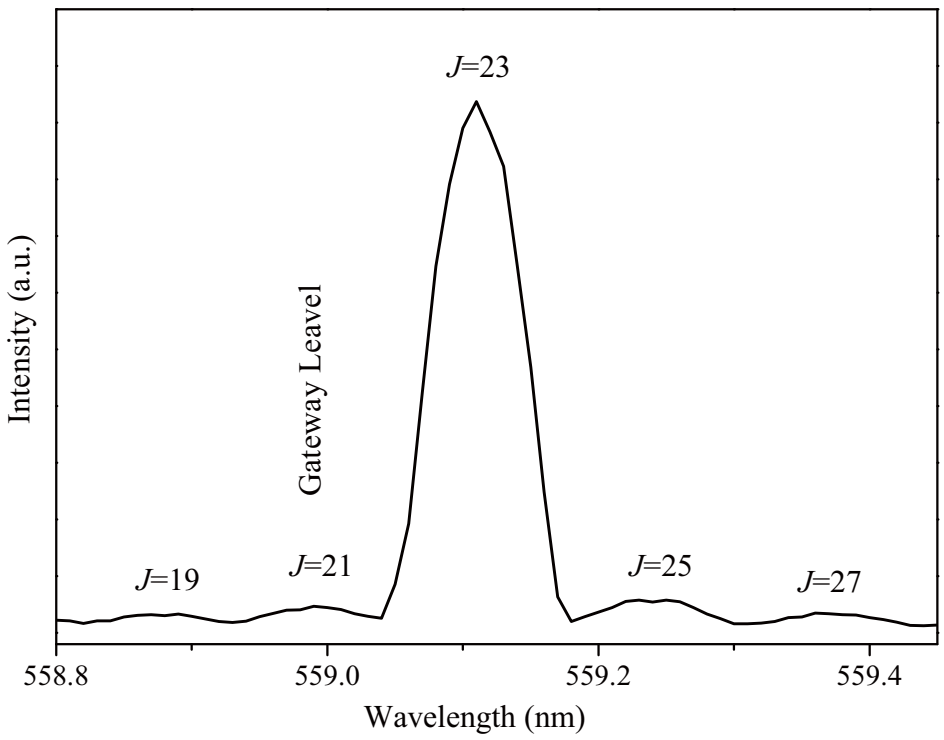

Figure 4.9: Resolved fluorescence of the direct excitation $X^1\Sigma_g^+(v''=1, J''=24) \rightarrow A^1\Sigma_u^+(v'=9, J'=23) \rightarrow G^1\Pi_g(v=12, J=23, f)$ (part "A" in Figure 4.3) and the $\Delta J = \pm 2, \pm 4$ collisional satellite components according to Reference [17]. The $\Delta J = -2$ component is the mixed pair of *gateway* levels $1^3\Sigma_g^-(v=1, N=21, f) \sim G^1\Pi_g(v=12, J=21, f)$.

The resolved fluorescence of the direct excitation $X^1\Sigma_g^+(v''=1, J''=24) \rightarrow A^1\Sigma_u^+(v'=9, J'=23) \rightarrow G^1\Pi_g(v=12, J=23, f)$ (part "A" in Figure 4.3) is given in Figure 4.9. The $\Delta J = \pm 2, \pm 4$ collisional satellite components can also be observed, according to collisional propensity rules [25, 45]. The mixed pair of *gateway* levels $1^3\Sigma_g^-(v=1, N=21, f) \sim G^1\Pi_g(v=12, J=21, f)$ corresponds to the $\Delta J = -2$ component.

4.6 Simulations

The simulations we carried out, which are based on the model described by Equations 4.2 and 4.3, are shown in Ref. [17]. The relaxation matrix Γ in Equation 4.2, which corresponds to the processes such as spontaneous decay, collisions, and laser beam transit, is of great importance in the collisional population transfer model. The spontaneous decay rate of level j,

$$W_j = \frac{1}{\tau_j},$$

is inversely proportional to its lifetime τ_j, and can be calculated from experimental molecular potentials and transition dipole moment functions. The total collisional relaxation rate (quenching rate) Γ_Q of a particular level is assumed to have the form

$$\Gamma_Q = \frac{1}{t_c},$$

where t_c is the average time between collisions

$$t_c = \frac{l}{v},$$

with the average mean free path of the $^7Li_2$ molecules

$$l = \frac{kT}{\sqrt{2}\pi d P},$$

and the most probable speed

$$v = \sqrt{\frac{2kT}{m}}.$$

The levels involved in the experiment are assumed to have the same quenching rate of $\Gamma_Q = 7.35 \times 10^{-7}$ s^{-1}, calculated using the following values for the parameters: T = 850 K, P = 5831 mTorr (obtained from P_{Ar} (293 K) = 2000 mTorr, and P_{Li}

(850 K) = 28.9 mTorr [64]), and the equilibrium internuclear distance of the ground state of $^7Li_2$ is $d = 2.67$ Å [65]. This value for Γ_Q is in good agreement with an experimentally measured quenching rate for NaK molecules [66].

The rate equation model is given in Ref. [66]. The fluorescence ratio of the collisional satellite $G^1\Pi_g(v = 12, J = 21, f) \rightarrow A^1\Sigma_u^+(v' = 10, J' = 21)$ line intensity to the direct $G^1\Pi_g(v = 12, J = 23, f) \rightarrow A^1\Sigma_u^+(v' = 10, J' = 23)$ line intensity can be experimentally measured in Figure 4.9. The collisional population transfer rate from level $|3\rangle$ to the mixed *gateway* levels $|S\rangle \sim |T\rangle$ is of the most importance in our experiment. It is only a fraction of the total collisional quenching rate Γ_Q of level $|3\rangle$. The branching ratio for the process $|3\rangle \rightarrow |S\rangle \sim |T\rangle$ from Γ_Q is calculated in Ref. [17]. The results of simulations are shown in Figures 4.6(a) and 4.8, which agree well with the experiment.

4.7 Conclusion

In this chapter, we have experimentally demonstrated that the collisional population flow between states of different spin multiplicity (singlet and triplet) can be controlled by optical fields. The control is achieved by manipulating the spin character of a pair of singlet-triplet mixed *gateway* levels using the Autler-Townes effect.

We have observed triplet fluorescence from the mixed *gateway* levels to a triplet electronic state as a function of the probe laser detuning as well as the control laser detuning. The enhancement of collisional transfer rate can be achieved by increasing the power level (Rabi frequency) of the control laser. We have also compared the singlet and triplet fluorescence with the control laser detuning over the resonance, and confirmed the conservation of the molecular population transfer.

Thus the optical control has been demonstrated to be an effective method to manipulate the transfer rate of collisions between excited molecules ($^7Li_2$) and atoms (Ar) leading to internal state changes in the molecules.

References

[7] S. H. Autler, and C. H. Townes, Phys. Rev. **100**, 703 (1955).

[16] E. H. Ahmed, S. Ingram, T. Kirova, O. Salihoglu, J. Huennekens, J. Qi, Y. Guan, and A. M. Lyyra, Phys. Rev. Lett. **107**, 163601 (2011).

[17] E. H. Ahmed, X. Pan, J. Huennekens, and A. M. Lyyra, Phys. Rev. A **89**, 061401 (2014).

[22] H. Lefebvre-Brion, and R. W. Field, *Perturbations in the spectra of diatomic molecules* (Academic Press, Orlando, 1986).

[25] H. Lefebvre-Brion, and R. W. Field, *The spectra and dynamics of diatomic molecules* (Elsevier, Amsterdam, 2004).

[35] D. R. Skinner, and R. E. Whitcher, J. Phys. E **5**, 237 (1972).

[40] S. Ingram, Ph.D. Thesis, Temple University (2010).

[45] L. Li, Q. Zhu, A. M. Lyyra, T. Whang, W. C. Stwalley, R. W. Field, and M. H. Alexander, J. Chem. Phys. **97**, 8835 (1992).

[46] L. Li, S. Antonova, A. Yiannopoulou, K. Urbanski, and A. M. Lyyra, J. Chem. Phys. **105**, 9859 (1996).

[48] T. Kirova, and F. C. Spano, Phys. Rev. A **71**, 063816 (2005).

[55] B. Barakat, R. Bacis, F. Carrot, S. Churassy, P. Crozet, F. Martin, and J. Verges, Chem. Phys. **102**, 215 (1986).

[56] K. Urbanski, S. Antonova, A. Yiannopoulou, A. M. Lyyra, L. Li, and W. C. Stwalley, J. Chem. Phys. **116**, 10557 (2002).

[57] I. Russier, A. Yiannopoulou, P. Crozet, A. Ross, F. Martin, and C. Linton, J. Mol. Spectrosc. **184**, 129 (1997).

[58] K. Urbanski, S. Antonova, A. M. Lyyra, L. Li, and B. Ji, J. Chem. Phys. **109**, 912 (1998).

[59] A. Yiannopoulou, B. Ji, L. Li, M. Li, K. Urbanski, A. M. Lyyra, W. C. Stwalley, and G. Jeung, J. Chem. Phys. **101**, 3581 (1994).

[60] M. H. Alexander, J. Chem. Phys. **76**, 429 (1982).

[61] S. Stenholm, *Foundations of laser spectroscopy* (Wiley Interscience, New York, 1984).

[62] M. O. Scully, and M. S. Zubairy, *Quantum optics* (Cambridge University Press, Cambridge, 2002).

[63] W. Demtröder, *Laser spectroscopy* (Springer-Verlag Berlin Heidelberg, New York, 1982).

[64] A. N. Nesmeyanov, *Vapor pressure of the chemical elements* (Elsevier, Amsterdam, 1963).

[65] X. Wang, J. Magnes, A. M. Lyyra, A. J. Ross, F. Martin, P. M. Dove, and R. J. LeRoy, J. Chem. Phys. **117**, 9339 (2002).

[66] C. M. Wolfe, S. Ashman, J. Bai, B. Beser, E. H. Ahmed, A. M. Lyyra, and J. Huennekens, J. Chem. Phys. **134**, 174301 (2011).

CHAPTER 5

OBSERVATION AND ANALYSIS OF THE $6^1\Sigma_g^+$ AND $3^1\Pi_g$ STATES OF RUBIDIUM DIMER

5.1 Introduction

Detailed knowledge of the excited electronic states of Rubidium dimer is of significant importance to a number of areas of research such as, the production of ultracold ground state molecules, cold atom-molecule collisions, and the development of new *ab-initio* molecular electronic structure methods. The potential energy curves and transition dipole moments of dozens of electronic states of $^{85}Rb_2$ have been calculated. However, only a few low-lying electronic states have been experimentally studied and assigned. In this chapter, our experimental work and preliminary analysis of the $6^1\Sigma_g^+$ and $3^1\Pi_g$ electronic states of $^{85}Rb_2$ are illustrated following the procedure described in Ref [67].

In the experiment, a large number of ro-vibrational levels of the two electronic states ($v = 1-18, 20-31, J = 29, 31$ for $6^1\Sigma_g^+$ state, and $v = 4-25, 27, J = 29-31$

for $3^1\Pi_g$ state) were observed using a narrow band *cw* TiSa and a dye laser in double resonance cascade configuration. The intermediate states used in the experiment are from the mutually perturbed $A^1\Sigma_g^+ \sim b^3\Pi_u$ pair of states [68]. The rotational and vibrational Dunham's coefficients in the Dunham expansion are extracted from the term values of the observed levels, and then used to generate a preliminary Rydberg-Klein-Rees (RKR) potential energy curve for each state.

5.2 Experimental Term Values

The excitation scheme and electronic states of Rubidium dimer is shown in Figure 5.1. We use a pump laser (L_1) to excite the $^{85}Rb_2$ molecule from the $X^1\Sigma_g^+$ ground state

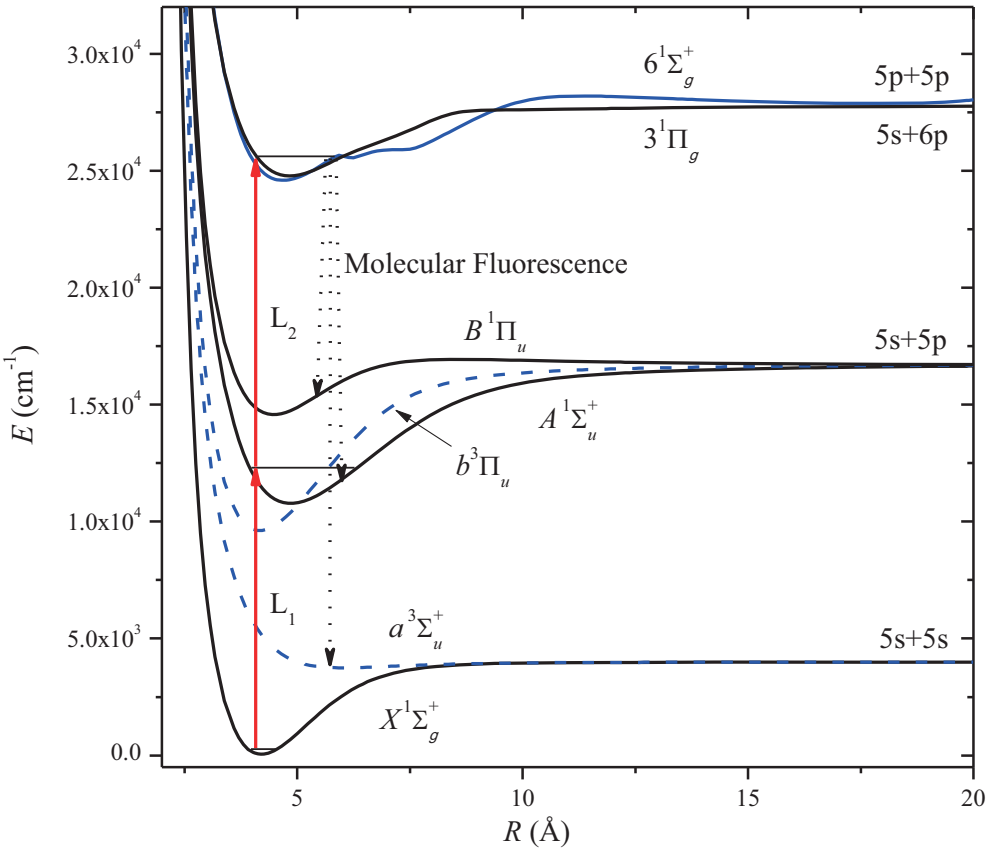

Figure 5.1: The excitation scheme and selected electronic states of $^{85}Rb_2$.

to the intermediate state, which is the mutually perturbed $A^1\Sigma_u^+ \sim b^3\Pi_u$ pair of states. The probe laser (L_2) then excites the population from the intermediate state to upper excited electronic states, which are the $6^1\Sigma_g^+$ and the $3^1\Pi_g$ states here. We observe ro-vibrational levels by detecting total molecular fluorescence from the $6^1\Sigma_g^+$ and $3^1\Pi_g$ states.

Figure 5.2 describes collisional population transfer in the $^{85}Rb_2$ optical-optical double resonance (OODR) experiment. The pump laser (L_1) excites molecules from

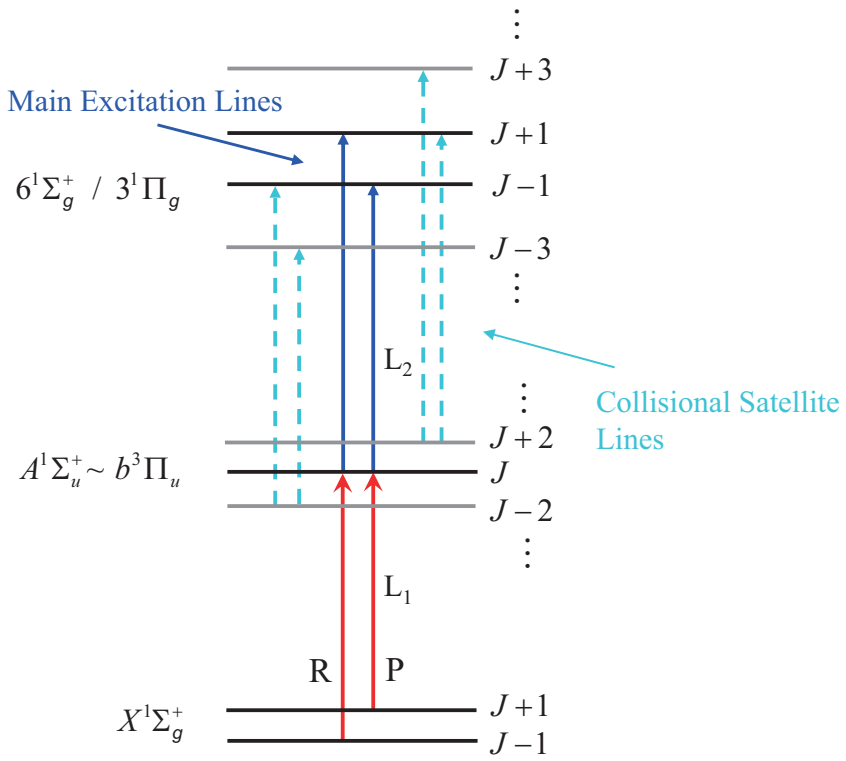

Figure 5.2: Model of collisional transfer for the $^{85}Rb_2$ OODR experiment. The pump laser (L_1) excites molecules from the $X^1\Sigma_g^+$ state to the intermediate state $A^1\Sigma_u^+ \sim b^3\Pi_u$. During collisions, population flows to nearby rotational levels according to propensity rule: $\Delta J = \pm 2, \pm 4, \cdots$. The probe laser ($L_2$) then excites the population from the intermediate state to the $6^1\Sigma_g^+$ or $3^1\Pi_g$ states, while L_1 is fixed either to the P or R branch transitions.

the $X^1\Sigma_g^+$ ground state to the intermediate $A^1\Sigma_u^+ \sim b^3\Pi_u$ state. During the collision, population flows to nearby rotational levels, according to collisional propensity

rules [25, 60]:

$$\Delta J = \pm 2, \pm 4, \cdots ,$$

$$\Delta \Omega = 0,$$

$$\Delta S = 0,$$

$$\boldsymbol{s} \not\leftrightarrow \boldsymbol{a},$$

$$e \not\leftrightarrow f,$$

$$g \not\leftrightarrow u.$$

The probe laser (L_2) then excites population from the intermediate state to excited states $6^1\Sigma_g^+$ or $3^1\Pi_g$, while L_1 is fixed either to the P or R branch excitation.

The experimental setup is shown in Figure 5.3. We use a Coherent 899-29 *cw* Titanium Sapphire laser as the pump laser (L_1), and a Coherent 699-29 *cw* dye laser operated with LD700 dye as the probe laser (L_2). Lasers L_1 and L_2 counterpropagate through the Rb_2 heatpipe, which is heated to about 470 K. The Fourier Transform Spectrometer BOMEM DA8 is used for observing the resolved fluorescence from the intermediate $A^1\Sigma_u^+ \sim b^3\Pi_u$ level to the singlet ground $X^1\Sigma_g^+$ state, by using a pierced mirror to collect the fluorescence. A Hamamatsu R928 photomultiplier tube (PMT) with a short pass filter at 520nm on one side of the Rb_2 heatpipe is used to observe the total fluorescence from the $6^1\Sigma_g^+$ and the $3^1\Pi_g$ states. An Iodine cell equipped with a PMT is used to calibrate the probe laser (L_2) simultaneously [69, 70]. A mechanical modulator is used on the probe laser to improve the signal to noise by phase sensitive detection with lock-in amplifiers.

Table 5.1 is used to determine the systematic measurement errors and calibrate the TiSa laser [71]. The reading errors are listed for both BOMEM FTIR and the Burleigh WA-1600 wavemeter at different spectral ranges based on an optogalvanic

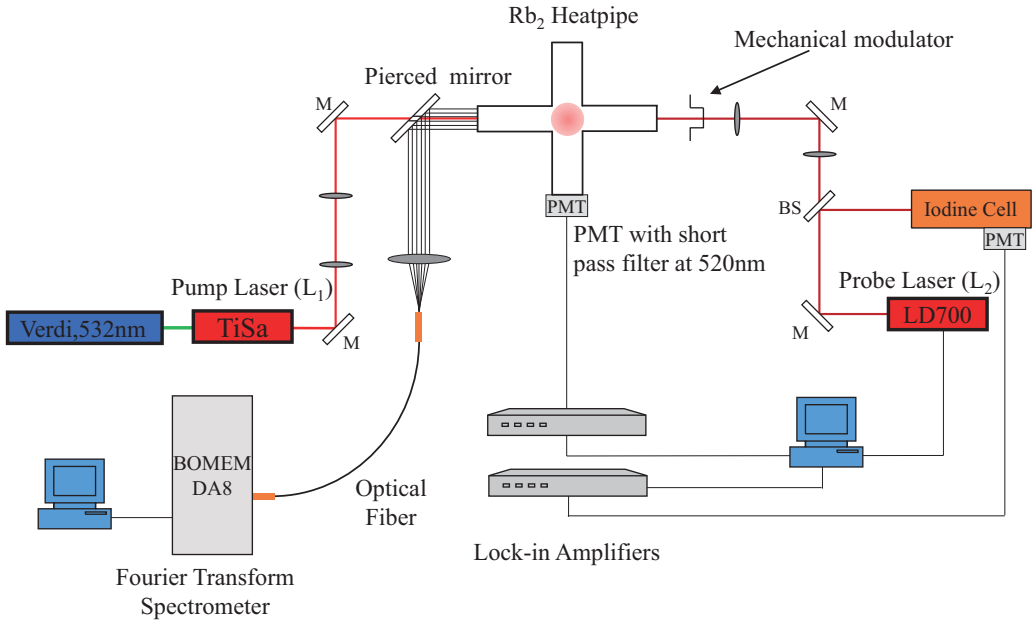

Figure 5.3: Experimental setup for observing the Rb_2 spectra. The two lasers are a narrow band tunable *cw* TiSa and a dye laser (Coherent 899-29 and 699-29, respectively). A Fourier Transform Spectrometer BOMEM DA8 is used for observing the resolved fluorescence from the intermediate $A^1\Sigma_u^+ \sim b^3\Pi_u$ level to the singlet ground $X^1\Sigma_g^+$ state. A PMT with a short pass filter at 520nm is used to observe the total fluorescence from the $6^1\Sigma_g^+$ and $3^1\Pi_g$ states. An Iodine cell is used to calibrate the probe laser.

calibration spectrum by using the Uranium lamp and its Atlas of a calibrated Uranium spectrum [72]. By adding the BOMEM FTIR systematic error to the TiSa laser wavenumber readings recorded by BOMEM, we are able to determine the calibrated readings of the TiSa laser.

The excitation spectrum of the Rb_2 molecule is very dense and congested. In order to confirm the intermediate level, we observe resolved fluorescence with the BOMEM DA8 high resolution Fourier Transform spectrometer from the target intermediate $A^1\Sigma_u^+ \sim b^3\Pi_u$ ro-vibrational level for both the R and P branch excitations. Figure 5.4 describes a portion of the resolved fluorescence following the excitation from the ground state $X^1\Sigma_g^+(v'' = 1, J'' = 29, 31)$ to the intermedi-

Table 5.1: Reading errors of the BOMEM FTIR and the Burleigh WA-1600 wavemeter. The average magnitude of the Burleigh wavemeter system error is 0.0233 cm^{-1}, and the average magnitude of the BOMEM FTIR system error is 0.0266 cm^{-1}.

U Atlas (cm^{-1})	Burleigh Wavemeter (cm^{-1})	BOMEM (cm^{-1})	Burleigh Error (cm^{-1})	BOMEM Error (cm^{-1})
11041.3737	11041.334	11041.3438	0.0397	0.0299
11010.0931	11010.087	11010.0747	0.0061	0.0184
11046.0148	11045.978	11045.9868	0.0368	0.028
11082.1804	11082.173		0.0074	
11093.1953	11093.17	11093.17	0.0253	0.0253
11112.8638	11112.831	11112.8414	0.0328	0.0224
11120.5186	11120.508	11120.4873	0.0106	0.0313
11167.6798	11167.643	11167.6525	0.0368	0.0273
11193.6145	11193.602	11193.5879	0.0125	0.0266
11199.3745	11199.35	11199.3442	0.0245	0.0303
11247.4602	11247.447	11247.434	0.0132	0.0262
11248.3361	11248.322	11248.3069	0.0141	0.0292
11267.2606	11267.218	11267.2362	0.0426	0.0244

ate level $A^1\Sigma_u^+ \sim b^3\Pi_u(n' = 148, J' = 30)$ recorded by the BOMEM FTIR. The blue line corresponds to the fluorescence resulting from the P branch excitation $A^1\Sigma_u^+ \sim b^3\Pi_u(n' = 148, J' = 30) \leftarrow X^1\Sigma_g^+(v'' = 1, J'' = 31)$, and the red line corresponds to the fluorescence resulting from the R branch excitation $A^1\Sigma_u^+ \sim b^3\Pi_u(n' = 148, J' = 30) \leftarrow X^1\Sigma_g^+(v'' = 1, J'' = 29)$. In Figure 5.4, the P-R pairs from both the P and R branches overlap very well, which confirms the target intermediate state $A^1\Sigma_u^+ \sim b^3\Pi_u(n' = 148, J' = 30)$.

After confirming the intermediate level, we fix the pump laser (L_1) on resonance of either the R or the P transition, and scan the probe laser (L_2) from the intermediate level to higher excited states. Figure 5.5 describes two examples of excitation spectra of the $6^1\Sigma_g^+$ and the $3^1\Pi_g$ states to be assigned. The blue lines correspond to the intermediate levels having been excited through the P branch by the pump laser (L_1), and the red lines represent the intermediate level excitation through the R branch by

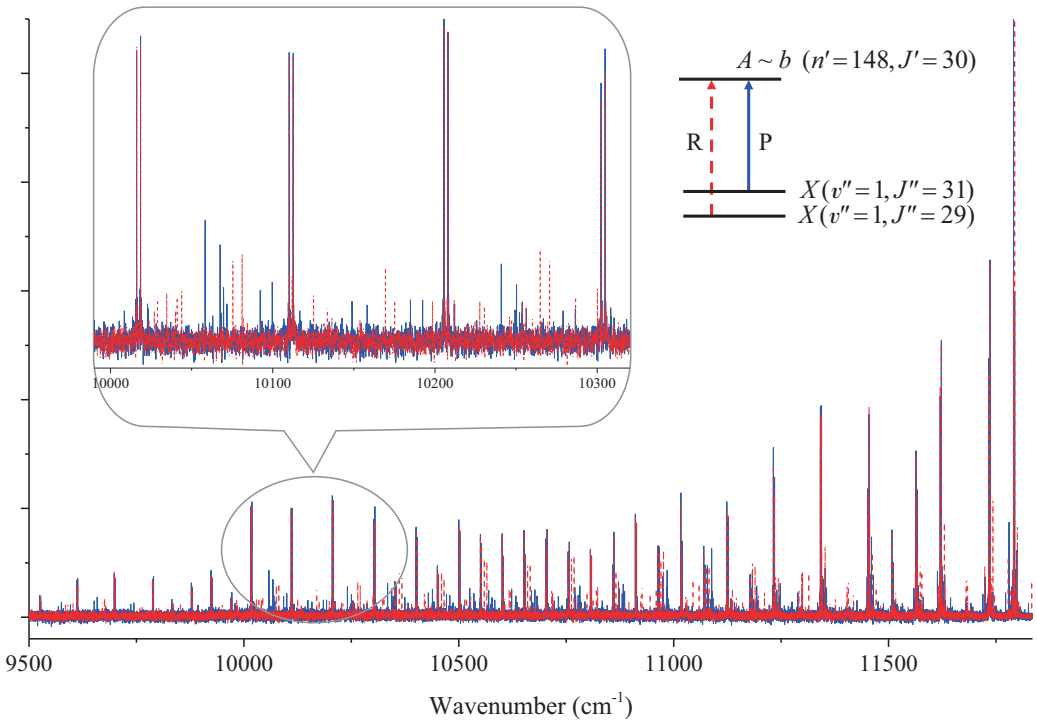

Figure 5.4: A portion of the resolved fluorescence resulting from the excitation from the ground state $X^1\Sigma_g^+(v'' = 1, J'' = 29, 31)$ to the intermediate level $A^1\Sigma_u^+ \sim b^3\Pi_u(n' = 148, J' = 30)$.

the pump laser (L_1). The overlapped main lines and collisional lines can be assigned by comparing with the calculated term values by using the program LEVEL [73] with the *ab-initio* calculated $6^1\Sigma_g^+$ and $3^1\Pi_g$ potential energy curves [74]. By using this technique, we could confirm the upper state term values, and eliminate accidental excitation.

The experimental term values of the $6^1\Sigma_g^+$ and $3^1\Pi_g$ electronic states can be calculated by adding the calibrated wavenumbers of the probe laser (L_2) to the term values of the intermediate levels $A^1\Sigma_u^+ \sim b^3\Pi_u$. The measured term values of the energy levels of the Rb_2 $6^1\Sigma_g^+$ and $3^1\Pi_g$ states are listed in Table 5.2 and Table 5.3, respectively.

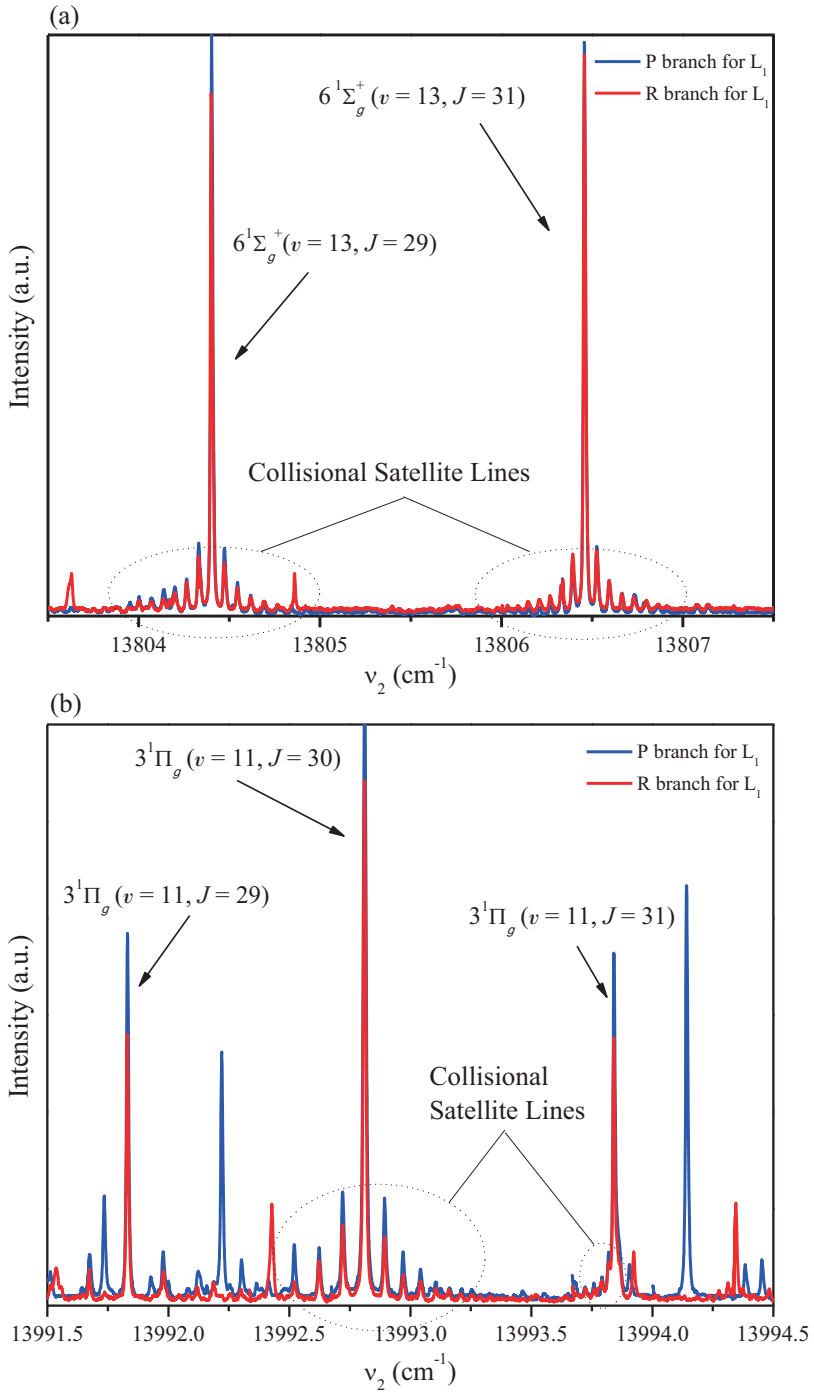

Figure 5.5: High resolution collisional spectra for the $6^1\Sigma_g^+$ and $3^1\Pi_g$ states of Rb_2. The probe laser (L_2) scans around the main lines of each state, while the pump laser (L_1) is kept on resonance of R($\Delta J = +1$) and P($\Delta J = -1$) transitions. (a) The probe laser (L_2) scan for the $6^1\Sigma_g^+ \leftarrow A^1\Sigma_u^+ \sim b^3\Pi_u(n' = 107, J' = 30)$ transition. (b) The probe laser (L_2) scan for the $3^1\Pi_g \leftarrow A^1\Sigma_u^+ \sim b^3\Pi_u(n' = 97, J' = 30)$ transition.

Table 5.2: Measured energies (in cm^{-1}) of the ro-vibrational levels of the $6^1\Sigma_g^+$ state of $^{85}Rb_2$.

v	J	Term Values	v	J	Term Values
1	29	24659.97	16	29	25329.98
1	31	24662.1494	16	31	25332.2536
2	29	24705.9665	17	29	25373.86
2	31	24708.131	17	31	25376.0308
3	29	24751.8123	18	29	25417.7018
3	31	24753.9618	18	31	25419.874
4	29	24797.4877	20	29	25503.7663
4	31	24799.6274	20	31	25505.8097
5	29	24842.9266	21	29	25545.8042
5	31	24845.0613	21	31	25547.8386
6	29	24887.8412	22	29	25586.911
6	31	24889.938	22	31	25588.8645
7	29	24933.9287	23	29	25629.9778
7	31	24936.0378	23	31	25631.9428
8	29	24978.7712	24	29	25671.3024
8	31	24980.8848	24	31	25673.2779
9	29	25023.5144	25	29	25712.5026
9	31	25025.6116	25	31	25714.4746
10	29	25068.0564	26	29	25755.2097
10	31	25070.1445	26	31	25757.0832
11	29	25112.2977	27	29	25794.9548
11	31	25114.3844	27	31	25796.8975
12	29	25156.8097	28	29	25835.5772
12	31	25158.8203	28	31	25837.4951
13	29	25199.5273	29	29	25875.7515
13	31	25201.59	29	31	25877.6399
14	29	25239.8734	30	29	25915.4258
14	31	25242.0105	30	31	25917.1451
15	29	25287.5138	31	29	25955.2645
15	31	25289.7977	31	31	25957.2285

Table 5.3: Measured energies (in cm^{-1}) of the ro-vibrational levels of the $3^1\Pi_g$ state of $^{85}Rb_2$.

v	J	Term Values	v	J	Term Values
4	29	24985.6516	15	31	25418.6752
4	30	24986.6316	16	29	25454.3962
4	31	24987.6737	16	30	25455.3620
5	29	25026.1207	16	31	25456.3505
5	30	25027.1007	17	29	25492.1212
5	31	25028.1419	17	30	25493.0832
6	29	25066.3083	17	31	25494.0838
6	30	25067.3012	18	29	25528.6782
6	31	25068.3288	18	30	25529.6290
7	29	25106.2731	18	31	25530.6266
7	30	25107.2514	19	29	25566.3162
7	31	25108.2739	19	30	25567.3022
8	29	25145.9610	19	31	25568.3789
8	30	25146.9430	20	29	25600.8979
8	31	25147.9597	20	30	25601.7934
9	29	25185.3663	20	31	25602.9393
9	30	25186.3398	21	29	25637.6378
9	31	25187.3587	21	30	25638.5258
10	29	25224.3925	21	31	25639.5482
10	30	25225.3679	22	29	25672.9555
10	31	25226.3863	22	30	25673.8644
11	29	25263.4122	22	31	25674.8627
11	30	25264.3986	23	29	25708.4558
11	31	25265.4224	23	30	25709.4013
12	29	25303.8721	23	31	25710.4269
12	30	25304.8865	24	29	25743.4395
12	31	25305.9911	24	30	25744.6234
13	29	25343.1205	24	31	25745.4898
13	30	25344.1365	25	29	25778.3983
13	31	25345.4595	25	30	25779.4768
14	29	25378.3863	25	31	25780.3808
14	30	25379.3362	27	29	25849.8777
14	31	25380.4478	27	30	25850.6364
15	29	25416.6793	27	31	25851.9337
15	30	25417.7978			

5.3 The Vibrational and Rotational Coefficients in the Dunham Expansion

As stated in Section 2.3, according to Dunham's study of the interaction of vibration and rotation [27], the term values of the vibrating rotator can be written in the form of a polynomial expansion,

$$T_{v,J} = \sum_{l,m} Y_{lm} \left(v + \frac{1}{2}\right)^l \left[J(J+1) - \Omega^2\right]^m . \tag{5.1}$$

Here the v, J are the vibrational and rotational quantum numbers, respectively. The Y_{lm} parameters are the Dunham's coefficients, and Y_{l0} and Y_{0m} denote the vibrational and rotational coefficients, respectively. Ω is the component of the total electronic spin and orbital angular momentum along the internuclear axis. The vibrational and rotational energies are given by

$$G_v = \sum_{l(l\neq 0)} Y_{l0} \left(v + \frac{1}{2}\right)^l = \omega_e \left(v + \frac{1}{2}\right) - \omega_e x_e \left(v + \frac{1}{2}\right)^2 + \cdots , \tag{5.2}$$

and

$$F_v(J) = \sum_{m(m\neq 0)} Y_{0m}[J(J+1)]^m = B_v J(J+1) - D_v[J(J+1)]^2 + \cdots , \tag{5.3}$$

with

$$B_v = B_e - \alpha_e \left(v + \frac{1}{2}\right) + \cdots ,$$

$$D_v = D_e + \beta_e \left(v + \frac{1}{2}\right) + \cdots .$$

The $\omega_e, \omega_e x_e$ parameters are the harmonic vibrational frequency, and the vibrational anharmonicity constant, respectively. B_v and D_v are the rotational and centrifugal distortion constants, respectively, and depend on the vibrational quantum number v.

B_e is rotational constant at equilibrium internuclear distance, and $\alpha_e \ll B_e$. D_e refers to the completely vibrationless state, and $\beta_e \ll D_e$. These spectroscopic constants have the relations

$$Y_{10} = \omega_e, \quad Y_{20} = -\omega_e x_e, \quad Y_{01} = B_e, \quad Y_{02} = -D_e, \quad Y_{11} = -\alpha_e, \quad \cdots$$

and can be experimentally determined for most electronic states.

The ro-vibrational level energies for a given vibrational state can be expressed as,

$$E_v(J) = G_v + B_v J(J+1) - D_v[J(J+1)]^2 + \cdots . \tag{5.4}$$

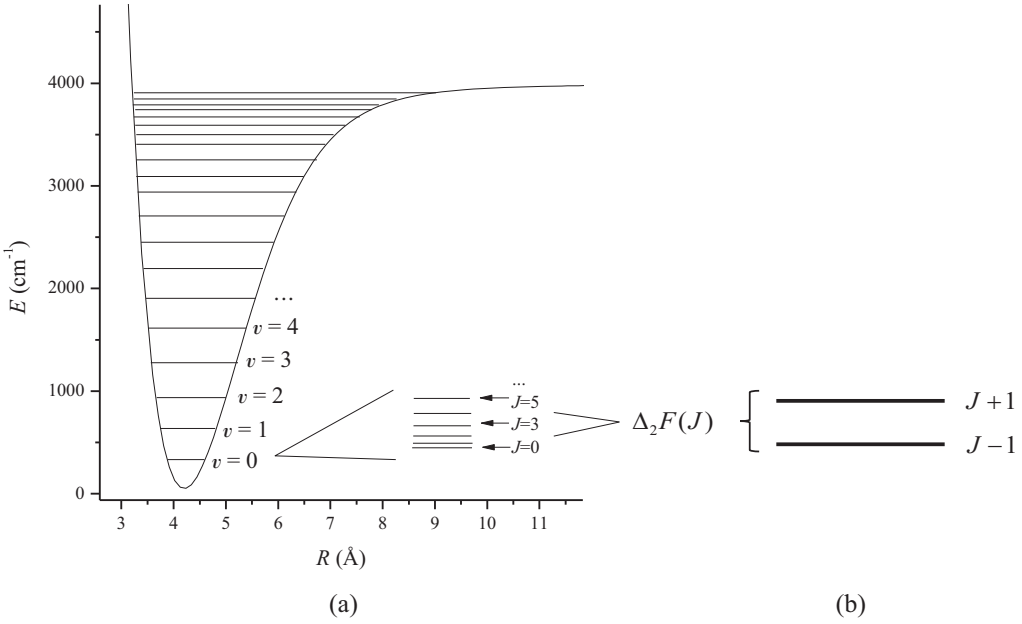

Figure 5.6: (a) An anharmonic potential energy curve with vibrational level spacing illustrated. Within each vibrational level there is a series of rotational levels. (b) The second combination difference $\Delta_2 F(J)$ is defined as the energy difference between the levels with rotational quantum numbers $J-1$ and $J+1$, within the vibrational level v.

The second combination difference (see Figure 5.6) can be described as

$$\Delta_2 F(J) = F(J+1) - F(J-1), \tag{5.5}$$

therefore,

$$\Delta_2 F(J) = 4B_v \left(J + \frac{1}{2}\right) - 8D_v \left(J + \frac{1}{2}\right)^3. \tag{5.6}$$

D_v is often very small compared to B_v, and as a result the second term of the left part of formula 5.6 is negligible. Subsequently, the B_v values can be calculated from experimental spectroscopic ro-vibrational data. By fitting the polynomial curve as a function of $v + \frac{1}{2}$, we obtain a set of coefficients which represent $Y_{01}, Y_{11}, \cdots$ in the Dunham expansion (5.1).

The G_v values can be further calculated from the fitted B_v values according to Equation 5.4, and fitted as a function of $v + \frac{1}{2}$. The fitted coefficients are $Y_{10}, Y_{20}, Y_{30}, \cdots$ in the Dunham expansion (5.1).

There is also a non-vanishing term Y_{00} in the Equation 5.1, which modifies the energy of the vibrational level $v = 0$,

$$Y_{00} = \frac{Y_{01} + Y_{20}}{4} - \frac{Y_{11}Y_{10}}{12Y_{01}} + \frac{Y_{11}^2 Y_{10}^2}{144Y_{01}^3}.$$

This is the zero energy correction term, which is also denoted by T_e.

Tables 5.4 and 5.5 show the results for the fitted B_v and G_v values based on the experimentally measured ro-vibrational energies for $6^1\Sigma_g^+$ and $3^1\Pi_g$ states, respectively. Figures 5.7 and 5.8 give the results of preliminary Dunham's coefficients extracted from the observed ro-vibrational energies for each state.

Table 5.4: Calculation of B_v and G_v values based on the experimental ro-vibrational energies for the $6^1\Sigma_g^+$ state of $^{85}Rb_2$.

v	J	Experiment	$\Delta_2F(J)$	$v+\frac{1}{2}$	B_v	Fitted B_v	Calculated G_v
1	29	24659.9700	2.1794	1.5	0.01786	0.01785	24644.4419
	31	24662.1494					
2	29	24705.9665	2.1645	2.5	0.01774	0.01777	24690.5089
	31	24708.1310					
3	29	24751.8123	2.1495	3.5	0.01762	0.01769	24736.4252
	31	24753.9618					
4	29	24797.4877	2.1397	4.5	0.01754	0.01761	24782.1712
	31	24799.6274					
5	29	24842.9266	2.1346	5.5	0.01750	0.01752	24827.6806
	31	24845.0613					
6	29	24887.8412	2.0968	6.5	0.01719	0.01744	24872.6657
	31	24889.9380					
7	29	24933.9287	2.1091	7.5	0.01729	0.01736	24918.8238
	31	24936.0378					
8	29	24978.7712	2.1135	8.5	0.01732	0.01728	24963.7368
	31	24980.8848					
9	29	25023.5144	2.0972	9.5	0.01719	0.01720	25008.5506
	31	25025.6116					
10	29	25068.0564	2.0881	10.5	0.01712	0.01712	25053.1631
	31	25070.1445					
11	29	25112.2977	2.0867	11.5	0.01710	0.01704	25097.4750
	31	25114.3844					
12	29	25156.8097	2.0106	12.5	0.01648	0.01696	25142.0575
	31	25158.8203					
13	29	25199.5273	2.0627	13.5	0.01691	0.01688	25184.8456
	31	25201.5900					
14	29	25239.8734	2.1371	14.5	0.01752	0.01679	25225.2622
	31	25242.0105					
15	29	25287.5138	2.2840	15.5	0.01872	0.01671	25272.9731
	31	25289.7977					

(Continued on next page)

Table 5.4: (*continued*)

v	J	Experiment	$\Delta_2 F(J)$	$v+\frac{1}{2}$	B_v	Fitted B_v	Calculated G_v
16	29	25329.9800	2.2736	16.5	0.01864	0.01663	25315.5099
	31	25332.2536					
17	29	25373.8600	2.1708	17.5	0.01779	0.01655	25359.4605
	31	25376.0308					
18	29	25417.7018	2.1722	18.5	0.01780	0.01647	25403.3727
	31	25419.8740					
20	29	25503.7663	2.0434	20.5	0.01675	0.01631	25489.5784
	31	25505.8097					
21	29	25545.8042	2.0344	21.5	0.01668	0.01623	25531.6868
	31	25547.8386					
22	29	25586.9110	1.9535	22.5	0.01601	0.01615	25572.8641
	31	25588.8645					
23	29	25629.9778	1.9650	23.5	0.01611	0.01606	25616.0015
	31	25631.9428					
24	29	25671.3024	1.9755	24.5	0.01619	0.01598	25657.3966
	31	25673.2779					
25	29	25712.5026	1.9721	25.5	0.01616	0.01590	25698.6673
	31	25714.4746					
26	29	25755.2097	1.8735	26.5	0.01536	0.01582	25741.4449
	31	25757.0832					
27	29	25794.9548	1.9427	27.5	0.01592	0.01574	25781.2606
	31	25796.8975					
28	29	25835.5772	1.9179	28.5	0.01572	0.01566	25821.9535
	31	25837.4951					
29	29	25875.7515	1.8884	29.5	0.01548	0.01558	25862.1984
	31	25877.6399					
30	29	25915.4258	1.7192	30.5	0.01409	0.01550	25901.9432
	31	25917.1451					
31	29	25955.2645	1.9640	31.5	0.01610	0.01542	25941.8524
	31	25957.2285					

Table 5.5: Calculation of B_v and G_v values based on the experimental ro-vibrational energies for the $3^1\Pi_g$ state of $^{85}Rb_2$.

v	J	Experiment	$\Delta_2F(J)$	$v+\frac{1}{2}$	B_v	Fitted B_v	Calculated G_v
4	29	24985.6516	2.0221	4.5	0.01657	0.01643	24971.3562
	30	24986.6316					
	31	24987.6737					
5	29	25026.1207	2.0213	5.5	0.01657	0.01643	25011.8231
	30	25027.1007					
	31	25028.1419					
6	29	25066.3083	2.0205	6.5	0.01656	0.01644	25052.0085
	30	25067.3012					
	31	25068.3288					
7	29	25106.2731	2.0009	7.5	0.01640	0.01644	25091.9710
	30	25107.2514					
	31	25108.2739					
8	29	25145.9610	1.9987	8.5	0.01638	0.01644	25131.6568
	30	25146.9430					
	31	25147.9597					
9	29	25185.3663	1.9924	9.5	0.01633	0.01644	25171.0598
	30	25186.3398					
	31	25187.3587					
10	29	25224.3925	1.9938	10.5	0.01634	0.01645	25210.0838
	30	25225.3679					
	31	25226.3863					
11	29	25263.4122	2.0102	11.5	0.01648	0.01645	25249.1013
	30	25264.3986					
	31	25265.4224					
12	29	25303.8721	2.1190	12.5	0.01737	0.01645	25289.5590
	30	25304.8865					
	31	25305.9911					
13	29	25343.1205	2.3390	13.5	0.01917	0.01645	25328.8051
	30	25344.1365					
	31	25345.4595					
14	29	25378.3863	2.0615	14.5	0.01690	0.01646	25364.0688

(Continued on next page)

Table 5.5: (*continued*)

v	J	Experiment	$\Delta_2 F(J)$	$v+\frac{1}{2}$	B_v	Fitted B_v	Calculated G_v
	30	25379.3362					
	31	25380.4478					
15	29	25416.6793	1.9959	15.5	0.01636	0.01646	25402.3595
	30	25417.7978					
	31	25418.6752					
16	29	25454.3962	1.9543	16.5	0.01602	0.01646	25440.0742
	30	25455.3620					
	31	25456.3505					
17	29	25492.1212	1.9626	17.5	0.01609	0.01646	25477.7970
	30	25493.0832					
	31	25494.0838					
18	29	25528.6782	1.9484	18.5	0.01597	0.01647	25514.3517
	30	25529.6290					
	31	25530.6266					
19	29	25566.3162	2.0627	19.5	0.01691	0.01647	25551.9876
	30	25567.3022					
	31	25568.3789					
20	29	25600.8979	2.0414	20.5	0.01673	0.01647	25586.5670
	30	25601.7934					
	31	25602.9393					
21	29	25637.6378	1.9104	21.5	0.01566	0.01647	25623.3047
	30	25638.5258					
	31	25639.5482					
22	29	25672.9555	1.9073	22.5	0.01563	0.01648	25658.6202
	30	25673.8644					
	31	25674.8627					
23	29	25708.4558	1.9711	23.5	0.01616	0.01648	25694.1183
	30	25709.4013					
	31	25710.4269					
24	29	25743.4395	2.0503	24.5	0.01681	0.01648	25729.0997
	30	25744.6234					
	31	25745.4898					

(Continued on next page)

Table 5.5: (*continued*)

v	J	Experiment	$\Delta_2 F(J)$	$v+\frac{1}{2}$	B_v	Fitted B_v	Calculated G_v
25	29	25778.3983	1.9824	25.5	0.01625	0.01648	25764.0564
	30	25779.4768					
	31	25780.3808					
27	29	25849.8777	2.0560	27.5	0.01685	0.01649	25835.5313
	30	25850.6364					
	31	25851.9337					

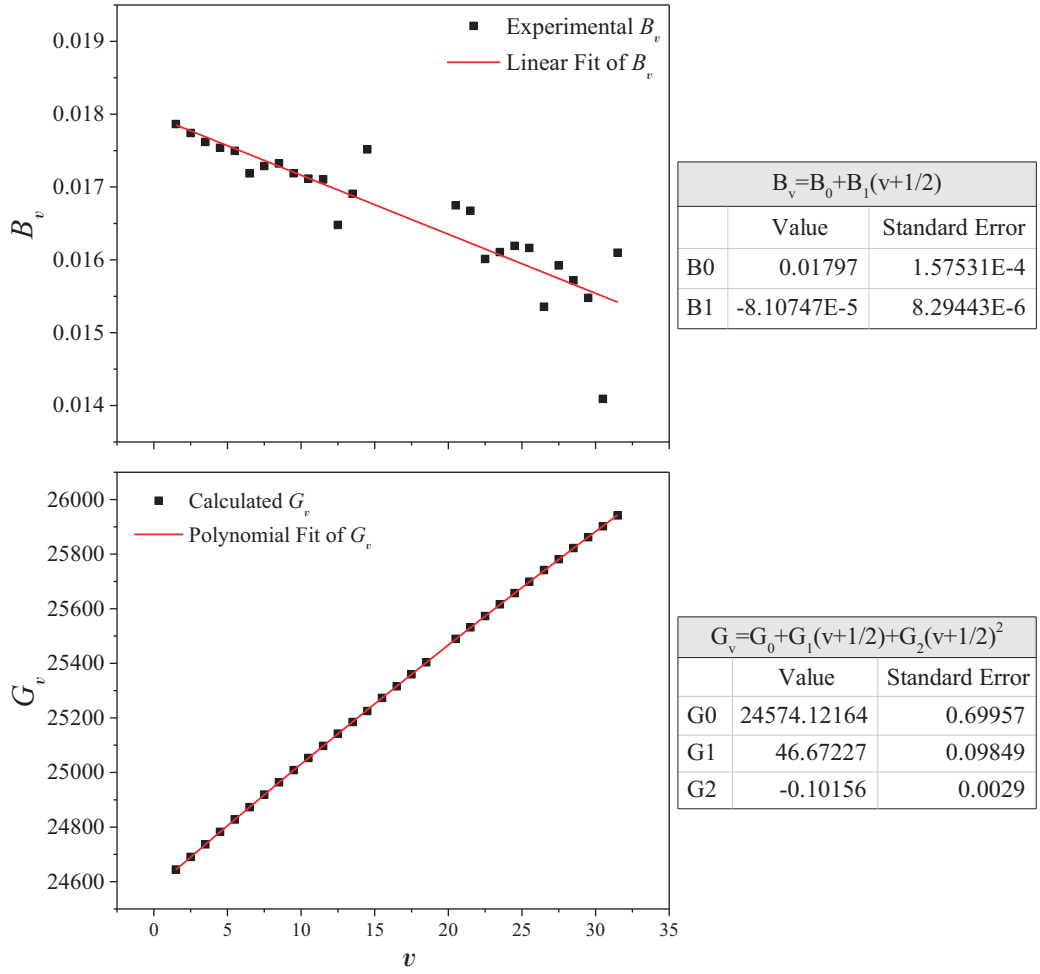

$B_v=B_0+B_1(v+1/2)$		
	Value	Standard Error
B0	0.01797	1.57531E-4
B1	-8.10747E-5	8.29443E-6

$G_v=G_0+G_1(v+1/2)+G_2(v+1/2)^2$		
	Value	Standard Error
G0	24574.12164	0.69957
G1	46.67227	0.09849
G2	-0.10156	0.0029

Figure 5.7: Preliminary Dunham's coefficients extracted from the fitted B_v and G_v values for the $6^1\Sigma_g^+$ state of $^{85}Rb_2$.

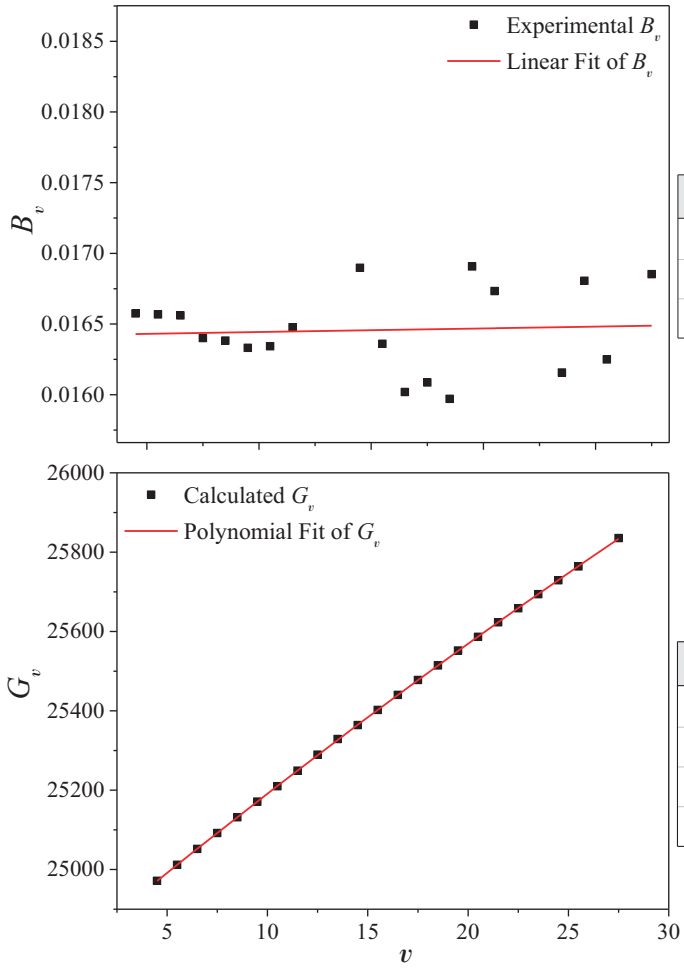

$B_v=B_0+B_1(v+1/2)$		
	Value	Standard Error
B0	0.01642	1.63601E-4
B1	2.54825E-6	9.80957E-6

$G_v=G_0+G_1(v+1/2)+G_2(v+1/2)^2$		
	Value	Standard Error
G0	24784.61014	0.96227
G1	42.08372	0.13595
G2	-0.14285	0.00426

Figure 5.8: Preliminary Dunham's coefficients extracted from the fitted B_v and G_v values for the $3^1\Pi_g$ state of $^{85}Rb_2$.

5.4 Rydberg-Klein-Rees (RKR) Potential Energy Curves

After extracting the preliminary Dunham's coefficients from the measured spectroscopic ro-vibrational energies, we use the Rydberg-Klein-Rees (RKR) [75–78] method to construct the preliminary potential energy curves for the $6^1\Sigma_g^+$ and $3^1\Pi_g$ states.

Using this method, the inner and outer turning points of the molecular vibrational motion, $R_-(v), R_+(v)$, can be expressed by Klein Integrals, f and g,

$$R_+(v) - R_-(v) = 2\sqrt{\frac{\mathbb{C}_u}{\mu}} \int_{v_{\min}}^{v} \frac{\mathrm{d}v'}{\sqrt{G_v - G_{v'}}} = 2f, \tag{5.7a}$$

$$\frac{1}{R_-(v)} - \frac{1}{R_+(v)} = 2\sqrt{\frac{\mu}{\mathbb{C}_u}} \int_{v_{\min}}^{v} \frac{B_{v'}\mathrm{d}v'}{\sqrt{G_v - G_{v'}}} = 2g. \tag{5.7b}$$

where the vibrational energy G_v and the rotational constant B_v are in cm^{-1} units, μ is the reduced mass of the nuclei in amu, the turning points are in units Å, and $v_{\min}$ is the non-integer effective value of the vibrational quantum number at the potential minimum. The constant $\mathbb{C}_u = \hbar^2/2 = 16.857\,629\,09$ [amu·Å^2·cm^{-1}]. By solving the integrals, we can get inner and outer turning points for a particular vibrational level from our experimental ro-vibrational energies,

$$R_-(v) = \sqrt{f^2 + \frac{f}{g}} - f, \tag{5.8a}$$

$$R_+(v) = \sqrt{f^2 + \frac{f}{g}} + f. \tag{5.8b}$$

Table 5.6: Preliminary Dunham's coefficients Y_{lm} (in cm^{-1}) for the $6^1\Sigma_g^+$ and $3^1\Pi_g$ states of $^{85}Rb_2$ extracted from experimental ro-vibrational energies.

	$6^1\Sigma_g^+$		$3^1\Pi_g$	
	Value	Standard Error	Value	Standard Error
T_e	24574.12164	0.69957	24784.61014	0.96227
Y_{10}	46.67227	0.09849	42.08372	0.13595
Y_{20}	-0.10156	0.0029	-0.14285	0.00426
Y_{01}	0.01797	1.57531E-4	0.01642	1.63601E-4
Y_{11}	-8.10747E-5	8.29443E-6	2.54825E-6	9.80957E-6

With the Dunham's coefficients listed in Table 5.6 as the input file, we run LeRoy's

Table 5.7: Preliminary RKR potential function calculated for the $6^1\Sigma_g^+$ state of $^{85}Rb_2$ based on Dunham's coefficients in Table 5.6.

$E_v(\text{cm}^{-1})$	$R_-(\text{Å})$	$R_+(\text{Å})$	$E_v(\text{cm}^{-1})$	$R_-(\text{Å})$	$R_+(\text{Å})$
24578.8016	4.6433	4.7601	24918.4647	4.2699	5.2944
24588.1279	4.6027	4.8050	24963.5120	4.2469	5.3395
24597.4461	4.5754	4.8366	25008.3562	4.2257	5.3830
24606.7562	4.5535	4.8627	25052.9972	4.2060	5.4250
24616.0582	4.5349	4.8856	25097.4352	4.1877	5.4658
24625.3520	4.5185	4.9063	25141.6700	4.1705	5.5056
24634.6377	4.5037	4.9254	25185.7017	4.1543	5.5444
24643.9153	4.4901	4.9433	25229.5303	4.1390	5.5825
24690.1813	4.4345	5.0205	25273.1558	4.1246	5.6198
24736.2442	4.3910	5.0857	25316.5781	4.1108	5.6565
24782.1040	4.3546	5.1438	25359.7974	4.0978	5.6927
24827.7607	4.3231	5.1972	25402.8135	4.0853	5.7284
24873.2142	4.2951	5.2471	25445.6265	4.0734	5.7636

Table 5.8: Preliminary RKR potential energy curve calculated for the $3^1\Pi_g$ state of $^{85}Rb_2$ based on Dunham's coefficients in Table 5.6.

$E_v(\text{cm}^{-1})$	$R_-(\text{Å})$	$R_+(\text{Å})$	$E_v(\text{cm}^{-1})$	$R_-(\text{Å})$	$R_+(\text{Å})$
24788.7849	4.8566	4.9791	24971.0620	4.5166	5.3514
24797.1902	4.8122	5.0249	25011.7172	4.4750	5.4007
24805.5841	4.7818	5.0567	25052.0867	4.4370	5.4463
24813.9666	4.7572	5.0828	25092.1706	4.4019	5.4892
24822.3376	4.7360	5.1054	25131.9687	4.3690	5.5300
24830.6972	4.7171	5.1258	25171.4811	4.3379	5.5690
24839.0454	4.6999	5.1444	25210.7078	4.3084	5.6066
24847.3821	4.6840	5.1618	25249.6488	4.2802	5.6429
24888.8945	4.6173	5.2359	25288.3042	4.2532	5.6782
24930.1211	4.5632	5.2973	25326.6738	4.2271	5.7126

"RKR" program [79] to construct the preliminary potential energy curves for the $6^1\Sigma_g^+$ and $3^1\Pi_g$ states of $^{85}Rb_2$. The results are listed in Tables 5.7 and 5.8.

Thereafter the ro-vibrational energies are reproduced by using the LEVEL [73] program to calculate numerically the ro-vibrational energy eigenvalues by solving the radial Schrödinger equation with the preliminary RKR potential energy curves for comparison with the observed energies that we measured. Figure 5.9 shows the residuals between the measured ro-vibrational energies and the energies reproduced from the preliminary RKR curves. By comparison of the energies (Appendix 5.6), we can test the quality of the potential energy curves we constructed.

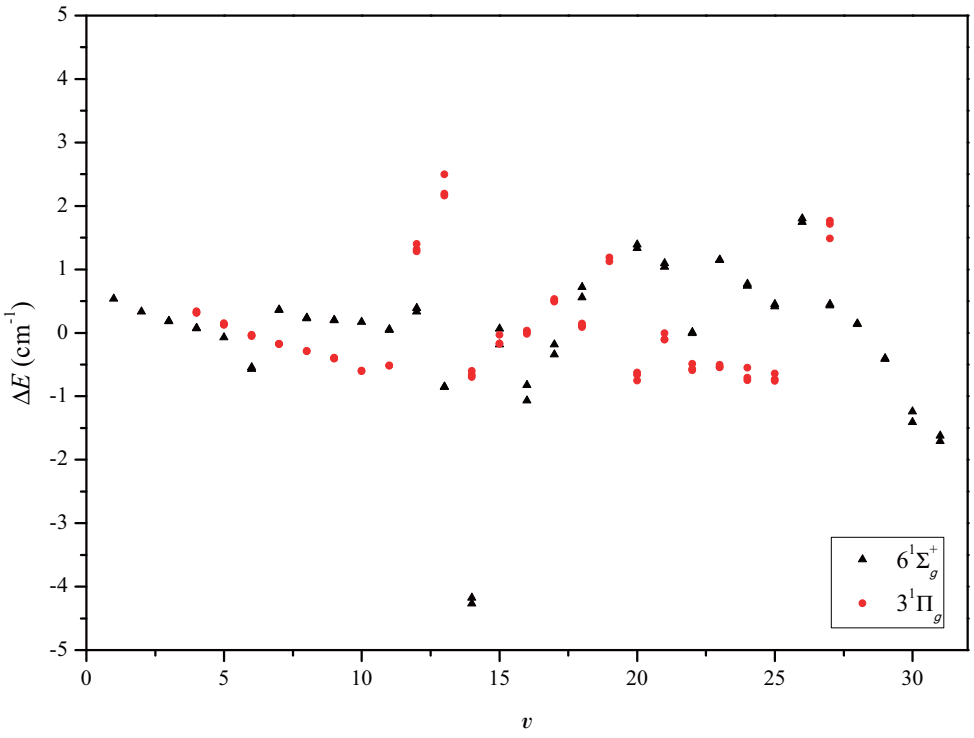

Figure 5.9: Residuals between experimentally measured ro-vibrational energies and reproduced eigenvalues from preliminary RKR curves as a function of v for the $6^1\Sigma_g^+$ and $3^1\Pi_g$ states of $^{85}Rb_2$.

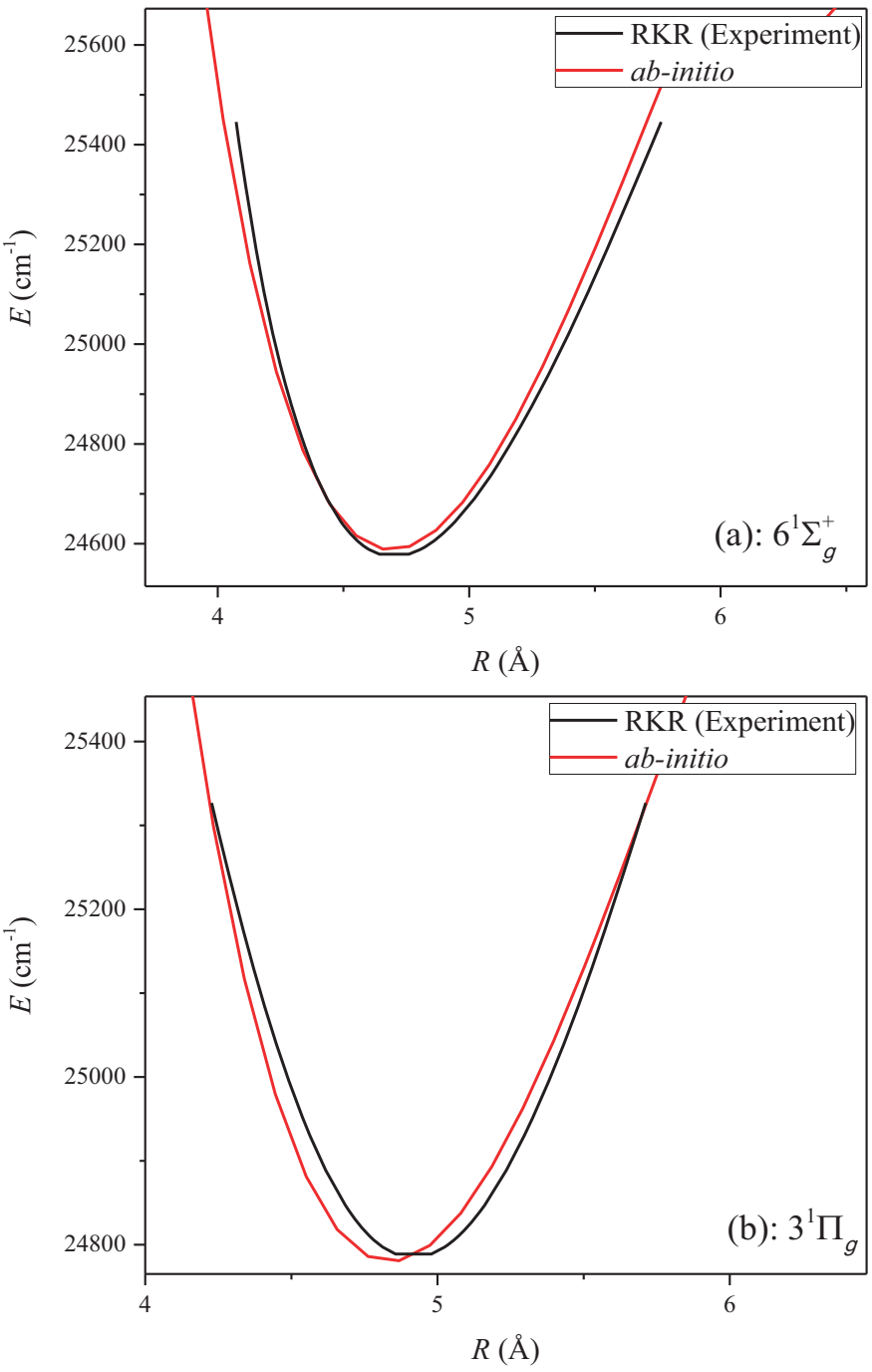

Figure 5.10: Preliminary calculated RKR potential energy curves constructed using the Dunham's coefficients in Table 5.6 for the $6^1\Sigma_g^+$ and $3^1\Pi_g$ states of $^{85}Rb_2$, and compared with *ab-initio* curves [74].

Figure 5.10 shows the preliminary RKR potential energy curves based on our experimental data, compared with *ab-initio* curves [74]. The *ab-initio* curves are not too far off from the preliminary RKR curves.

In order to see the difference between the *ab-initio* curves and our preliminary RKR curves, the LEVEL [73] program is used to calculate the ro-vibrational energy eigenvalues from the *ab-initio* potential energy curves as well (Appendix 5.6). Figure 5.11 illustrates the residuals between the two ro-vibrational energies. The agreement is better at lower vibrational quantum numbers.

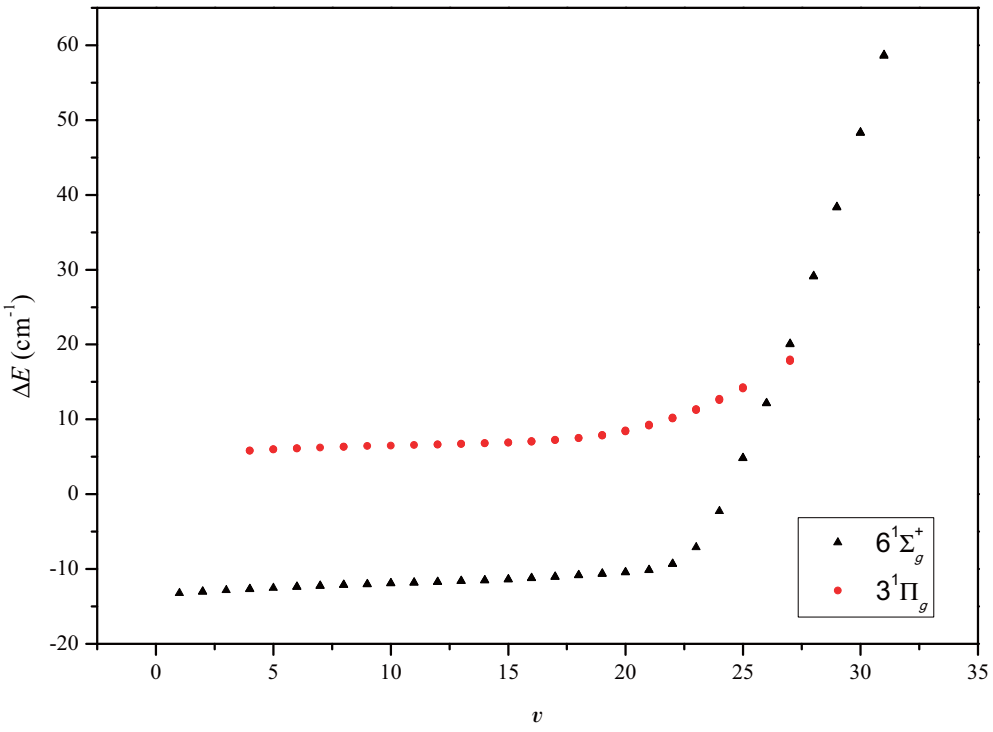

Figure 5.11: Residuals between calculated ro-vibrational eigenvalues from preliminary RKR curves and *ab-intio* curves [74] as a function of v for the $6^1\Sigma_g^+$ and $3^1\Pi_g$ states of $^{85}Rb_2$.

5.5 Assignment of the Collisional Lines

After determining the term values of the main excitation lines, we could confirm the quantum numbers of the collisional lines, by comparing with theoretical term values of the intermediate $A^1\Sigma_u^+ \sim b^3\Pi_u$ levels (see Figure 5.2).

Since the term values of the main lines have already been determined from previous sections, by subtracting the fluorescence frequencies of the collisional lines from the term values of the main lines, the experimental term values of the intermediate $A^1\Sigma_u^+ \sim b^3\Pi_u$ levels could be determined. Thereafter, the rotational quantum number J could be determined by comparing with theoretical values [68]. Figure 5.12 gives an example of the assignment of the collisional lines.

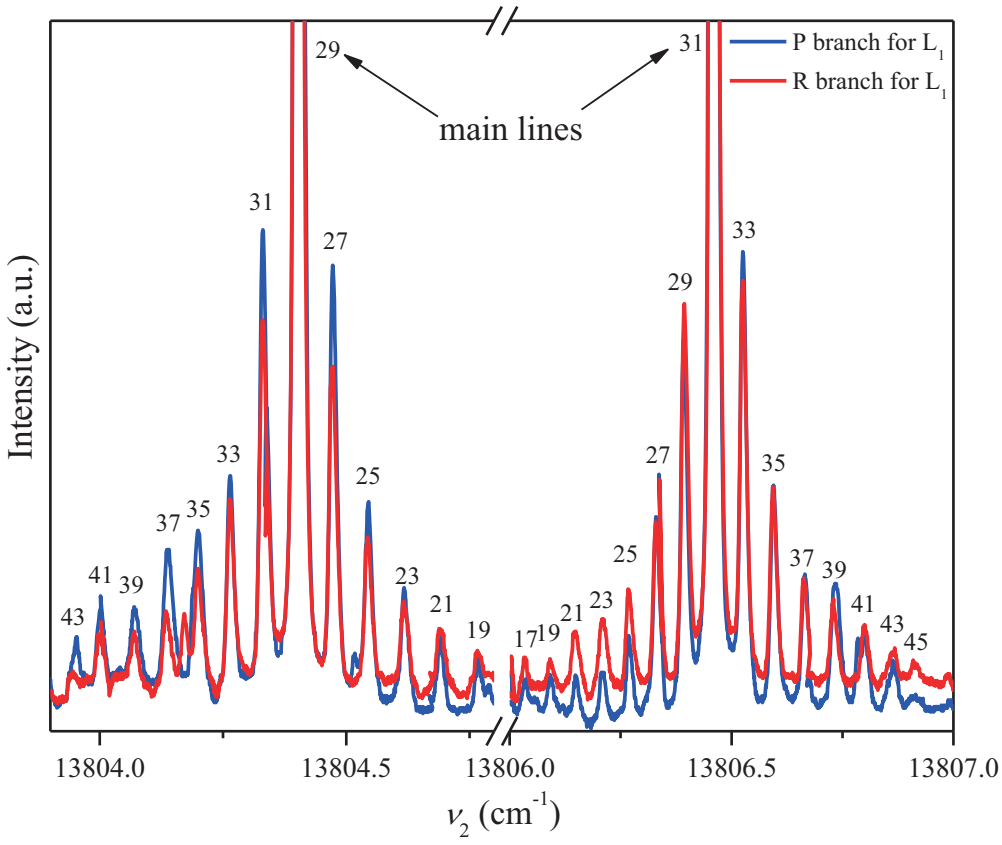

Figure 5.12: Laser induced fluorescence probe laser scan of the direct excitation from $A^1\Sigma_u^+ \sim b^3\Pi_u(n' = 107, J' = 30)$ to $6^1\Sigma_g^+(v = 13, J = 29, 31)$, and the $\Delta J = \pm 2, \pm 4, \cdots$ collisional satellite components.

Figure 5.13 describes all observed levels for the $6^1\Sigma_g^+$ and $3^1\Pi_g$ states of $^{85}Rb_2$ after assigning all the main lines as well as the collisional satellite lines from the experimental data.

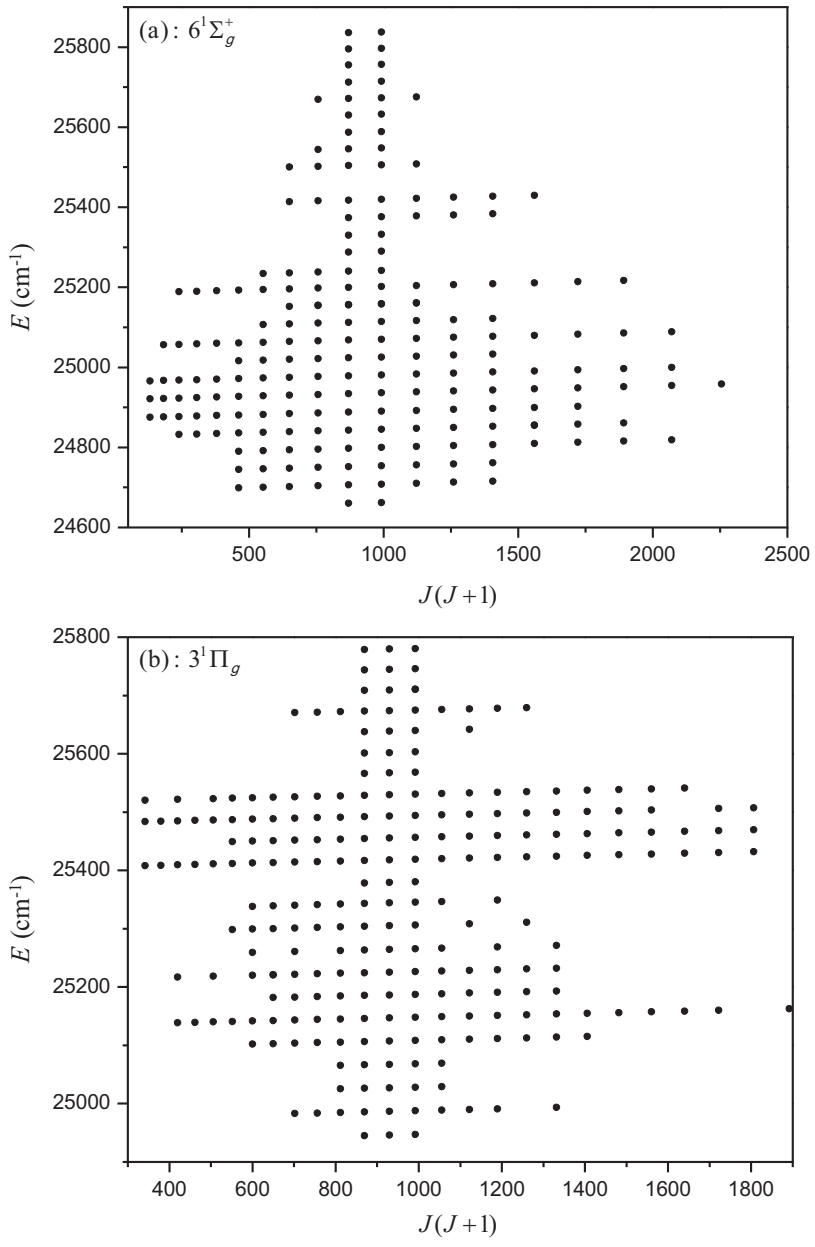

Figure 5.13: All observed levels for the $6^1\Sigma_g^+$ and $3^1\Pi_g$ states of $^{85}Rb_2$ from the experimental data.

5.6 Conclusion

In this chapter, we have described the observation of a large number of ro-vibrational levels of the $6^1\Sigma_g^+$ and $3^1\Pi_g$ electronic states of $^{85}Rb_2$ by using optical-optical double resonance (OODR) spectroscopy. In order to confirm the intermediate states, we compared the P-R pairs of the resolved fluorescence of the excitation from the ground state $X^1\Sigma_g^+$ to the intermediate level $A^1\Sigma_u^+ \sim b^3\Pi_u$ for both R($\Delta J = +1$) and P($\Delta J = -1$) branches. By keeping the pump laser on resonance of both R and P transitions, we could confirm the overlapped main lines and collisional lines, and eliminate accidental excitation.

The rotational and vibrational Dunham coefficients that have been extracted from the experimental data are used to calculate the preliminary Rydberg-Klein-Rees (RKR) potential energy curves for the $6^1\Sigma_g^+$ and $3^1\Pi_g$ states. In order to test the quality of the experimental potential energy curves, we calculated the ro-vibrational eigenvalues from the preliminary RKR curves by using the LEVEL program for comparison with the experimental ro-vibrational energy values. We also compared the ro-vibrational eigenvalues calculated from the *ab-initio* curves with our preliminary RKR potential energy curves.

By comparing with the theoretical term values of the intermediate $A^1\Sigma_u^+ \sim b^3\Pi_u$ states, we could confirm the quantum numbers of the collisional lines, and get additional term values for the $6^1\Sigma_g^+$ and $3^1\Pi_g$ states.

References

[25] H. Lefebvre-Brion, and R. W. Field, *The spectra and dynamics of diatomic molecules* (Elsevier, Amsterdam, 2004).

[27] J. L. Dunham, Phys. Rev. **41**, 721 (1932).

[60] M. H. Alexander, J. Chem. Phys. **76**, 429 (1982).

[67] A. M. Lyyra, W. T. Luh, L. Li, H. Wang, and W. C. Stwalley, J. Chem. Phys. **92**, 43 (1990).

[68] H. Salami, T. Bergeman, B. Beser, J. Bai, E. H. Ahmed, S. Kotochigova, A. M. Lyyra, J. Huennekens, C. Lisdat, A. V. Stolyarov, O. Dulieu, P. Crozet, and A. J. Ross, EPAPS of Phys. Rev. A **80**, 022515 (2009).

[69] S. Gerstenkorn, and P. Luc, Rev. Phys. Appl. (Paris) **14**, 791 (1979).

[70] S. Gerstenkorn, and P. Luc, *Atlas du spectre d'absorption de la molécule de l'iode entre* 14 800-20 000 cm^{-1} (Editions du C.N.R.S., 15, quai Anatole-France, 75700 Paris).

[71] J. Bai, Ph.D. Thesis, Temple University (2011).

[72] B. A. Palmer, R. A. Keller, and R. Engleman, Jr, LASL Report No. LA-8251-MS (Los Alamos Scientific Laboratory, Los Alamos, NM, 1980).

[73] R. J. LeRoy, University of Waterloo Chemical Physics Research Report No. CP663, 2007.

[74] W. Jastrzebski, P. Kowalczyk, J. Szczepkowski, A.-R. Allouche, P. Crozet, and A. J. Ross, EPAPS of J. Chem. Phys. **143**, 044308 (2015).

[75] A. L. G. Rees, Proc. Phys. Soc. (London) **59**, 998 (1947).

[76] O. Klein, Z. Physik **76**, 226 (1932).

[77] R. Rydberg, Z. Physik **73**, 376 (1932).

[78] R. Rydberg, Z. Physik **80**, 514 (1933).

[79] R. J. LeRoy, "RKR1 2.0: a computer program implementing the first-order RKR method for determining diatomic molecular potential energy curves", University of Waterloo Chemical Physics Research, Report CP-657R, 2004.

APPENDIX

COMPARISON OF RO-VIBRATIONAL ENERGIES FOR $6^1\Sigma_g^+$ AND $3^1\Pi_g$ STATES OF $^{85}Rb_2$

Table A: Comparison between the ro-vibrational eigenvalues reproduced from the preliminary RKR potential energy curves and the experimentally observed energies, as well as energies calculated from *ab-initio* curves [74] for the $6^1\Sigma_g^+$ state of $^{85}Rb_2$.

v	J	Experiment (cm^{-1})	RKR (cm^{-1})	*ab-initio* (cm^{-1})	ΔE (Exp-RKR)	ΔE (RKR-*ab-initio*)
1	29	24659.9700	24659.4360	24672.6468	0.5340	-13.2107
1	31	24662.1494	24661.6111	24674.8359	0.5383	-13.2248
2	29	24705.9665	24705.6321	24718.6513	0.3344	-13.0192
2	31	24708.1310	24707.7973	24720.8338	0.3337	-13.0366
3	29	24751.8123	24751.6250	24764.4649	0.1873	-12.8399
3	31	24753.9618	24753.7803	24766.6407	0.1814	-12.8603
4	29	24797.4877	24797.4148	24810.0867	0.0729	-12.6719

(Continued on next page)

Table A: (*continued*)

v	J	Experiment (cm^{-1})	RKR (cm^{-1})	*ab-initio* (cm^{-1})	ΔE (Exp-RKR)	ΔE (RKR-*ab-initio*)
4	31	24799.6274	24799.5603	24812.2556	0.0671	-12.6954
5	29	24842.9266	24843.0015	24855.5240	-0.0749	-12.5225
5	31	24845.0613	24845.1371	24857.6862	-0.0758	-12.5491
6	29	24887.8412	24888.3851	24900.7707	-0.5440	-12.3856
6	31	24889.9380	24890.5108	24902.9259	-0.5729	-12.4150
7	29	24933.9287	24933.5656	24945.8195	0.3630	-12.2538
7	31	24936.0378	24935.6815	24947.9676	0.3563	-12.2861
8	29	24978.7712	24978.5431	24990.6709	0.2281	-12.1278
8	31	24980.8848	24980.6490	24992.8119	0.2357	-12.1628
9	29	25023.5144	25023.3174	25035.3282	0.1970	-12.0108
9	31	25025.6116	25025.4135	25037.4621	0.1981	-12.0486
10	29	25068.0564	25067.8886	25079.7918	0.1677	-11.9032
10	31	25070.1445	25069.9748	25081.9184	0.1696	-11.9436
11	29	25112.2977	25112.2567	25124.0586	0.0410	-11.8019
11	31	25114.3844	25114.3331	25126.1780	0.0513	-11.8449
12	29	25156.8097	25156.4218	25168.1247	0.3879	-11.7029
12	31	25158.8203	25158.4882	25170.2367	0.3321	-11.7485
13	29	25199.5273	25200.3837	25211.9846	-0.8564	-11.6009
13	31	25201.5900	25202.4403	25214.0891	-0.8503	-11.6488
14	29	25239.8734	25244.1426	25255.6316	-4.2692	-11.4891
14	31	25242.0105	25246.1892	25257.7286	-4.1787	-11.5393
15	29	25287.5138	25287.6983	25299.0586	-0.1846	-11.3603
15	31	25289.7977	25289.7351	25301.1478	0.0626	-11.4127
16	29	25329.9800	25331.0510	25342.2576	-1.0710	-11.2067
16	31	25332.2536	25333.0779	25344.3389	-0.8243	-11.2610
17	29	25373.8600	25374.2006	25385.2233	-0.3406	-11.0228
17	31	25376.0308	25376.2176	25387.2966	-0.1868	-11.0789
18	29	25417.7018	25417.1471	25427.9626	0.5547	-10.8155
18	31	25419.8740	25419.1543	25430.0278	0.7197	-10.8735
19	29		25459.8905	25470.5015		-10.6110

(Continued on next page)

Table A: (*continued*)

v	J	Experiment (cm^{-1})	RKR (cm^{-1})	*ab-initio* (cm^{-1})	ΔE (Exp-RKR)	ΔE (RKR-*ab-initio*)
19	31		25461.8878	25472.5590		-10.6711
20	29	25503.7663	25502.4309	25512.8474	1.3354	-10.4166
20	31	25505.8097	25504.4183	25514.8965	1.3914	-10.4782
21	29	25545.8042	25544.7681	25554.8852	1.0361	-10.1171
21	31	25547.8386	25546.7457	25556.9226	1.0929	-10.1769
22	29	25586.9110	25586.9023	25596.2141	0.0087	-9.3118
22	31	25588.8645	25588.8700	25598.2307	-0.0055	-9.3607
23	29	25629.9778	25628.8335	25635.9402	1.1444	-7.1067
23	31	25631.9428	25630.7913	25637.9178	1.1515	-7.1265
24	29	25671.3024	25670.5615	25672.8528	0.7409	-2.2913
24	31	25673.2779	25672.5094	25674.7762	0.7685	-2.2667
25	29	25712.5026	25712.0865	25707.2859	0.4160	4.8007
25	31	25714.4746	25714.0246	25709.1799	0.4500	4.8446
26	29	25755.2097	25753.4085	25741.2878	1.8012	12.1207
26	31	25757.0832	25755.3366	25743.1715	1.7465	12.1652
27	29	25794.9548	25794.5274	25774.4981	0.4274	20.0292
27	31	25796.8975	25796.4457	25776.3496	0.4518	20.0961
28	29	25835.5772	25835.4432	25806.3699	0.1339	29.0733
28	31	25837.4951	25837.3516	25808.2004	0.1434	29.1513
29	29	25875.7515	25876.1560	25837.8609	-0.4045	38.2951
29	31	25877.6399	25878.0546	25839.6743	-0.4147	38.3803
30	29	25915.4258	25916.6658	25868.4157	-1.2400	48.2501
30	31	25917.1451	25918.5544	25870.2028	-1.4094	48.3516
31	29	25955.2645	25956.9724	25898.3805	-1.7080	58.5919
31	31	25957.2285	25958.8512	25900.1536	-1.6228	58.6976

Table B: Comparison between the ro-vibrational eigenvalues reproduced from the preliminary RKR potential energy curves and the experimentally observed energies, as well as energies calculated from *ab-initio* curves [74] for the $3^1\Pi_g$ state of $^{85}Rb_2$.

v	J	Experiment (cm^{-1})	RKR (cm^{-1})	*ab-initio* (cm^{-1})	ΔE (Exp-RKR)	ΔE (RKR-*ab-initio*)
4	29	24985.6516	24985.3324	24979.5067	0.3192	5.8257
4	30	24986.6316	24986.3171	24980.5099	0.3145	5.8072
4	31	24987.6737	24987.3345	24981.5464	0.3392	5.7880
5	29	25026.1207	25025.9895	25019.9946	0.1311	5.9949
5	30	25027.1007	25026.9743	25020.9946	0.1263	5.9797
5	31	25028.1419	25027.9919	25022.0278	0.1500	5.9641
6	29	25066.3083	25066.3610	25060.2329	-0.0527	6.1280
6	30	25067.3012	25067.3459	25061.2295	-0.0447	6.1163
6	31	25068.3288	25068.3635	25062.2593	-0.0348	6.1042
7	29	25106.2731	25106.4467	25100.2094	-0.1737	6.2374
7	30	25107.2514	25107.4317	25101.2025	-0.1804	6.2292
7	31	25108.2739	25108.4495	25102.2287	-0.1756	6.2208
8	29	25145.9610	25146.2467	25139.9147	-0.2857	6.3320
8	30	25146.9430	25147.2319	25140.9043	-0.2889	6.3275
8	31	25147.9597	25148.2498	25141.9269	-0.2901	6.3229
9	29	25185.3663	25185.7611	25179.3448	-0.3948	6.4162
9	30	25186.3398	25186.7463	25180.3309	-0.4066	6.4155
9	31	25187.3587	25187.7643	25181.3497	-0.4057	6.4146
10	29	25224.3925	25224.9897	25218.4990	-0.5972	6.4907
10	30	25225.3679	25225.9750	25219.4813	-0.6071	6.4937
10	31	25226.3863	25226.9931	25220.4964	-0.6069	6.4968
11	29	25263.4122	25263.9326	25257.3752	-0.5204	6.5573
11	30	25264.3986	25264.9180	25258.3539	-0.5195	6.5642
11	31	25265.4224	25265.9363	25259.3650	-0.5139	6.5712
12	29	25303.8721	25302.5897	25295.9695	1.2824	6.6202
12	30	25304.8865	25303.5753	25296.9443	1.3111	6.6310
12	31	25305.9911	25304.5936	25297.9515	1.3975	6.6421
13	29	25343.1205	25340.9612	25334.2750	2.1593	6.6862
13	30	25344.1365	25341.9469	25335.2459	2.1896	6.7010

(Continued on next page)

Table B: (*continued*)

v	J	Experiment (cm^{-1})	RKR (cm^{-1})	*ab-initio* (cm^{-1})	ΔE (Exp-RKR)	ΔE (RKR-*ab-initio*)
13	31	25345.4595	25342.9653	25336.2490	2.4942	6.7163
14	29	25378.3863	25379.0470	25372.2812	-0.6607	6.7657
14	30	25379.3362	25380.0328	25373.2481	-0.6966	6.7847
14	31	25380.4478	25381.0513	25374.2470	-0.6035	6.8043
15	29	25416.6793	25416.8470	25409.9762	-0.1677	6.8708
15	30	25417.7978	25417.8329	25410.9388	-0.0351	6.8941
15	31	25418.6752	25418.8516	25411.9334	-0.1764	6.9181
16	29	25454.3962	25454.3613	25447.3496	0.0349	7.0117
16	30	25455.3620	25455.3473	25448.3079	0.0147	7.0394
16	31	25456.3505	25456.3661	25449.2980	-0.0156	7.0681
17	29	25492.1212	25491.5899	25484.3903	0.5313	7.1996
17	30	25493.0832	25492.5760	25485.3441	0.5072	7.2320
17	31	25494.0838	25493.5949	25486.3295	0.4889	7.2654
18	29	25528.6782	25528.5328	25521.0738	0.1453	7.4590
18	30	25529.6290	25529.5190	25522.0228	0.1100	7.4963
18	31	25530.6266	25530.5380	25523.0033	0.0886	7.5347
19	29	25566.3162	25565.1900	25557.3535	1.1262	7.8365
19	30	25567.3022	25566.1763	25558.2971	1.1259	7.8792
19	31	25568.3789	25567.1954	25559.2721	1.1835	7.9233
20	29	25600.8979	25601.5615	25593.1703	-0.6636	8.3912
20	30	25601.7934	25602.5479	25594.1081	-0.7545	8.4397
20	31	25602.9393	25603.5670	25595.0771	-0.6277	8.4899
21	29	25637.6378	25637.6472	25628.4957	-0.0094	9.1515
21	30	25638.5258	25638.6337	25629.4275	-0.1079	9.2062
21	31	25639.5482	25639.6530	25630.3904	-0.1048	9.2626
22	29	25672.9555	25673.4472	25663.3467	-0.4918	10.1005
22	30	25673.8644	25674.4338	25664.2727	-0.5694	10.1611
22	31	25674.8627	25675.4532	25665.2295	-0.5905	10.2237
23	29	25708.4558	25708.9616	25697.7293	-0.5058	11.2322
23	30	25709.4013	25709.9482	25698.6492	-0.5469	11.2991
23	31	25710.4269	25710.9677	25699.5995	-0.5408	11.3681

(Continued on next page)

Table B: (*continued*)

v	J	Experiment (cm^{-1})	RKR (cm^{-1})	*ab-initio* (cm^{-1})	ΔE (Exp-RKR)	ΔE (RKR-*ab-initio*)
24	29	25743.4395	25744.1901	25731.6169	-0.7507	12.5732
24	30	25744.6234	25745.1769	25732.5303	-0.5536	12.6466
24	31	25745.4898	25746.1964	25733.4741	-0.7067	12.7224
25	29	25778.3983	25779.1330	25765.0164	-0.7347	14.1166
25	30	25779.4768	25780.1199	25765.9235	-0.6430	14.1964
25	31	25780.3808	25781.1395	25766.8606	-0.7587	14.2788
27	29	25849.8777	25848.1616	25830.3786	1.7161	17.7830
27	30	25850.6364	25849.1486	25831.2723	1.4877	17.8763
27	31	25851.9337	25850.1684	25832.1958	1.7653	17.9726

BIBLIOGRAPHY

[1] H. R. Gray, R. M. Whitley, and C. R. Stroud, Opt. Lett. **3**, 218 (1978).

[2] F. Renzoni, A. Lindner, and E. Arimondo, Phys. Rev. A **60**, 450 (1999).

[3] F.-L. Li, and S.-Y. Zhu, Opt. Commun. **162**, 155 (1999).

[4] S. E. Harris, J. E. Field, and A. Imamoğlu, Phys. Rev. Lett. **64**, 1107 (1990).

[5] K.-J. Boller, A. Imamoğlu, and S. E. Harris, Phys. Rev. Lett. **66**, 2593 (1991).

[6] J. E. Field, K. H. Hahn, and S. E. Harris, Phys. Rev. Lett. **67**, 3062 (1991).

[7] S. H. Autler, and C. H. Townes, Phys. Rev. **100**, 703 (1955).

[8] A. Imamoğlu, and S. E. Harris, Opt. Lett. **14**, 1344 (1989).

[9] S. E. Harris, Phys. Rev. Lett. **62**, 1033 (1989).

[10] M. O. Scully, S.-Y. Zhu, and A. Gavrielides, Phys. Rev. Lett. **62**, 2813 (1989).

[11] J. Qi, G. Lazarov, X. Wang, L. Li, L. M. Narducci, A. M. Lyyra, and F. C. Spano, Phys. Rev. Lett. **83**, 288 (1999).

[12] M. M. Kash, V. A. Sautenkov, A. S. Zibrov, L. Hollberg, G. R. Welch, M. D. Lukin, Y. Rostovtsev, E. S. Fry, and M. O. Scully, Phys. Rev. Lett. **82**, 5229 (1999).

[13] D. Budker, D. F. Kimball, S. M. Rochester, and V. V. Yashchuk, Phys. Rev. Lett. **83**, 1767 (1999).

[14] M. Ikram, and M. S. Zubairy, Phys. Rev. A **65**, 044305 (2002).

[15] V. Minogin, and Y. Rozhdestvenskii, Opt. Commun. **64**, 172 (1987).

[16] E. H. Ahmed, S. Ingram, T. Kirova, O. Salihoglu, J. Huennekens, J. Qi, Y. Guan, and A. M. Lyyra, Phys. Rev. Lett. **107**, 163601 (2011).

[17] E. H. Ahmed, X. Pan, J. Huennekens, and A. M. Lyyra, Phys. Rev. A **89**, 061401 (2014).

[18] B. H. Bransden, and C. J. Joachain, *Physics of atoms and molecules* (John Wiley & Sons, New York, 1983).

[19] I. N. Levine, *Molecular spectroscopy* (John Wiley & Sons, New York, 1975).

[20] G. Herzberg, *Molecular spectra and molecular structure I, Spectra of diatomic molecules* (Krieger Publishing Company, Malabar, Florida, 1989).

[21] J. I. Steinfeld, *Molecules and radiation: an introduction to modern molecular spectroscopy* (Dover, New York, 1985).

[22] H. Lefebvre-Brion, and R. W. Field, *Perturbations in the spectra of diatomic molecules* (Academic Press, Orlando, 1986).

[23] M. Born, and R. Oppenheimer, Ann. Phys. **84**, 4571 (1927).

[24] J. Brown, J. Hougen, K.-P. Huber, J. Johns, I. Kopp, H. Lefebvre-Brion, A. Merer, D. Ramsay, J. Rostas, and R. Zare, J. Mol. Spectrosc. **55**, 500 (1975).

[25] H. Lefebvre-Brion, and R. W. Field, *The spectra and dynamics of diatomic molecules* (Elsevier, Amsterdam, 2004).

[26] P. F. Bernath, *Spectra of atoms and molecules* (Oxford University Press, Oxford, 1995).

[27] J. L. Dunham, Phys. Rev. **41**, 721 (1932).

[28] F. Hund, Z. Phys. **42**, 93 (1927).

[29] L. Li, and R. W. Field, J. Phys. Chem. **87**, 3020 (1983).

[30] L. Li, and R. W. Field, *Molecular dynamics and spectroscopy of stimulated emission pumping*, edited by H. L. Dai, and R.W.Field, (World Scientific, Singapore, 1995) Chap. 7, p. 251.

[31] L. Li, and A. M. Lyyra, Spectrochimi. Acta, Part A **55**, 2147 (1999).

[32] L. Morgus, P. Burns, R. D. Miles, A. D. Wilkins, U. Ogba, A. P. Hickman, and J. Huennekens, J. Chem. Phys. **122**, 144313 (2005).

[33] P. Burns, L. Sibbach-Morgus, A. D. Wilkins, F. Halpern, L. Clarke, R. D. Miles, L. Li, A. P. Hickman, and J. Huennekens, J. Chem. Phys. **119**, 4743 (2003).

[34] S. Frank L. Pedrotti, L. M. Pedrotti, and L. S. Pedrotti, *Introduction to optics*, 3rd ed. (Pearson Education, Inc., New Jersey, 2007) Chap. 26, p. 567.

[35] D. R. Skinner, and R. E. Whitcher, J. Phys. E **5**, 237 (1972).

[36] J. Qi, Ph.D. Thesis, Temple University (2000).

[37] J. Qi, F. C. Spano, T. Kirova, A. Lazoudis, J. Magnes, L. Li, L. M. Narducci, R. W. Field, and A. M. Lyyra, Phys. Rev. Lett. **88**, 173003 (2002).

[38] F. C. Spano, J. Chem. Phys. **114**, 276 (2001).

[39] D. L. Cooper, J. M. Hutson, and T. Uzer, Chem. Phys. Lett. **86**, 472 (1982).

[40] S. Ingram, Ph.D. Thesis, Temple University (2010).

[41] L. Veseth, Theo. Chim. Acta **18**, 368 (1970).

[42] R. N. Zare, *Angular momentum* (Wiley-Interscience, New York, 1986).

[43] M. Blume, A. J. Freeman, and R. E. Watson, Phys. Rev. **134**, A320 (1964).

[44] X. Xie, and R. W. Field, Chem. Phys. **99**, 337 (1985).

[45] L. Li, Q. Zhu, A. M. Lyyra, T. Whang, W. C. Stwalley, R. W. Field, and M. H. Alexander, J. Chem. Phys. **97**, 8835 (1992).

[46] L. Li, S. Antonova, A. Yiannopoulou, K. Urbanski, and A. M. Lyyra, J. Chem. Phys. **105**, 9859 (1996).

[47] A. M. Lyyra, H. Wang, T.-J. Whang, W. C. Stwalley, and L. Li, Phys. Rev. Lett. **66**, 2724 (1991).

[48] T. Kirova, and F. C. Spano, Phys. Rev. A **71**, 063816 (2005).

[49] M. V. Korolkov, and J. Manz, J. Chem. Phys. **120**, 11522 (2004).

[50] J. González-Vázquez, I. R. Sola, J. Santamaria, and V. S. Malinovsky, Chem. Phys. Lett. **431**, 231 (2006).

[51] J. González-Vázquez, I. R. Sola, J. Santamaria, and V. S. Malinovsky, J. Chem. Phys. **125**, 124315 (2006).

[52] J. Huennekens, A. Loza, M. Masters, and K. M. Sando, J. Chem. Phys. **88**, 6013 (1988).

[53] M. Masters, J. Huennekens, W. Luh, L. Li, A. M. Lyyra, K. Sando, V. Zafiropulos, and W. C. Stwalley, J. Chem. Phys. **92**, 5801 (1990).

[54] H. Sun, and J. Huennekens, J. Chem. Phys. **97**, 4714 (1992).

[55] B. Barakat, R. Bacis, F. Carrot, S. Churassy, P. Crozet, F. Martin, and J. Verges, Chem. Phys. **102**, 215 (1986).

[56] K. Urbanski, S. Antonova, A. Yiannopoulou, A. M. Lyyra, L. Li, and W. C. Stwalley, J. Chem. Phys. **116**, 10557 (2002).

[57] I. Russier, A. Yiannopoulou, P. Crozet, A. Ross, F. Martin, and C. Linton, J. Mol. Spectrosc. **184**, 129 (1997).

[58] K. Urbanski, S. Antonova, A. M. Lyyra, L. Li, and B. Ji, J. Chem. Phys. **109**, 912 (1998).

[59] A. Yiannopoulou, B. Ji, L. Li, M. Li, K. Urbanski, A. M. Lyyra, W. C. Stwalley, and G. Jeung, J. Chem. Phys. **101**, 3581 (1994).

[60] M. H. Alexander, J. Chem. Phys. **76**, 429 (1982).

[61] S. Stenholm, *Foundations of laser spectroscopy* (Wiley Interscience, New York, 1984).

[62] M. O. Scully, and M. S. Zubairy, *Quantum optics* (Cambridge University Press, Cambridge, 2002).

[63] W. Demtröder, *Laser spectroscopy* (Springer-Verlag Berlin Heidelberg, New York, 1982).

[64] A. N. Nesmeyanov, *Vapor pressure of the chemical elements* (Elsevier, Amsterdam, 1963).

[65] X. Wang, J. Magnes, A. M. Lyyra, A. J. Ross, F. Martin, P. M. Dove, and R. J. LeRoy, J. Chem. Phys. **117**, 9339 (2002).

[66] C. M. Wolfe, S. Ashman, J. Bai, B. Beser, E. H. Ahmed, A. M. Lyyra, and J. Huennekens, J. Chem. Phys. **134**, 174301 (2011).

[67] A. M. Lyyra, W. T. Luh, L. Li, H. Wang, and W. C. Stwalley, J. Chem. Phys. **92**, 43 (1990).

[68] H. Salami, T. Bergeman, B. Beser, J. Bai, E. H. Ahmed, S. Kotochigova, A. M. Lyyra, J. Huennekens, C. Lisdat, A. V. Stolyarov, O. Dulieu, P. Crozet, and A. J. Ross, EPAPS of Phys. Rev. A **80**, 022515 (2009).

[69] S. Gerstenkorn, and P. Luc, Rev. Phys. Appl. (Paris) **14**, 791 (1979).

[70] S. Gerstenkorn, and P. Luc, *Atlas du spectre d'absorption de la molécule de l'iode entre* 14 800-20 000 cm^{-1} (Editions du C.N.R.S., 15, quai Anatole-France, 75700 Paris).

[71] J. Bai, Ph.D. Thesis, Temple University (2011).

[72] B. A. Palmer, R. A. Keller, and R. Engleman, Jr, LASL Report No. LA-8251-MS (Los Alamos Scientific Laboratory, Los Alamos, NM, 1980).

[73] R. J. LeRoy, University of Waterloo Chemical Physics Research Report No. CP663, 2007.

[74] W. Jastrzebski, P. Kowalczyk, J. Szczepkowski, A.-R. Allouche, P. Crozet, and A. J. Ross, EPAPS of J. Chem. Phys. **143**, 044308 (2015).

[75] A. L. G. Rees, Proc. Phys. Soc. (London) **59**, 998 (1947).

[76] O. Klein, Z. Physik **76**, 226 (1932).

[77] R. Rydberg, Z. Physik **73**, 376 (1932).

[78] R. Rydberg, Z. Physik **80**, 514 (1933).

[79] R. J. LeRoy, "RKR1 2.0: a computer program implementing the first-order RKR method for determining diatomic molecular potential energy curves", University of Waterloo Chemical Physics Research, Report CP-657R, 2004.